How water vapor shapes Earth's longwave climate feedback

Florian Elias Römer

Hamburg 2024

How water vapor shapes Earth's longwave climate feedback

Florian Elias Römer

Hamburg 2024

Florian Elias Römer

aus Oberndorf, Österreich

Max-Planck-Institut für Meteorologie
The International Max Planck Research School on Earth System Modelling
(IMPRS-ESM)

Universität Hamburg
Fachbereich Erdsystemwissenschaften
Institut für Meereskunde

Bundesstraße 53
20146 Hamburg

Titelgrafik vom Autor:
Von Satelliten gemessene Abstrahlung der Erde bei zwei verschiedenen Frequenzen

ABSTRACT

The clear-sky longwave feedback λ is by far the strongest radiative feedback in Earth's climate system. Therefore, λ plays an essential role in determining climate sensitivity, the temperature increase following a doubling of atmospheric CO_2 concentration. The overarching theme of this thesis concerns the uniquely important role water vapor plays in determining λ which arises from the fact that water vapor is a strong greenhouse gas whose concentration strongly increases with temperature. These spectroscopic and thermodynamic properties of water vapor are overall well-understood, but uncertainties remain regarding their exact quantitative behavior. In this thesis, I investigate the impact of these uncertainties in the properties of water vapor on λ. I do so by focusing on the spectrally resolved λ_ν which quantifies how λ depends on the wavenumber ν of thermal radiation. This approach allows for a better understanding of the underlying feedback processes regarding both the relevant greenhouse gases and the vertical layers of the atmosphere.

In my first and second study, I focus on uncertainty in the thermodynamics, specifically, how relative humidity $\mathcal{R}$ will change in a warming atmosphere. To first order, it is usually assumed that $\mathcal{R}$ remains constant with warming; however, changes in circulation can lead to variations in $\mathcal{R}$, both regionally and in the global mean. In my first study, I derive the global-mean λ_ν from satellite observations of short-term variability. I find that the observed λ_ν is more strongly stabilizing in the absorption bands of water vapor compared to idealized model studies. Based on radiative transfer simulations, I demonstrate that this is in part due to two features of water vapor not captured by these models: (1) Horizontal variations in water vapor concentration q between the tropics and the polar regions mean that surface emission from the polar regions can more easily escape to space in the real world compared to idealized models that represent Earth's atmosphere by a single global-mean atmospheric column. (2) Decreasing global-mean $\mathcal{R}$ with warming in the analyzed short-term variability causes more atmospheric emission with warming which stabilizes the observed λ_ν compared to idealized models that assume constant $\mathcal{R}$. This observational constraint on the global-mean λ_ν can be useful to evaluate the representation of $\mathcal{R}$ variations and feedback processes in climate models.

In my second study, I expand on these findings by directly observing λ_ν as a function of near-surface air temperature T_s. These observations corroborate the effect of surface emission at low T_s, and further show that λ_ν at these T_s is sensitive to biases in the representation

of Earth's skin temperature. The observations also confirm the important role of changes in $\mathcal{R}$ with warming at high T_s. In particular, I demonstrate that the spectrum of λ_ν directly maps onto vertical variations in the change of $\mathcal{R}$ with warming, as different parts of the spectrum are sensitive to different atmospheric layers. This way, I demonstrate that the observed λ_ν at a wide range of T_s can be fully understood considering only a small number of variables, which solidifies our understanding of λ and provides the foundation for similar studies on past climates of Earth.

In my third study, I focus on uncertainty in the spectroscopy, specifically in water vapor continuum absorption, which represents absorption due to poorly understood interactions between water vapor molecules. Using a single-column model, I find that the two components of the continuum differently affect λ: Increasing the self continuum, which depends quadratically on q, weakens λ; increasing the foreign continuum, which depends linearly on q, strengthens λ. I demonstrate that these opposite effects occur because of the different dependencies on q: A stronger self continuum mostly reduces outgoing longwave radiation $\mathcal{L}$ at high T_s, whereas a stronger foreign continuum mostly reduces $\mathcal{L}$ at low T_s. To represent real-world continuum uncertainty, I account for the negative correlation between self and foreign continuum uncertainties using two different approaches. This way, I show that continuum uncertainty affects λ by affecting both the temperature dependence and vertical distribution of continuum absorption. Overall, the effect on λ is modest at global-mean temperatures, but substantial at tropical temperatures. Therefore, a correct partitioning between self and foreign continuum absorption is important to better constrain λ and its temperature dependence.

ZUSAMMENFASSUNG

Die langwellige Rückkopplung bei klarem Himmel, λ, ist bei weitem die stärkste Strahlungsrückkopplung im Klimasystem der Erde. Daher spielt λ eine wesentliche Rolle bei der Bestimmung der Klimasensitivität, dem Temperaturanstieg in Folge einer Verdopplung der atmosphärischen CO_2-Konzentration. Diese Arbeit behandelt die herausragende Rolle, die Wasserdampf bei der Bestimmung von λ spielt. Diese ergibt sich daraus, dass Wasserdampf ein starkes Treibhausgas ist, dessen Konzentration mit steigender Temperatur stark zunimmt. Diese spektroskopischen und thermodynamischen Eigenschaften von Wasserdampf sind grundsätzlich gut verstanden, aber es gibt weiterhin Unsicherheiten hinsichtlich ihres genauen quantitativen Verhaltens. In dieser Arbeit untersuche ich die Auswirkungen dieser Unsicherheiten in den Eigenschaften von Wasserdampf auf λ. Zu diesem Zweck analysiere ich das spektral aufgelöste λ_ν, das quantifiziert, wie λ von der Wellenzahl ν der thermischen Strahlung abhängt. Dieser Ansatz ermöglicht ein besseres Verständnis der zugrunde liegenden Rückkopplungsprozesse bezüglich der relevanten Treibhausgase und vertikalen Schichten der Atmosphäre.

In meiner ersten und zweiten Studie konzentriere ich mich auf Unsicherheiten in der Thermodynamik, insbesondere darauf, wie sich die relative Feuchte $\mathcal{R}$ in einer wärmeren Atmosphäre ändert. In erster Näherung wird in der Regel angenommen, dass $\mathcal{R}$ bei Erwärmung konstant bleibt, doch Änderungen in der Zirkulation können Veränderungen der relativen Feuchte sowohl regional als auch im globalen Mittel verursachen. In meiner ersten Studie leite ich das global gemittelte λ_ν aus Satellitenbeobachtungen der kurzfristigen Variabilität ab. Ich finde heraus, dass das beobachtete λ_ν in den Absorptionsbanden von Wasserdampf stärker stabilisierend wirkt im Vergleich zu idealisierten Modellstudien. Anhand von Strahlungstransfersimulationen zeige ich, dass dies teilweise auf zwei Merkmale von Wasserdampf zurückzuführen ist, die von diesen Modellen nicht erfasst werden: (1) Horizontale Variationen in der Wasserdampfkonzentration q zwischen den Tropen und den Polargebieten bedeuten, dass die bodennahe Emission aus den Polargebieten in der realen Welt leichter in den Weltraum entweichen kann im Vergleich zu idealisierten Modellen, welche die Atmosphäre der Erde durch eine einzelne, global gemittelt Atmosphärensäule darstellen. (2) Eine abnehmende global gemittelte $\mathcal{R}$ bei Erwärmung in der analysierten kurzfristigen Variabilität führt zu mehr atmosphärischer Emission bei Erwärmung, was das beobachtete λ_ν stabilisiert im Vergleich zu idealisierten Modellen, welche konstante $\mathcal{R}$ annehmen. Diese beobachtungsgestützte Einschränkung des global gemittelten λ_ν kann nützlich sein, um die Darstellung von

Variationen in der relativen Feuchte sowie Rückkopplungsprozessen in Klimamodellen zu evaluieren.

In meiner zweiten Studie baue ich auf diese Erkenntnisse auf, indem ich λ_ν als Funktion der bodennahen Lufttemperatur T_s direkt beobachte. Diese Beobachtungen bestätigen den Effekt der bodennahen Emission bei niedrigen T_s und zeigen darüber hinaus, dass λ_ν bei diesen T_s empfindlich auf Abweichungen in der Darstellung der Obeflächentemperatur der Erde reagiert. Die Beobachtungen bestätigen auch die wichtige Rolle von Änderungen der relativen Feuchte bei Erwärmung bei hohen T_s. Insbesondere zeige ich, dass das Spektrum von λ_ν direkt vertikale Variationen in der Änderung der relativen Feuchte bei Erwärmung abbildet, da verschiedene Teile des Spektrums auf verschiedene atmosphärische Schichten reagieren. Auf diese Weise zeige ich, dass das beobachtete λ_ν bei einer großen Bandbreite von T_s vollständig verstanden werden kann, wenn nur eine geringe Anzahl von Variablen berücksichtigt wird. Dies festigt unser Verständnis von λ und bildet die Grundlage für ähnliche Studien zu vergangenen Klimaten der Erde.

In meiner dritten Studie konzentriere ich mich auf Unsicherheiten in der Spektroskopie, insbesondere in der Kontinuumabsorption von Wasserdampf, welche die Absorption aufgrund von schlecht verstandenen Wechselwirkungen zwischen Wasserdampfmolekülen darstellt. Unter Verwendung eines Einzelsäulenmodells finde ich heraus, dass die zwei Komponenten des Kontinuums λ unterschiedlich beeinflussen: Eine Erhöhung des Eigenkontinuums, das quadratisch von q abhängt, schwächt λ ab; eine Erhöhung des Fremdkontinuums, das linear von q abhängt, verstärkt λ. Ich zeige, dass diese entgegengesetzten Auswirkungen aufgrund der unterschiedlichen Abhängigkeiten von q auftreten: Ein stärkeres Eigenkontinuum reduziert die ausgehende langwellige Strahlung $\mathcal{L}$ hauptsächlich bei hohen T_s während ein stärkeres Fremdkontinuum $\mathcal{L}$ hauptsächlich bei niedrigen T_s reduziert. Um die Unsicherheit des Kontinuums in der realen Welt darzustellen, berücksichtige ich die negative Korrelation zwischen den Unsicherheiten des Eigenkontinuums und des Fremdkontinuums mit zwei verschiedenen Ansätzen. Auf diese Weise zeige ich, dass die Unsicherheit des Kontinuums λ beeinflusst, indem sie sowohl die Temperaturabhängigkeit als auch die vertikale Verteilung der Kontinuumabsorption beeinflusst. Insgesamt ist der Effekt auf λ bei globalen Mitteltemperaturen moderat, aber bei tropischen Temperaturen erheblich. Daher ist eine korrekte Aufteilung zwischen Eigen- und Fremdkontinuumabsorption wichtig, um λ und seine Temperaturabhängigkeit besser zu bestimmen.

In the context of contemporary climate change it is important to predict future global-mean warming. This is for example necessary to study local effects of climate change, such as shifts in weather patterns and extreme events. This global-mean warming depends on the amount of emitted CO_2 and on Earth's climate sensitivity, the temperature increase that would follow a hypothetical doubling of atmospheric CO_2 concentration. Consequently, climate sensitivity is the central quantity of interest in climate science.

CO_2 is a powerful greenhouse gas which means that more CO_2 in the atmosphere traps more thermal radiation and thus disrupts Earth's energy balance. This additional heat increases Earth's temperature which in turn radiates more energy to space, allowing it to restore its energy balance. The effectiveness of this process is quantified by Earth's radiative feedback. A strong radiative feedback means that for a given warming, Earth can radiate a lot more energy to space. Thus, to restore energy balance, only little warming has to occur and climate sensitivity is low. In contrast, a weak radiative feedback means that for a given warming, Earth can radiate only slightly more energy to space. Thus, to restore energy balance, a lot of warming has to occur and climate sensitivity is high.

The magnitude of this radiative feedback depends on many different feedback processes. The most important one — and the focus of this thesis — is the clear-sky longwave feedback. It encompasses two major processes: First, when Earth's surface and atmosphere warm, they emit more radiation. Second, a warmer atmosphere contains more water vapor which is also a powerful greenhouse gas. Therefore, more water vapor in Earth's atmosphere traps even more thermal radiation, which leads to even more warming. This amplifying feedback loop causes water vapor to roughly double climate sensitivity. This important effect of water vapor has been recognized for a long time and is overall well-understood. However, uncertainties still remain in the details.

In this thesis, I investigate the effect of two of these uncertainties on the clear-sky longwave feedback. First, it is not exactly known how much more water vapor a warmer atmosphere contains. It is generally assumed that relative humidity will remain approximately constant as temperature rises which would imply about 6–7 % more water vapor per degree of warming. However, changes in atmospheric circulation can lead to changes in relative humidity with warming. The first research question of this thesis is therefore: How does uncertainty in the change of relative humidity with warming affect Earth's clear-sky longwave feedback? I find that even small changes in rel-

ative humidity within the current range of uncertainty can have a substantial effect and thus should not be neglected when studying the clear-sky longwave feedback. This also highlights the importance of better understanding the processes that control relative humidity in a warming world.

Second, the ability of water vapor to absorb thermal radiation is also mostly well-understood. However, interactions between water molecules in Earth's atmosphere affect its absorption properties, and many of these interactions are still poorly understood. Therefore, these interactions are commonly subsumed in the so-called water vapor continuum absorption. This continuum absorption can only be estimated based on observations and thus still exhibits substantial uncertainty. The second research question of this thesis is therefore: How does this uncertainty in water vapor continuum absorption affect Earth's clear-sky longwave feedback? I find that uncertainty in water vapor continuum absorption only has a modest effect at temperatures around Earth's global mean. However, it can have a substantial effect at higher temperatures that frequently occur in tropical regions. This highlights that continuum uncertainty should be considered when studying the temperature dependence of the clear-sky longwave feedback.

Overall, this thesis provides important insights into how uncertainties in the properties of water vapor affect Earth's clear-sky longwave feedback. These findings highlight the importance of better understanding the processes underlying changes in relative humidity with warming and absorption by the water vapor continuum. Better understanding these processes can help improve their representation in climate models and, thus, support efforts to further constrain Earth's climate sensitivity.

POPULÄRWISSENSCHAFTLICHE ZUSAMMENFASSUNG

Im Kontext des gegenwärtigen Klimawandels ist es wichtig, die zukünftige globale Erwärmung vorherzusagen. Dies ist etwa notwendig, um lokale Auswirkungen des Klimawandels zu untersuchen, etwa durch Verschiebungen der Wettermuster und Extremereignisse. Diese globale Erwärmung hängt von der Menge des emittierten CO_2 und von der Klimasensitivität der Erde ab, dem Temperaturanstieg in Folge einer hypothetische Verdopplung der atmosphärischen CO_2-Konzentration. Folglich ist die Klimasensitivität die zentrale Größe in der Klimaforschung.

CO_2 ist ein starkes Treibhausgas, das heißt, dass mehr CO_2 in der Atmosphäre mehr Wärmestrahlung einfängt und somit das Energiegleichgewicht der Erde stört. Diese zusätzliche Wärme erhöht die Temperatur der Erde, wodurch diese mehr Energie in den Weltraum abstrahlt, bis ihr Energiegleichgewicht wiederhergestellt ist. Die Wirksamkeit dieses Prozesses wird durch die Strahlungsrückkopplung der Erde quantifiziert. Eine starke Strahlungsrückkopplung bedeutet, dass die Erde bei einer bestimmten Erwärmung viel mehr Energie abstrahlen kann. Um das Energiegleichgewicht wiederherzustellen, muss daher nur eine geringe Erwärmung erfolgen, und die Klimasensitivität ist gering. Im Gegensatz dazu bedeutet eine schwache Strahlungsrückkopplung, dass die Erde bei einer gegebenen Erwärmung kaum mehr Energie abstrahlen kann. Um das Energiegleichgewicht wiederherzustellen, muss daher eine starke Erwärmung erfolgen, und die Klimasensitivität ist hoch.

Das Ausmaß dieser Strahlungsrückkopplung hängt von vielen verschiedenen Rückkopplungsprozessen ab. Der wichtigste davon — und der Schwerpunkt dieser Arbeit — ist die langwellige Rückkopplung bei klarem Himmel. Sie umfasst zwei Hauptprozesse: Erstens, wenn sich die Erdoberfläche und die Atmosphäre erwärmen, geben sie mehr Strahlung ab. Zweitens enthält eine wärmere Atmosphäre mehr Wasserdampf, der ebenfalls ein starkes Treibhausgas ist. Daher fängt mehr Wasserdampf in der Erdatmosphäre noch mehr Wärmestrahlung ein, was zu einer noch stärkeren Erwärmung führt. Diese verstärkende Rückkopplungsschleife bewirkt, dass Wasserdampf die Klimasensitivität ungefähr verdoppelt. Diese wichtige Wirkung des Wasserdampfs ist seit langem bekannt und wird im Allgemeinen gut verstanden. In den Details bestehen jedoch noch Unsicherheiten.

In dieser Arbeit untersuche ich die Auswirkungen von zwei dieser Unsicherheiten auf die langwellige Rückkopplung bei klarem Himmel. Erstens ist nicht genau bekannt, wie viel mehr Wasserdampf eine wärmere Atmosphäre enthält. Im Allgemeinen wird angenom-

men, dass die relative Feuchte bei steigenden Temperaturen in etwa konstant bleibt, was etwa 6-7 % mehr Wasserdampf pro Grad Erwärmung bedeuten würde. Veränderungen in der atmosphärischen Zirkulation können jedoch zu Veränderungen der relativen Feuchte bei Erwärmung führen. Die erste Forschungsfrage dieser Arbeit lautet daher: Wie wirkt sich die Unsicherheit in der Änderung der relativen Feuchte mit der Erwärmung auf die langwellige Rückkopplung bei klarem Himmel aus? Ich habe herausgefunden, dass selbst kleine Änderungen der relativen Feuchte innerhalb des derzeitigen Unsicherheitsbereichs eine erhebliche Auswirkung haben können und deshalb in Studien über die langwellige Rückkopplung bei klarem Himmel nicht vernachlässigt werden sollten. Dies unterstreicht auch die Bedeutung eines besseren Verständnisses der Prozesse, welche die relative Feuchte in einer sich erwärmenden Welt kontrollieren.

Zweitens ist auch die Fähigkeit von Wasserdampf, Wärmestrahlung zu absorbieren, weitgehend verstanden. Allerdings können Wechselwirkungen zwischen Wassermolekülen in der Atmosphäre die Absorptionseigenschaften von Wasserdampf beeinflussen, und viele dieser Wechselwirkungen sind noch nicht gut verstanden. Daher werden diese Wechselwirkungen üblicherweise in der so genannten Wasserdampf-Kontinuumsabsorption zusammengefasst. Diese Kontinuumsabsorption kann nur auf der Grundlage von Beobachtungen abgeschätzt werden und ist daher noch mit erheblichen Unsicherheiten behaftet. Die zweite Forschungsfrage dieser Arbeit lautet daher: Was sind die Auswirkungen dieser Unsicherheit in der Wasserdampf-Kontinuumsabsorption auf die langwellige Rückkopplung bei klarem Himmel? Ich habe herausgefunden, dass die Unsicherheit in der Wasserdampf-Kontinuumsabsorption nur einen moderaten Effekt bei Temperaturen um den globalen Mittelwert der Erde hat. Allerdings kann sie einen erheblichen Effekt bei höheren Temperaturen haben, welche häufig in tropischen Regionen auftreten. Dies macht deutlich, dass die Kontinuumsunsicherheit bei der Untersuchung der Temperaturabhängigkeit der langwelligen Rückkopplung bei klarem Himmel berücksichtigt werden sollte.

Insgesamt liefert diese Arbeit wichtige Erkenntnisse darüber, wie sich Unsicherheiten in den Eigenschaften von Wasserdampf auf die langwellige Rückkopplung bei klarem Himmel auswirken. Diese Ergebnisse zeigen, wie wichtig es ist, die Prozesse besser zu verstehen, die den Veränderungen der relativen Feuchte bei Erwärmung und Absorption durch das Wasserdampfkontinuum zugrunde liegen. Ein besseres Verständnis dieser Prozesse kann dazu beitragen, ihre Darstellung in Klimamodellen zu verbessern, und so die Bemühungen um eine weitere Begrenzung der Klimasensitivität der Erde unterstützen.

PUBLICATIONS

The following three first-author publications are part of this thesis and included in the appendix:

APPENDIX A

Roemer, F. E., S. A. Buehler, M. Brath, L. Kluft, and V. O. John (2023a). "Direct observation of Earth's spectral long-wave feedback parameter." In: *Nature Geoscience* 16.5, pp. 416–421. DOI: 10.1038/s41561-023-01175-6

APPENDIX B

At the time of writing, this study is under review at *Journal of Climate*:

Roemer, F. E. and S. A. Buehler (2024a). "Observations of the Clear-Sky Spectral Longwave Feedback at Surface Temperatures Between 210 K and 310 K." In: *ESS Open Archive*. DOI: 10.22541/essoar.171804490.08945991/v2

APPENDIX C

Roemer, F. E., S. A. Buehler, L. Kluft, and R. Pincus (2024a). "Effect of Uncertainty in Water Vapor Continuum Absorption on CO_2 Forcing, Longwave Feedback, and Climate Sensitivity." In: *Journal of Advances in Modeling Earth Systems* 16.7, e2023MS004157. DOI: 10.1029/2023MS004157

ACKNOWLEDGMENTS

CONTENTS

Part I

UNIFYING ESSAY

1

MOTIVATION

The increase in global-mean near-surface air temperature T_s in response to a doubling of the atmospheric CO_2 concentration is quantified by Earth's climate sensitivity $\mathcal{S}$ (Charney et al., 1979). Apart from academic interest, constraining the magnitude of $\mathcal{S}$ is of paramount importance in the context of contemporary climate change. This is because $\mathcal{S}$ provides the foundation for studying regional changes in temperature, precipitation, weather patterns, and extreme events as well as their impact on human populations and ecosystems. However, despite extensive research throughout the past decades, substantial uncertainty remains regarding the magnitude of $\mathcal{S}$, with a current best estimate of 2.6 K–3.9 K (66 % confidence, Sherwood et al., 2020).

Fundamentally, the magnitude of $\mathcal{S}$ depends on two central variables: (1) The CO_2 radiative forcing $\mathcal{F}_{2\times CO_2}$ quantifies by how much Earth's energy balance is perturbed if the atmospheric CO_2 concentration is doubled; (2) the radiative feedback λ quantifies how effectively Earth can restore this energy balance by increasing T_s. The overarching theme of this thesis concerns the central role of water vapor in shaping λ.

As its name suggests, λ encompasses the radiative effects of different feedback processes within Earth's climate system which are typically analyzed separately (e. g., Hansen et al., 1984; Soden et al., 2008; Sherwood et al., 2020). Among these processes, by far the strongest is the clear-sky longwave feedback λ_{lwcs} which quantifies the change in emission and absorption of thermal radiation from Earth's surface and within its atmosphere due to changes in temperature and humidity (e. g., Manabe and Wetherald, 1967; Budyko, 1969; Koll et al., 2023). Even in the absence of other feedbacks, λ_{lwcs} generates an $\mathcal{S}$ of approximately 2 K (Kluft et al., 2019), highlighting the crucial need to thoroughly understand its underlying mechanisms. Furthermore, although water vapor influences the absorption of solar radiation in Earth's atmosphere, its primary impact on the climate arises from its role in shaping λ_{lwcs}, making this the central focus of this thesis.

Water vapor plays a uniquely important role in shaping λ_{lwcs} — and by extension $\mathcal{S}$. The significance of water vapor stems from the interplay of two of its fundamental properties: (1) Water vapor strongly absorbs thermal radiation, thus making it a powerful greenhouse gas (Foote, 1856; Tyndall, 1861a,b); and (2) the equilibrium concentration of water vapor increases approximately exponentially with temperature following the Clausius-Clapeyron relation (Carnot, 1824; Clapeyron, 1834; Clausius, 1850). The combination of these two prop-

erties means that the water vapor greenhouse effect strongly increases with temperature which in turn reduces Earth's ability to restore its radiative balance. This way, water vapor roughly halves λ_{lwcs}, doubling S (Manabe and Wetherald, 1967; Hansen et al., 1984; Ingram, 2010).

Both the spectroscopic and thermodynamic properties of water vapor have been recognized since the 19$^{\text{th}}$ century, and subsequent studies have lead to a more quantitative and comprehensive understanding (e. g., Colman and Soden, 2021). However, to this day, uncertainties remain in the exact magnitude of both the absorption properties of water vapor (e. g., Shine et al., 2016) and the change of its abundance in a warming atmosphere (e. g., Sherwood et al., 2010). Given the dominant role of λ_{lwcs}, even small uncertainties in its underlying processes substantially affect our estimates of S. Therefore, the aim of this thesis is to better understand how uncertainties in both thermodynamic and spectroscopic properties of water vapor impact λ_{lwcs}.

Thermodynamic uncertainties arise because the Clausius-Clapeyron relation only provides an analytic description of how the equilibrium water vapor pressure e^* changes with temperature T. However, atmospheric water vapor pressure e is often prevented from reaching equilibrium between evaporation and condensation by the atmospheric general circulation, and thus relative humidity $R = e/e^*$ is generally below 100 %. Changes in the global distribution of R with warming are generally expected to be small; however, uncertainties remain regarding the sign, magnitude, and geographic distribution of these changes. These uncertainties largely stem from uncertainties in atmospheric dynamics, that is, shifts in circulation patterns with warming which have major implications for the global distribution of R (e. g., Bony et al., 2006; Sherwood et al., 2010; Romps, 2014; Colman and Soden, 2021).

In the first two projects of my PhD, I therefore use satellite observations to investigate how changes in R with warming affect λ_{lwcs}. For this purpose, I spectrally decompose λ_{lwcs} into the contributions of thermal radiation with different wavenumbers (frequencies) — the clear-sky spectral longwave feedback λ_ν. This spectral perspective is motivated by the fact that the absorption properties of greenhouse gases strongly vary spectrally. Hence, analyzing λ_{lwcs} in different parts of the radiation spectrum allows for differentiation between the effects of different greenhouse gases and for an investigation of feedback processes in different vertical layers of Earth's atmosphere (see Section 2.2.7). In my first project, I focus on Earth's global-mean λ_ν; in my second project, I investigate the T_s dependence of λ_ν. In both studies, I investigate how changes in surface and atmospheric temperature shape λ_ν, and I particularly focus on the role of changes in R with warming.

Spectroscopic uncertainties are generally among the smallest in the wider field of climate sciences. In large part, this is because the spectroscopic properties of greenhouse gases in Earth's atmosphere can largely be calculated from the first principles of quantum mechanics (e. g., Pierrehumbert, 2010). However, water vapor continuum absorption constitutes a notable exception to this rule. The continuum encompasses water vapor absorption that occurs due to poorly understood interactions of water vapor with other molecules in Earth's atmosphere, including both other water molecules and non-water molecules. To this day, water vapor continuum absorption is estimated semi-empirically and thus substantial uncertainty in its magnitude remains, which is estimated to be in the order of 10 %–30 % (e. g., Baranov et al., 2008; Mlawer et al., 2024, see also Section 2.2.3).

In my third project, I therefore investigate the impact of this uncertainty on λ_{lwcs}, as well as on $\mathcal{F}_{2\times CO_2}$ and $\mathcal{S}$, using a simple climate model. For this purpose, I adopt strongly idealized representations of both Earth's atmosphere and continuum uncertainty which allows me to concentrate on the most fundamental mechanisms. As before, I focus on spectrally decomposing the effect of this uncertainty on both λ_{lwcs} and $\mathcal{F}_{2\times CO_2}$ in order to further illuminate the underlying physical processes.

This unifying essay is structured as follows: In Chapter 2, I provide background information on climate feedbacks (Section 2.1) and on the radiation spectrum (Section 2.2). In the following chapters, I summarize the methodologies and results of the three projects that are part of this thesis. This includes my work on deriving the global-mean λ_v (Chapter 3), on analyzing the T_s dependence of λ_v (Chapter 4), and on investigating the effects of uncertainty in water vapor continuum absorption on λ_v (Chapter 5). In Chapter 6, I summarize and contextualize the central findings of my work, present my conclusions, and provide an outlook.

BACKGROUND

This chapter provides background information on radiative feedbacks in Earth's climate system and on the spectral dimension of thermal radiation.

2.1 CLIMATE FEEDBACKS

2.1.1 *Forcing-feedback framework*

To understand how Earth's climate responds to changes in atmospheric CO_2 concentration, it is useful to consider Earth's energy budget N at the top of the atmosphere. In equilibrium, Earth receives the same amount of energy from the sun as it re-emits to space. In such an equilibrium, $N = 0$ and thus Earth's global-mean near-surface air temperature T_s is stable, that is, $\Delta T_s = 0$.

This equilibrium can be perturbed in several different ways, including variations in the incoming solar radiation or reflective aerosols ejected by volcanic eruptions. However, most relevant in our context are changes in the atmospheric concentration of greenhouse gases, such as CO_2. An increase in atmospheric CO_2 reduces the amount of thermal radiation that Earth can emit to space, creating an imbalance in N. Such perturbations are commonly referred to as radiative forcing $\mathcal{F}$.

Following an increase in CO_2, Earth loses less energy than it receives and hence excess energy accumulates in Earth's climate system, leading to an increase in T_s. In a stable climate (see below), the energy Earth emits to space increases with warming, reducing the imbalance in N. The rate at which Earth's radiation budget changes per $1\,\mathrm{K}$ increase in T_s is called Earth's radiative feedback

$$\lambda = \frac{dN}{dT_s}. \tag{2.1}$$

These definitions follow the forcing-feedback framework which can be expressed as

$$N = \mathcal{F} + \lambda \Delta T_s. \tag{2.2}$$

Equation (2.2) demonstrates the fundamental distinction between forcing and feedback: The forcing $\mathcal{F}$ represents changes in N that occur *independently* of T_s, whereas the feedback λ represents changes in N that are *caused* by changes in T_s (e. g., Gregory et al., 2004).

After an increase in CO_2, T_s increases until $N = 0$, when a new equilibrium is reached. Climate sensitivity $\mathcal{S}$ is defined as the equilibrium change in T_s caused by the forcing of a doubling of the CO_2 concentration $\mathcal{F}_{2\times CO_2} \approx 3.7\,\mathrm{W\,m^{-2}}$. Rearranging Equation (2.2) gives

$$\mathcal{S} = T_{s,\,2\times CO_2} = -\frac{\mathcal{F}_{2\times CO_2}}{\lambda}. \tag{2.3}$$

It is important to note that this new equilibrium is only reached for a stabilizing radiative feedback ($\lambda < 0$). For a destabilizing radiative feedback ($\lambda \geqslant 0$), an increase in T_s does not reduce Earth's energy imbalance and thus causes a rapid increase in T_s — the so-called *runaway greenhouse effect* (e. g., Ingersoll, 1969; Komabayasi, 1967; Nakajima et al., 1992). However, Earth's current climate is well within the stable regime with a stabilizing $\lambda \sim \mathcal{O}(-1\,\mathrm{W\,m^{-2}\,K^{-1}})$.

2.1.2 *Radiative feedback*

As the name *feedback* suggests, λ describes processes that are caused by T_s changes but also *feed back* on T_s by altering N. These processes can broadly be split into three different categories:

THE CLEAR-SKY LONGWAVE FEEDBACK λ_{lwcs} comprises changes in absorption and emission of thermal radiation under clear skies due to changes in temperature and humidity. This strongly stabilizing feedback ($\lambda_{\mathrm{lwcs}} \ll 0$) is the focus of this thesis and further discussed in Section 2.1.3.

THE CLEAR-SKY SHORTWAVE FEEDBACK λ_{swcs} comprises changes in absorption of solar radiation under clear skies. This includes changes in surface albedo, mainly due to sea ice (Budyko, 1969), as well as changes in absorption of solar radiation by atmospheric water vapor (Zhang et al., 1994). Both of these feedbacks are destabilizing ($\lambda_{\mathrm{swcs}} > 0$), but of much smaller magnitude than λ_{lwcs}.

CLOUDS   affect λ in two different ways. (1) The mere presence of clouds can affect the clear-sky feedback through *cloud climatology effects* (Yoshimori et al., 2020): Clouds can mask and thus dampen a strongly stabilizing λ_{lwcs} (McKim et al., 2021) or a destabilizing λ_{swcs} (Sledd and L'Ecuyer, 2019); but they can also amplify λ_{lwcs}, for example in the case of low-level clouds above a moist boundary layer (Stevens and Kluft, 2023), or due to cloud-induced radiative heating (Mosso et al., 2024). (2) Changes in cloud amount, altitude, or optical depth with T_s induce changes in both shortwave and longwave radiation — so-called cloud feedbacks (e. g., Ceppi et al., 2017; Zelinka et al., 2020). Many of these cloud effects on λ still exhibit substantial uncertainty regarding both their sign and magnitude (e. g., Sherwood et al., 2020; Siebesma et al., 2020).

2.1.3 *Clear-sky longwave feedback*

This section contains more information on the clear-sky longwave feedback λ_{lwcs} which is the main focus of this thesis. It quantifies the change in clear-sky outgoing longwave radiation $\mathcal{L}_{\text{cs}}$ with T_{s} as

$$\lambda_{\text{lwcs}} = -\frac{d\mathcal{L}_{\text{cs}}}{dT_{\text{s}}}, \tag{2.4}$$

where the negative sign accounts for the fact that $\mathcal{L}_{\text{cs}}$ represents an energy loss to Earth's climate system, following the convention that stabilizing feedbacks are negative. In the following, I refer to λ_{lwcs} and $\mathcal{L}_{\text{cs}}$ as λ and $\mathcal{L}$, respectively.

The central role of λ has been recognized since the early days of climate modeling (e. g., Manabe and Wetherald, 1967; Budyko, 1969). It is by far the strongest radiative feedback with a magnitude of around $-2 \pm 0.2\,\text{W}\,\text{m}^{-2}\,\text{K}^{-1}$ (Sherwood et al., 2020). Consequently, even the comparatively small relative uncertainty in λ of $\pm10\,\%$ has a substantial effect on the total radiative feedback, from now on referred to as λ_{tot}. This small relative uncertainty stems from the fact that, compared to other feedbacks, the underlying physics of λ is well-understood and can even be described analytically (Koll et al., 2023). For these reasons, λ is a suitable prior for λ_{tot} and can be used as a reference to, for example, study the effects of clouds (Stevens and Kluft, 2023).

Traditionally, investigations of λ have considered temperature T and specific humidity q as their state variables. Following this framework, λ is split into three components:

THE PLANCK FEEDBACK   comprises the radiative effects of uniform warming of Earth's surface and atmosphere while keeping q constant. Because warmer bodies emit more thermal radiation (see Section 2.2.2), this is a strong stabilizing feedback.

THE WATER VAPOR FEEDBACK   comprises the radiative effects of changes in q. Because q strongly increases with temperature and water vapor is a potent greenhouse gas, this is a strong destabilizing feedback.

THE LAPSE RATE FEEDBACK   comprises the radiative effects of a non-uniform warming of the atmosphere. To first order, the tropospheric lapse rate follows a moist adiabatic lapse rate and thus the upper troposphere warms more strongly than the surface. This increases the amount of thermal radiation emitted to space for a given surface warming, making it a stabilizing feedback. However, this additional atmospheric warming also causes a stronger increase in q in the upper troposphere which in turn amplifies the destabilizing water vapor feedback.

However, this traditional feedback decomposition has a number of disadvantages. Most fundamentally, q strongly depends on temperature due to the Clausius-Clapeyron relation and thus constant q under temperature changes is not a good null hypothesis (Jeevanjee et al., 2022). When T is decreased, constant q can thus lead to values larger than the equilibrium value q*, a state that is physically unrealizable on large scales (Held and Shell, 2012). Hence, pioneering studies on Earth's ice ages already used the null-hypothesis of constant relative humidity $\mathcal{R}$ instead (e. g., Arrhenius, 1896).

This null-hypothesis of constant $\mathcal{R}$ is further supported by theoretical, modeling, and observational studies that have found $\mathcal{R}$ to change little with warming (e. g., Held and Soden, 2000; Bony et al., 2006; Sherwood et al., 2010; Romps, 2014; Colman and Soden, 2021). The global distribution of $\mathcal{R}$ is governed by the general circulation, as described for example by the advection-condensation paradigm (Sherwood, 1996; Pierrehumbert et al., 2008). Although changes in circulation patterns with warming are still uncertain (e. g., Shepherd, 2014; Bony et al., 2015), both models and observations tend to show increasing $\mathcal{R}$ with warming around the tropical tropopause and decreasing $\mathcal{R}$ in the subtropical mid-troposphere. However, these changes are expected to be in the order of $\pm 1\,\%\,K^{-1}$ and thus relatively small compared to the changes in q with warming, particularly in the global mean (Sherwood et al., 2010; Colman and Soden, 2021).

Moreover, the effect of the lapse rate feedback on the water vapor feedback causes considerable negative correlation between the two feedbacks in climate models, limiting the usefulness of this decomposition. This is resolved by adopting a combined water vapor lapse rate feedback, but inconsistencies remain as the water vapor feedback includes all changes in q but the lapse rate feedback only includes changes in T that are not vertically uniform (Jeevanjee et al., 2022).

Therefore, it has been proposed to use a feedback decomposition based on $\mathcal{R}$ rather than q (Held and Shell, 2012; Ingram, 2012, 2013). This decomposition also yields three feedback components:

THE PLANCK FEEDBACK   comprises the radiative effects of a uniform warming while holding $\mathcal{R}$ constant. It is still strongly stabilizing, but less so than the traditional Planck feedback.

THE RELATIVE HUMIDITY FEEDBACK   comprises the radiative effects of changes in $\mathcal{R}$. It is much weaker than the traditional water vapor feedback and its sign depends on the sign of the change in $\mathcal{R}$.

THE LAPSE RATE FEEDBACK   comprises the radiative effects of non-uniform warming and the additional q change required to keep $\mathcal{R}$ constant. It is usually slightly stabilizing but much weaker than the traditional lapse rate feedback.

This relative humidity framework provides a more physically consistent decomposition of λ. It has also received further support due to the natural way by which it incorporates the behavior of the clearsky spectral longwave feedback λ_ν, in particular *Simpson's law* (see Sections 2.2.6 and 2.2.7).

In this thesis, I do not explicitly decompose λ into its feedback components, but rather focus on analyzing λ_ν (see Section 2.2.7). In this framework, it is useful to instead split λ into a *surface feedback* that encompasses changes in $\mathcal{L}$ due to changes in T_s only, and an *atmospheric feedback* that encompasses changes in $\mathcal{L}$ due to changes in atmospheric temperature and humidity (Jeevanjee et al., 2021a, see also Sections 2.2.4 and 2.2.7). However, throughout this thesis, I follow the spirit of the relative humidity framework by analyzing λ_ν with respect to changes in T and $\mathcal{R}$.

2.2 RADIATION SPECTRUM

Electromagnetic radiation is inherently spectral in nature; yet, this spectral dimension is often neglected in the context of climate feedbacks. This section therefore provides some background on the spectral nature of thermal radiation and its interaction with Earth's atmosphere, as well as its relevance for Earth's climate.

2.2.1 *Radiation quantities*

Different coordinates are used to describe the spectral dimension of radiation. In this thesis, all spectral quantities are expressed in terms of wavenumber ν, with the unit cm^{-1}. Wavenumber ν is proportional to the frequency f of electromagnetic radiation as $\nu = f/c$, where c is the speed of light, meaning that increasing ν corresponds to electromagnetic radiation with increasing energy.

There are two different radiation quantities relevant for this thesis:

SPECTRAL RADIANCE I_ν quantifies the intensity of radiation of a certain wavenumber that originates from a certain solid angle in units of $\mathrm{W\,m}^{-2}\,(\mathrm{cm}^{-1})^{-1}\,\mathrm{sr}^{-1}$. This is the quantity directly measured by satellites and natively used in many radiative transfer models.

SPECTRAL FLUX F_ν quantifies the energy flow of radiation with a certain wavenumber through an area in units of $\mathrm{W\,m}^{-2}\,(\mathrm{cm}^{-1})^{-1}$. It is derived from I_ν by integrating over all zenith and azimuth angles. This is the quantity relevant for climate studies; the most important example used in this thesis is the clear-sky spectral outgoing longwave radiation $\mathcal{L}_\nu$, the upwelling thermal F_ν at the top of the atmosphere in the absence of clouds.

2.2.2   *Blackbody radiation*

A blackbody is an object that absorbs all incoming radiation and emits the maximum radiation possible, proportional to the fourth power of its temperature (Stefan, 1879; Boltzmann, 1884). The spectral radiance emitted by a blackbody is described by the Planck law

$$B_\nu(T) = 2h\nu^3 c^2 \frac{1}{e^{\frac{hc\nu}{k_B T}} - 1}, \tag{2.5}$$

where c is the speed of light, h is the Planck constant, and k_B is the Boltzmann constant. As T increases, B_ν increases throughout the spectrum and maximum emission shifts to higher ν (Planck, 1901).

At temperatures observed on Earth, most of this radiation is emitted in the thermal infrared, also referred to as longwave or terrestrial radiation, which roughly spans from $10\,\text{cm}^{-1}$ to $3000\,\text{cm}^{-1}$. However, about 99 % of Earth's outgoing longwave radiation $\mathcal{L}$ is emitted between $50\,\text{cm}^{-1}$ and $2000\,\text{cm}^{-1}$ (Stevens and Kluft, 2023). In contrast, due to its much higher temperature, most of the radiation emitted by the sun lies at much higher ν in the near-infrared and visible spectral ranges, also referred to as shortwave or solar radiation.

However, most real-world bodies absorb and emit less radiation than blackbodies. This is quantified by their spectrally varying absorptivity a_ν and emissivity ε_ν. For each zenith angle θ and azimuth angle ϕ, Kirchhoff's law states that, in thermodynamic equilibrium,

$$\varepsilon_\nu(\theta, \phi) = a_\nu(\theta, \phi) \leqslant 1, \tag{2.6}$$

meaning that a body's absorptivity is equal to its emissivity, and no body can absorb or emit more than a blackbody (Kirchhoff, 1860).

2.2.3   *Absorption and emission by greenhouse gases*

Unlike blackbodies, greenhouse gases absorb and emit radiation only at specific spectral lines, with ν determined by the quantum mechanical properties of each gas. In the infrared, absorption and emission occurs due to transitions between different quantized rotational and vibrational energy states of the molecules which are associated with different electric dipoles. In many cases, these energy states — and thus the spectral lines — can be calculated from the first principles of quantum mechanics; for more complex molecules they are derived from laboratory measurements. Overall, this makes spectroscopy one of the best understood disciplines in the wider field of climate sciences (Pierrehumbert, 2010).

In Earth's atmosphere, spectral lines have finite widths due to different broadening mechanisms. Pressure broadening, the dominant mechanism for thermal radiation in most parts of the atmosphere, occurs due to collisions between molecules that limit the lifetime

of their excited states. Following Heisenberg's uncertainty principle, this leads to uncertainty in the energy difference between the different states and thus in the frequency of the line. Doppler broadening, mostly relevant at high altitudes and high wavenumbers, occurs due to the thermal movement of molecules which causes their lines to shift due to the Doppler effect (Liou, 2002).

Furthermore, interactions between molecules can also modify their electric dipoles and thus their radiative properties which is particularly relevant for water vapor due to its permanent dipole. For example, these modified dipoles lead to absorption in the far-wing, far away from the line center. Furthermore, two water molecules can form dimers, weakly bound complexes with absorption properties that differ from those of single water molecules. Due to the highly complex nature of these processes, they cannot yet be calculated from first principles. Instead, these processes are subsumed in the water vapor continuum, a spectrally smooth absorption component that is still estimated by relying on semi-empirical fits based on laboratory measurements and field observations. Consequently, uncertainty in the magnitude of the continuum is still in the order of 10 %–30 %, much larger than other spectroscopic uncertainties (Baranov et al., 2008; Shine et al., 2016; Mlawer et al., 2024).

The water vapor continuum is usually split into two components that differ in their dependence on water vapor volume mixing ratio x: The foreign continuum encompasses interactions between water and non-water molecules and thus depends linearly on x; the self continuum encompasses interactions between two water molecules and thus depends quadratically on x. Furthermore, the self continuum decreases with increasing temperature T, whereas the foreign continuum features no known T dependence (Burch and Alt, 1984; Shine et al., 2016; Mlawer et al., 2023).

2.2.4 *Opacity and emission level*

The infrared clear-sky atmospheric radiative transfer in this thesis is well described by Schwarzschild's equation for a non-scattering medium (Schwarzschild, 1914). To describe $\mathcal{L}_\nu$, its integral form can be written as

$$\mathcal{L}_\nu = \varepsilon_{\nu,s} \, B_\nu(T_s) \, e^{-\tau_\nu(0,\infty)} + \int_{z=0}^{\infty} \alpha_\nu(z) \, B_\nu[T(z)] \, e^{-\tau_\nu(z,\infty)} \, dz. \quad (2.7)$$

Here, $\varepsilon_{\nu,s}$ is the emissivity of the surface, $\alpha_\nu(z)$ is the atmospheric absorption coefficient, $z = 0$ and $z = \infty$ refer to the surface and the top of the atmosphere, respectively, and the spectrally resolved opacity τ_ν between levels z and ∞ is defined as

$$\tau_\nu(z, \infty) = \int_z^{\infty} \alpha_\nu(z) dz. \quad (2.8)$$

The first term in Equation (2.7) denotes radiation emitted by Earth's surface and attenuated by atmospheric absorption. The second term denotes radiation emitted by the different atmospheric layers and attenuated by the atmospheric layers aloft.

Based on Equation (2.7), one can identify two different limits. In the optically thin limit ($\tau \to 0$), the atmosphere does not interact with radiation, thus all radiation emitted by the surface passes through the atmosphere unimpeded and $\mathcal{L}_\nu$ is entirely determined by the surface. In the optically thick limit ($\tau \to \infty$), the atmosphere absorbs all radiation emitted by the surface and re-emits radiation based on its temperature and thus $\mathcal{L}_\nu$ is entirely determined by the atmosphere. Between those limits, the optically thin regime encompasses all cases where $\tau_\nu < 1$ and the optically thick regime encompasses all cases where $\tau_\nu > 1$.

The fraction of radiation that passes through Earth's atmosphere without being absorbed is quantified by its transmissivity

$$t(z, \infty) = e^{-\tau(z,\infty)}. \tag{2.9}$$

Due to the exponential nature of Equation (2.9), $t < 1\,\%$ for $\tau \geqslant 5$, but $t > 90\,\%$ for $\tau \leqslant 0.1$. Consequently, radiation emitted from atmospheric layers with $\tau(z, \infty) \gg 1$ is mostly absorbed aloft; conversely only little radiation is emitted in atmospheric layers with $\tau(z, \infty) \ll 1$. Therefore, most outgoing radiation originates from a layer where $\tau(z, \infty)$ is high enough to emit sufficient radiation, but low enough so that little of it is absorbed aloft. As a convenient rule of thumb, this *emission level* is located where $\tau(z, \infty) \approx 1$ (e. g., Thomas and Stamnes, 2002; Jeevanjee and Fueglistaler, 2020).

This emission level strongly varies spectrally and can be calculated separately for each absorption species. Consequently, atmospheric emission at wavenumber ν is mostly controlled by the atmospheric species with the highest emission level at that ν. This can be expressed both in terms of *emission fraction* (Section C.2.4) and the *first-to-1 model* (Stevens and Kluft, 2023).

2.2.5 *Spectral outgoing longwave radiation*

Absorption by various greenhouse gases in Earth's atmosphere displays distinct spectral characteristics (Figure 2.1a). Consequently, different parts of the thermal infrared spectrum behave differently depending on the dominant absorption species, that is, their emission levels vary (Figure 2.1b), which has direct implications for $\mathcal{L}_\nu$ (Figure 2.1c). Therefore, it is convenient to split the thermal infrared into different spectral bands with distinct radiative properties. The exact boundaries of these bands vary slightly in the literature and even among the papers included in this thesis. Generally, the major spectral bands can be defined as follows:

WATER VAPOR ABSORPTION BANDS   These spectral regions are dominated by many different water vapor lines that form two main water vapor bands in the thermal infrared: A purely rotational band in the far-infrared ($\approx$100 cm^{-1}–550 cm^{-1}) and a vibrational-rotational band in the mid-infrared ($\approx$1250 cm^{-1}–2000 cm^{-1}). Except for narrow absorption bands of CH_4 and N_2O around 1300 cm^{-1}, water vapor is the only relevant greenhouse gas in these bands. These water vapor bands are usually optically thick (Figure 2.1a) and thus $\mathcal{L}_\nu$ is mostly sensitive to the middle and upper troposphere (Figure 2.1b). Consequently, global-mean $\mathcal{L}_\nu$ is substantially lower than the emission of a blackbody at global-mean $T_s = 288$ K (Figure 2.1c). However, in cold and dry conditions, the band flanks can become optically thin which means that surface emission can pass through the atmosphere and escape to space.

CO_2 ABSORPTION BANDS   There are two vibrational CO_2 absorption bands in the thermal infrared in which CO_2 is optically thick and the dominant absorber (Figure 2.1a). In the center of these bands, the emission level is located in the stratosphere (Figure 2.1b) and hence $\mathcal{L}_\nu$ is strongly reduced compared with surface emission (Figure 2.1c). As τ_ν decreases towards the band flanks, $\mathcal{L}_\nu$ becomes sensitive to the troposphere and $\mathcal{L}_\nu$ increases. The only major influence on Earth's climate comes from the band at $\approx$550 cm^{-1}–750 cm^{-1}, due to its location close to the maximum of Earth's thermal emission.

ATMOSPHERIC WINDOWS   Between these absorption bands, there are spectral regions where absorption is orders of magnitude weaker and the atmosphere is optically thin (Figure 2.1a). Because most surface emission can pass through the atmosphere without being absorbed, $\mathcal{L}_\nu$ in these bands is very similar to surface emission (Figure 2.1c). The most important window for Earth's climate is located in the mid-infrared ($\approx$750 cm^{-1}–1250 cm^{-1}), separated into two parts by an ozone absorption band (see below). This window accounts for approximately 25 % of $\mathcal{L}$ and an even larger fraction of λ (see Section 2.2.7). Nevertheless, some absorption does occur in the windows by both water vapor lines and the water vapor continuum. In warm and moist conditions, this absorption can become substantial and can even make the window optically thick (see Section 2.2.7).

O_3 ABSORPTION BAND   As mentioned above, the mid-infrared window is separated into two parts by a narrow band of ozone (O_3) absorption ($\approx$990 cm^{-1}–1080cm cm^{-1}). Most O_3 is located in the stratosphere and thus $\mathcal{L}_\nu$ in this band is sensitive to the stratosphere. However, the band also contains optically thin regions that are sensitive to the surface.
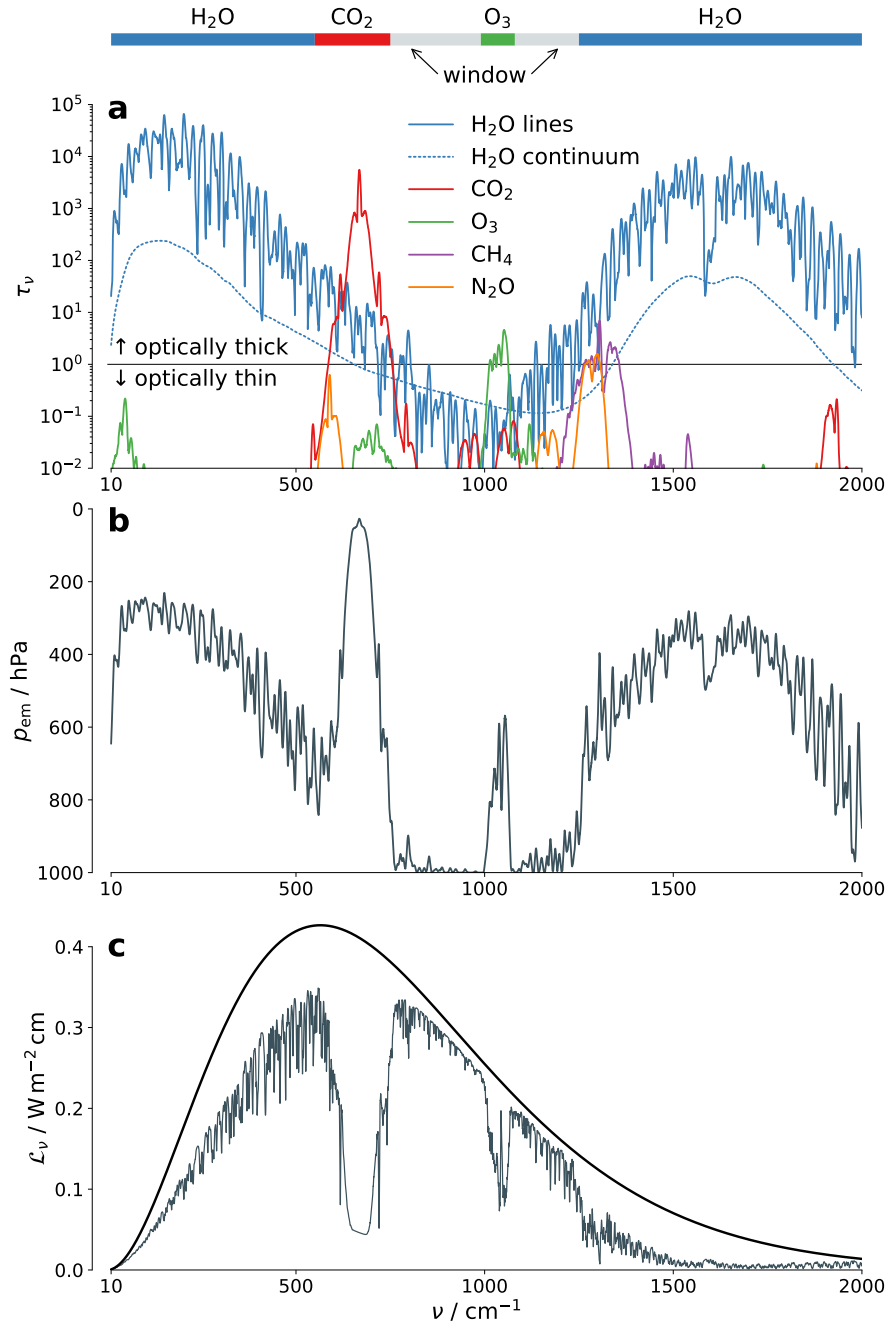
Figure 2.1: The thermal radiation spectrum: (a) Clear-sky spectral opacity τ_ν as a function of wavenumber ν of the most important greenhouse gases in Earth's atmosphere ($100\,cm^{-1}$ moving average). Above, the spectral bands described in Section 2.2.5 are shown. (b) Spectral emission pressure p_{em} of clear-sky spectral outgoing longwave radiation $\mathcal{L}_\nu$ ($100\,cm^{-1}$ moving average). Note that the tropospheric emission level in the O_3 band is the result of spectrally averaging p_{em} from both surface and stratosphere. (c) $\mathcal{L}_\nu$ for a surface temperature $T_s = 288\,K$ ($25\,cm^{-1}$ moving average), with the corresponding Planck curve for reference.

2.2.6   *Simpson's law*

An important phenomenon in atmospheric radiative transfer is the fact that under certain conditions, $\mathcal{L}_\nu$ decouples from the surface. Following Jeevanjee et al. (2021a), I will refer to this phenomenon as *Simpson's law*, in honor of the seminal work of Simpson (1928a,b) who first described this somewhat counterintuitive behavior.

Simpson's law applies under a number of assumptions:

1. Water vapor absorption is optically thick ($\tau \gg 1$) and absorption by other greenhouse gases is negligible;

2. water vapor absorption only depends on the water vapor pathlength, which in turn is proportional to the integral of specific humidity q over pressure p;

3. both relative humidity $\mathcal{R}$ and temperature lapse rate Γ are fixed functions of atmospheric temperature T, that is, they do not change with warming.

The profile of q — and thus the water vapor pathlength — only depends on $\mathcal{R}$ and T. Therefore, if $\mathcal{R}$ and Γ are fixed functions of T, then so is the water vapor pathlength. Thus, if water vapor absorption only depends on the water vapor pathlength (and no other greenhouse gas contributes) then $\tau(z, \infty)$ between level $z(T)$ and the top of the atmosphere is also only a function of T. Consequently, the emission level of $\mathcal{L}_\nu$, the level where $\tau(z, \infty) \approx 1$, will always be located at the same T. In other words, the emission temperature is constant and, therefore, so is $\mathcal{L}_\nu$ (Ingram, 2010; Jeevanjee et al., 2021a).

A necessary prerequisite for Simpson's law is the fact that q increases with T due to the Clausius-Clapeyron relation. Therefore, under constant $\mathcal{R}$, the increased atmospheric emission of a warmer atmosphere is approximately compensated by the increased atmospheric absorption of water vapor. Thus, water vapor acts as an *insensitive emitter*, whose emission is largely invariant with T_s to first order; whereas other greenhouse gases, such as CO_2, act as *sensitive emitters*, whose emission increases with T_s as long as their emission levels are located in the troposphere (Stevens and Kluft, 2023, see also Section 2.2.7).

Contrary to its name, Simpson's law is only a first-order approximation. This is because Earth's atmosphere deviates from most of the assumptions listed above:

1. The assumption that water vapor is optically thick and absorption by other gases is negligible is mostly fulfilled in the water vapor bands; however, it is obviously not fulfilled in the atmospheric window and in absorption bands of other greenhouse gases (see Section 2.2.5).

2. The assumption that water vapor absorption only depends on the water vapor pathlength is only fulfilled to first order. This is because it neglects the effects of pressure broadening (see Section 2.2.3) which redistributes absorption away from the line centers. For very strong lines where absorption is saturated in the line center, this redistribution means that the spectrally integrated τ increases with p. Consequently, the emission pressure decreases less strongly in a warmer atmosphere than predicted by constant emission temperature T_{em}. This results in a non-negligible increase with T_s in T_{em} — and thus in $\mathcal{L}_\nu$ — in the water vapor bands (e. g., Ingram, 2010; Feng et al., 2023a).

3. First, the assumption that $\mathcal{R}$ is a fixed function of T implies that the profile of $\mathcal{R}(T)$ is invariant with warming, which is broadly supported by numerous studies showing that $\mathcal{R}$ changes little under warming (see Section 2.1.3). However, even relatively small changes in $\mathcal{R}$ with warming can have a substantial effect on Simpson's law and thus on λ. This is analyzed and discussed in depth in the first two studies of my PhD (Chapters 3 and 4, Appendices A and B). Second, Γ is not a fixed function of T because in the troposphere, it to first order follows a moist adiabatic lapse rate which depends not only on T but also on p. The effects on λ of different assumptions about Γ and its changes in a warming climate are analyzed in the second study of my PhD (Chapter 4, Appendix B).

Despite these limitations, Simpson's law has proven very useful in climate studies. For example, it is a useful heuristic to understand the spectral longwave feedback, and it provides further support to adopt the relative humidity based feedback decomposition.

2.2.7   *Spectral feedback*

The preceding sections demonstrate how the radiative properties of Earth's atmosphere vary spectrally and how this spectral dimension maps onto different absorbing species and the vertical dimension of Earth's atmosphere. They also highlight that different spectral regions behave differently under warming, because some are much more sensitive to T_s than others. However, all of these details and subtleties are lost in the traditional way λ is often analyzed: as a *gray*, spectrally integrated, quantity.

To better understand the physical feedback processes that govern λ, investigating its spectral dimension offers valuable insights. To this end, one can define the clear-sky spectral longwave feedback as

$$\lambda_\nu = -\frac{d\mathcal{L}_\nu}{dT_s}, \tag{2.10}$$

whose spectral integral yields the broadband feedback $\lambda = \int \lambda_\nu \, d\nu$.

As indicated above, analyzing λ_ν provides a number of advantages over the spectrally integrated λ. First, it allows to easily separate the radiative effects of different greenhouse gases based on the different spectral distributions of their absorption. Second, it allows to pinpoint the vertical atmospheric layer a given radiative signal originates from and thus make statements about the vertical distribution of feedback processes in the atmosphere. For this, one can make use of the fact that $\mathcal{L}_\nu$ originates from different atmospheric regions in different parts of the spectrum (see Section 2.2.5, Figure 2.1b). Much of this information is lost when only analyzing the spectrally integrated λ: Due to compensating effects between different spectral bands, very different λ_ν can yield similar λ (e. g., Huang et al., 2014).

Furthermore, these different spectral regions exhibit very different λ_ν. First, in the H_2O bands, λ_ν to first order follows Simpson's law which predicts a roughly constant $\mathcal{L}_\nu$ and thus a near-zero λ_ν under constant $\mathcal{R}$ (see Section 2.2.6, also e. g., Jeevanjee et al., 2021a). This way, water vapor absorption *spectrally masks* the stabilizing surface feedback (Stevens and Kluft, 2023). However, real-world deviations from Simpson's law also manifest in λ_ν which is a major theme throughout this thesis (see Chapters 3 and 4, Appendices A and B).

Second, a large part of the feedback originates in the atmospheric window where changes in surface emission directly translate to changes in $\mathcal{L}_\nu$ (see Sections 2.2.4 and 2.2.5). Therefore, λ_ν in the window is dominated by the surface feedback, whereas the optically thin atmosphere only leads to a weak atmospheric feedback (e. g., Jeevanjee et al., 2021a; Koll et al., 2023).

Third, λ_ν strongly varies within the CO_2 bands: In the band centers, $\mathcal{L}_\nu$ is sensitive to the stratosphere whose temperature is to first order independent of T_s. Thus, CO_2 behaves as an *insensitive emitter*, yielding near-zero λ_ν in the band centers. At the band flanks, $\mathcal{L}_\nu$ is sensitive to the troposphere whose temperature increases with T_s. Thus, CO_2 behaves as a *sensitive emitter*, yielding a substantially stabilizing atmospheric λ_ν at the band flanks (see Section 2.2.6, also e. g., Seeley and Jeevanjee, 2021; Kluft et al., 2021; Stevens and Kluft, 2023).

Finally, λ_ν depends on the background climate, usually quantified by T_s. Most of this T_s dependence again arises from the fact that q strongly increases with T_s which affects the radiative properties of Earth's atmosphere throughout the longwave spectrum. Most prominently, at $T_s \approx 300\,K$, the mid-infrared atmospheric window becomes optically thick. This strongly weakens the stabilizing λ_ν in this spectral region because the strongly stabilizing surface feedback is now masked by water vapor absorption and is even replaced by a weakly destabilizing atmospheric feedback caused by the water vapor continuum which dominates absorption in the window (e. g., Koll et al., 2023). This process is commonly referred to as the *closing* of the atmospheric window (see Chapter 5, Appendix C).

3

OBSERVATION OF EARTH'S GLOBAL-MEAN SPECTRAL LONGWAVE FEEDBACK (PAPER 1)

To date, most research on Earth's longwave feedback λ has been limited to its spectral integral (e.g., Hansen et al., 1984; Sherwood et al., 2020). However, studying the spectrally resolved λ_ν provides deeper insights into the underlying feedback mechanisms (see Section 2.2.7). Yet, the global-mean λ_ν has only been investigated in model studies (e.g., Huang et al., 2014; Kluft et al., 2019; Jeevanjee et al., 2021a). Therefore, this study closes this gap by deriving the first observational estimate of λ_ν, using satellite observations of short-term variability. With this, I address two main research questions:

1. How does the observed λ_ν compare to model studies?

2. What are the physical processes responsible for deviations from model studies?

3.1 OBSERVING THE SPECTRAL LONGWAVE FEEDBACK

A major challenge in deriving radiative feedbacks from satellite observations is that observational time series are usually much shorter compared with model studies. This makes trends derived from these observations more susceptible to effects of short-term variability (Zhou et al., 2016; Colman and Hanson, 2017). Instead, multiple studies have used this short-term variability directly to derive λ (e.g., Dessler, 2013; Dessler and Forster, 2018).

However, this approach comes with the challenge that feedbacks derived from short-term variability can differ from those derived from long-term trends which are relevant for global climate change (e.g., Dong et al., 2020; Zhou et al., 2015; Dessler, 2020). This not only concerns the spectrally integrated feedbacks, but also their spectral distribution (Huang et al., 2019). Nevertheless, studying the short-term λ_ν still offers valuable insights into the underlying feedback mechanisms, many of which are expected to be similar on short and long timescales.

I therefore derive λ_ν based on two different sources of short-term variability: Seasonal variability (the mean annual cycle), and interannual variability (deviations from the mean annual cycle). For this, I use satellite observations by the Infrared Atmospheric Sounding Interferometer (IASI) which provides outgoing spectral radiances I_ν in 8461 spectral channels between $645\,\mathrm{cm}^{-1}$ and $2760\,\mathrm{cm}^{-1}$ from 2007 through 2020 (EUMETSAT, 2018). I average and convert those instan-
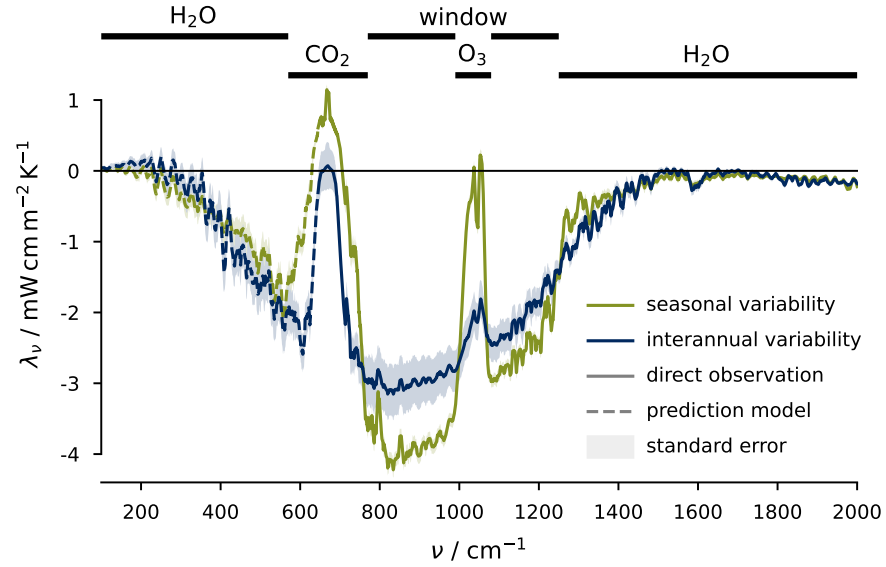
Figure 3.1: All-sky spectral longwave feedback λ_ν ($10\,\mathrm{cm}^{-1}$ moving average) inferred from satellite observations by the IASI instrument. Shown are the λ_ν calculated from seasonal variability (green) and interannual variability (blue). The solid lines represent the part of the spectrum covered by IASI, the dashed lines show the λ_ν in the far-infrared, which are estimated using a prediction model developed by Turner et al. (2015). Data are presented as mean values (lines) $\pm$ standard errors (shading). The ranges of different spectral bands are shown at the top. For better visibility, only the spectral range $100\,\mathrm{cm}^{-1}$–$2000\,\mathrm{cm}^{-1}$ is shown.

taneous I_ν to global monthly means of spectral outgoing longwave radiation $\mathcal{L}_\nu$, a spectral flux. To encompass most of the longwave spectrum, I extend $\mathcal{L}_\nu$ to the far-infrared spectral region ($100\,\mathrm{cm}^{-1}$–$645\,\mathrm{cm}^{-1}$) using a prediction model developed by Turner et al. (2015). To derive λ_ν, I then linearly regress these extended global monthly mean $\mathcal{L}_\nu$ spectra against near-surface air temperature T_s from the ERA5 reanalysis (Hersbach et al., 2019a).

These observations are made under all-sky conditions, and thus the derived λ_ν are a combination of the clear-sky λ_ν studied in this thesis and the effects of clouds (see Section 2.1.2). However, the observed all-sky λ_ν are in very good agreement with the clear-sky λ_ν that I calculate for simulated observations based on the MPI-ESM climate model (Jungclaus et al., 2019). This suggests that the observed λ_ν is dominated by the clear-sky feedback and the effect of clouds is of second order.

3.2 HOW WATER VAPOR SHAPES THE SPECTRAL LONGWAVE FEEDBACK

The observed λ_ν from seasonal and interannual variability (Figure 3.1) are similar to modeled λ_ν in their spectral integral and in the general spectral distribution. As expected, most of the feedback originates in the atmospheric window which is sensitive to surface warming, whereas the feedback in the absorption band of CO_2 sensitive to the stratosphere is close to zero (see Section 2.2.7). However, at closer inspection, there are notable differences in the spectral distribution between observed and modeled λ_ν. Most strikingly, the observations feature much more stabilizing (negative) λ_ν in the water vapor absorption bands in the mid-infrared ($1250\,\mathrm{cm}^{-1}$–$2000\,\mathrm{cm}^{-1}$) and far-infrared ($100\,\mathrm{cm}^{-1}$–$645\,\mathrm{cm}^{-1}$) compared with idealized model studies (Koll and Cronin, 2018; Jeevanjee et al., 2021a). I show that this discrepancy originates from two assumptions about atmospheric water vapor made in these models.

First, idealized model studies assume that relative humidity $\mathcal{R}$ is both vertically uniform and constant with surface temperature T_s. While the assumption of vertically uniform $\mathcal{R}$ only has a minor impact on λ_ν, neglecting changes in $\mathcal{R}$ with T_s has a substantial effect. In both seasonal and interannual variability, global mean $\mathcal{R}$ derived from ERA5 — which I use as a proxy for the observations — decreases with T_s by about $0.5\,\%\,\mathrm{K}^{-1}$ in the analyzed period. This change is well within the estimated change of $\mathcal{R}$ with T_s under climate change of about $\pm 1\,\%\,\mathrm{K}^{-1}$ (Sherwood et al., 2010). To estimate the effect of this $\mathcal{R}$ decrease on the observed λ_ν, I simulate λ_ν based on the single-column model konrad (Kluft et al., 2019; Dacie et al., 2019). I perform three different experiments in which I assume that $\mathcal{R}$ stays constant with warming, increases, and decreases with warming by $\pm 0.5\,\%\,\mathrm{K}^{-1}$, respectively. I find that even the relatively small $\mathcal{R}$ decrease seen in reanalysis strengthens the stabilizing λ_ν in the water vapor bands by about $30\,\%$ and the spectrally integrated λ by about $10\,\%$. This highlights the importance of accounting for changes in $\mathcal{R}$ with T_s, as even small changes substantially affect λ_ν.

Second, many previous studies on λ_ν were based on single-column models that represent Earth's atmosphere by one global-mean vertical column. In general, this approach is well-established and able to realistically reproduce λ (e. g., Manabe and Wetherald, 1967; Kluft et al., 2019). However, single-column models by design do not capture horizontal variations in temperature and humidity which determine the transmissivity of the atmosphere with respect to thermal radiation. The transmissivity in turn scales the surface feedback, the change in surface emission with warming that can escape to space without any atmospheric changes (see Sections 2.1.3 and 2.2.7). This is most obvious in the far-infrared water vapor band which is fully opaque

at temperatures similar to the global mean, meaning that that the surface feedback is zero. However, in cold regions with low specific humidities q, parts of this spectral region become optically thin and thus the stabilizing surface feedback is substantial in these regions. I demonstrate this by simulating the surface feedback based on the single-column model konrad for different T_s ranging from 268 K to 308 K. I assume the same $\mathcal{R}$ profile for all T_s and thus a strong increase in the vertically integrated q with temperature. I find that while the surface feedback is zero for $T_s \geqslant 288$ K, it is stabilizing for smaller T_s and thus also in the mean over all simulated T_s, which I use as a proxy for the global mean.

In the atmospheric window, the observed λ_ν from interannual variability is very similar to model studies, whereas the λ_ν from seasonal variability is more stabilizing. This can be explained by different warming patterns in those two short-term variabilities. Interannual variations of local T_s with global-mean T_s are distributed more or less uniformly globally, whereas the seasonal variations are much stronger over extratropical continents compared to the rest of the world. On average, the atmosphere over extratropical continents is drier and thus absorbs less surface emission compared with the global mean. This in turn favors a more stabilizing surface feedback — and thus a more stabilizing λ_ν in the atmospheric window.

In summary, the research questions of this study can be answered as follows:

1. The observed λ is consistent with previous studies, but the observed λ_ν is more stabilizing in the water vapor absorption bands compared to idealized models.

2. This discrepancy can be explained by changes in $\mathcal{R}$ with warming and the non-homogeneous global distribution of water vapor.

4

OBSERVATIONS OF THE SURFACE TEMPERATURE
DEPENDENCE OF EARTH'S SPECTRAL LONGWAVE
FEEDBACK (PAPER 2)

After the investigation of the global-mean spectral longwave feedback λ_ν in my first study, the second study of my PhD focuses on the dependence of the clear-sky λ_ν on surface temperature T_s. Similar to the global-mean λ_ν, investigations of this T_s dependence have so far been limited to model studies (e. g., Kluft et al., 2021; Seeley and Jeevanjee, 2021; Feng et al., 2023a; Koll et al., 2023). In this study, I close this gap by calculating λ_ν from satellite observations for T_s spanning from 210 K to 310 K, utilizing the large range of T_s on Earth's surface. This way, I address three main research questions:

1. How does the observed λ_ν vary with T_s?

2. Is it possible to reconstruct the observed $\lambda_\nu(T_s)$ using a single-column model of Earth's atmosphere?

3. How is the observed T_s dependence impacted by variations in atmospheric temperature and humidity induced by the general circulation?

4.1 THE RADIATIVE SIGNATURE OF THE GENERAL CIRCULATION

To calculate λ_ν as a function of T_s from satellite observations, I use a dataset of clear-sky spectral outgoing longwave radiation $\mathcal{L}_\nu$ based on observations by the AIRS instrument (Huang, 2020). This dataset provides monthly-mean $\mathcal{L}_\nu$ on a $2° \times 2°$ longitude-latitude grid from 2002 through 2022, covering the spectral range $10\,\mathrm{cm}^{-1}$–$2000\,\mathrm{cm}^{-1}$ with a spectral resolution of $10\,\mathrm{cm}^{-1}$. These observations cover a wide range of T_s which I split into ten regimes of $\Delta T_s = 10\,\mathrm{K}$ each, centered at 215 K, 225 K, . . . , 305 K. I linearly regress the spectral outgoing longwave radiation $\mathcal{L}_\nu$ against T_s for each regime and each spectral channel to calculate $\lambda_\nu(T_s)$.

The main challenge in deriving the T_s dependence of λ_ν from satellite observations lies in the fact that variations in T_s on Earth's surface coincide with variations in atmospheric temperature and humidity. These variations are often not controlled by the local T_s alone but also affected by their location within different branches of the atmospheric general circulation (e. g., Feng et al., 2023b). Hence, the $\lambda_\nu(T_s)$ derived from satellite observations not only contain the pure T_s dependence of λ_ν but also the radiative signature of these circulation-induced variations in atmospheric temperature and humidity.

At the same time, this challenge provides the opportunity to test the current understanding of λ. Therefore, to study the impact of circulation-induced variations on $\lambda_\nu(T_s)$, I reconstruct the observed $\lambda_\nu(T_s)$ using simulated observations of $\mathcal{L}_\nu$ based on a simple single-column atmospheric model. I disentangle the effects of different atmospheric processes by performing the simulations in different model configurations representing different degrees of idealization. I perform four different experiments:

THE CONSTANT-$\mathcal{R}$ EXPERIMENT   Within each T_s regime, I assume that tropospheric relative humidity $\mathcal{R}$ is vertically uniform and constant with T_s, and that the temperature profiles T follow a moist-adiabatic lapse rate based on T_s. The column-mean $\mathcal{R}$ for each regime is calculated based on the ERA5 reanalysis (Hersbach et al., 2019b).

THE VARIABLE-$\mathcal{R}$ EXPERIMENT   I account for variations in $\mathcal{R}$ with T_s by calculating the column-mean $\mathcal{R}$ separately for each T_s based on ERA5.

THE CONSTANT-LR EXPERIMENT   The tropospheric temperature follows a constant lapse rate of $6.5\,\mathrm{K\,km^{-1}}$ which better captures the change in T with T_s in ERA5.

THE CLOSURE EXPERIMENT   For each T_s, the actual atmospheric profiles of $\mathcal{R}$ and T from ERA5 are used which accounts for vertical variations in $\mathcal{R}$ and the temperature lapse rate, as well as in their changes with T_s.

Based on each of these experiments, I simulate $\mathcal{L}_\nu$ using the line-by-line radiative transfer model ARTS (Eriksson et al., 2011; Buehler et al., 2018). Based on these $\mathcal{L}_\nu$, I calculate λ_ν for each T_s regime by linear regression, as described above for the observed λ_ν.

4.2   observed surface temperature dependence

The observed λ_ν strongly vary with T_s (Figure 4.1). Generally, they are in fairly good agreement with previous model studies (e. g., Kluft et al., 2021; Seeley and Jeevanjee, 2021; Koll et al., 2023). In the following, I compare the observed and simulated λ_ν at low T_s ($< 270\,\mathrm{K}$), intermediate T_s ($270\,\mathrm{K}$–$290\,\mathrm{K}$), and high T_s ($> 290\,\mathrm{K}$) and discuss the main processes impacting λ_ν.

At low T_s, the atmosphere is largely transparent and thus there is substantial feedback throughout most of the spectrum. With increasing T_s, specific humidity q increases which increases the atmospheric opacity due to water vapor absorption and thus weakens the stabilizing (negative) λ_ν. This first occurs in the centers of the water
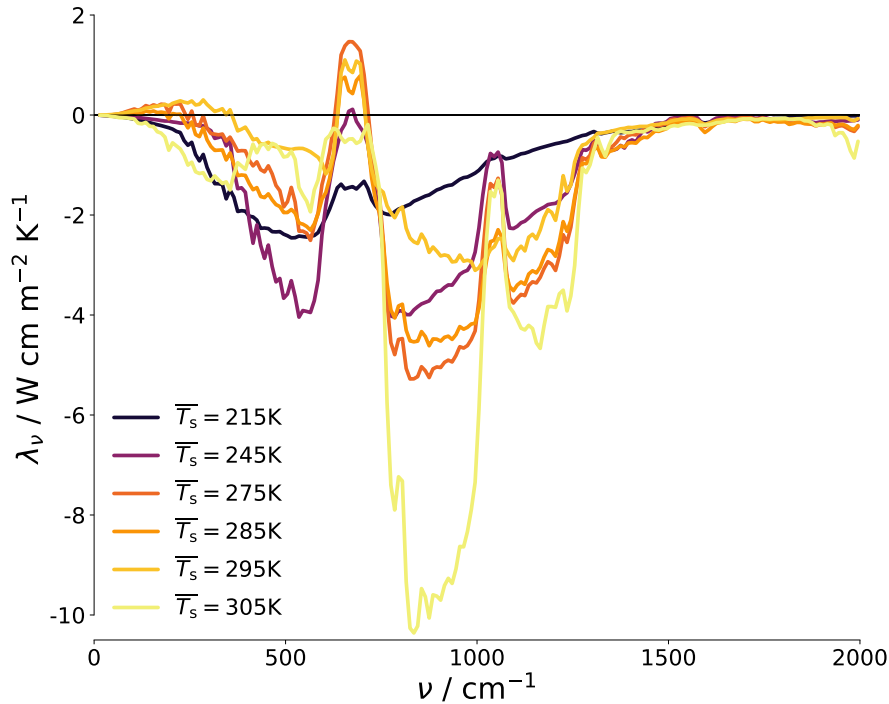
Figure 4.1: Observed spectral longwave feedback λ_ν for different near-surface air temperatures T_s.

vapor absorption bands ($T_s \approx 220\,\text{K}$), followed by the band flanks ($T_s \approx 250\,\text{K}$). As expected, λ_ν in this T_s range is mainly dominated by the surface feedback throughout the spectrum and hence sensitive to Earth's skin temperature T_{skin}, the temperature that determines thermal emission by the surface. However, the modeling reconstructions of the observed λ_ν suffer from known biases in the ERA5 reanalysis which substantially overestimates T_{skin} in polar regions (Trigo et al., 2015; Muñoz-Sabater et al., 2021). These biases are largest at very low T_s and decrease with increasing T_s which causes the reconstructed λ_ν to be less stabilizing than the observed λ_ν in large parts of the spectrum.

At intermediate T_s, the water vapor bands are optically thick meaning that the surface feedback there is zero and only the atmospheric feedback contributes to λ_ν. This atmospheric feedback is much weaker and thus the water vapor bands contribute less to the overall λ_ν compared to lower T_s. However, the water vapor bands are sensitive to changes in the profile of $\mathcal{R}$ with T_s. This becomes obvious when comparing the simulated λ_ν for the different experiments. The constant-$\mathcal{R}$ experiment that neglects these changes substantially underestimates λ_ν in the water vapor bands. The variable-$\mathcal{R}$ experiment, which accounts for the column-mean change in $\mathcal{R}$ with T_s, is able to capture the average feedback in the water vapor bands, as already seen in my first study (Chapter 3). However, this is the result of considerable spectral compensation within the band. This remaining dis-

crepancy is due to vertical variations in the $\mathcal{R}$ change with warming, because $\mathcal{R}$ at these T_s decreases in the mid-troposphere but increases in the upper troposphere. The discrepancy can be almost entirely resolved once these vertical variations are accounted for in the closure experiment. This demonstrates that the radiative signature of these vertical $\mathcal{R}$ variations directly maps onto the observed λ_ν.

At high T_s, the stabilizing λ_ν in the atmospheric window strongly varies between the regimes centered at 295 K and 305 K, respectively. Compared to intermediate T_s, $\lambda_\nu(295\,K)$ is less stabilizing because the exponentially increasing q initiates the closing of the atmospheric window. This process is further accelerated by the fact that $\mathcal{R}$ increases with T_s from the subtropics at 290 K to the inner tropics at 300 K. However, the opposite can be observed for $\lambda_\nu(305\,K)$, which is more than twice as stabilizing in the window. This is the signature of the strongly decreasing $\mathcal{R}$ with T_s between the moist inner tropics at 300 K and the very dry desert regions at 310 K, even featuring a decrease in q with T_s. This in turn causes the atmospheric window to abruptly *re-open* because more surface emission can escape to space at higher T_s, leading to a very strong surface feedback. Obviously, such extreme changes in $\mathcal{R}$ with warming are not realistic to occur under global climate change. Nevertheless, these results highlight the effect of these changes on λ_ν in different parts of the spectrum.

In summary, the research questions of this study can be answered as follows:

1. The observed λ_ν is stabilizing throughout the spectrum at low T_s, whereas most of it originates in the window at intermediate and high T_s.

2. The observed λ_ν at different T_s can be well reproduced using a single-column model of Earth's atmosphere.

3. At low T_s, λ_ν is mostly impacted by T_{skin}, while at intermediate and high T_s, λ_ν is strongly affected by variations in the $\mathcal{R}$ profiles with T_s induced by the general circulation. This effect is strongest the water vapor absorption bands, but also affects the atmospheric window.

EFFECT OF UNCERTAINTY IN WATER VAPOR CONTINUUM ABSORPTION ON EARTH'S SPECTRAL LONGWAVE FEEDBACK (PAPER 3)

In this chapter, I focus on the remaining uncertainty in water vapor continuum absorption, which is still in the order of 10 %–30 % (Baranov et al., 2008; Mlawer et al., 2024, see also Section 2.2.3) but has so far been primarily discussed within the field of spectroscopy (e. g. Shine et al., 2012, 2016). In the climate community, the discussion of continuum uncertainty has been mostly limited to its effect on outgoing longwave radiation $\mathcal{L}$ (Kiehl and Ramanathan, 1982; Paynter and Ramaswamy, 2011, 2012). To close this gap, I investigate the effect of continuum uncertainty on CO_2 radiative forcing $\mathcal{F}_{2\times CO_2}$ (in the following simply $\mathcal{F}$) and the clear-sky longwave feedback λ. I again focus particularly on the spectral dimension of these quantities to study the underlying processes and their implications for climate sensitivity $\mathcal{S}$. With this, I address three main research questions:

1. How do separate variations of self and foreign continuum absorption affect λ?

2. Through which physical processes does continuum uncertainty affect λ?

3. What does this imply for the effect of continuum uncertainty on the T_s dependence of $\mathcal{S}$?

5.1 EFFECT OF VARIATIONS IN SELF AND FOREIGN CONTINUUM

I use the single-column model konrad (Kluft et al., 2019; Dacie et al., 2019) to create atmospheric profiles of temperature and humidity for surface temperatures T_s between 270 K and 330 K. Based on these profiles, I use the line-by-line radiative transfer model ARTS (Eriksson et al., 2011; Buehler et al., 2018) to simulate the spectrally resolved $\mathcal{L}_\nu$, from which I in turn derive the spectrally resolved $\mathcal{F}_\nu$ and λ_ν.

The continuum consists of two components, the self and foreign continuum (see Section 2.2.3). To understand the different mechanisms by which they affect λ_ν, I separately vary self and foreign continuum by $\pm 10 \%$ compared to their baseline values in the MT_CKD continuum model (Mlawer et al., 2023). These variations of the continuum have a much stronger effect on λ than on $\mathcal{F}$, and thus the latter is not further discussed here (see Section C.3.1 for a detailed analysis). The effect on λ can be separately analyzed for the surface feedback and the atmospheric feedback (see Section 2.2.7).

Regarding the surface feedback, increasing continuum absorption causes a stronger attenuation of surface emission by the atmosphere which weakens the surface feedback in the optically thin atmospheric window. This is the case for both increases in self and foreign continuum, but the effect of the self continuum is about one order of magnitude stronger (Figure 5.1g,k). At at $T_s \approx 310\,\text{K}$, the window becomes optically thick and the surface feedback vanishes.

Regarding the atmospheric feedback, an increase in continuum absorption leads to a higher emission level which implies less atmospheric emission and thus lower $\mathcal{L}_\nu$. A stronger self continuum mostly reduces $\mathcal{L}_\nu$ at high T_s; hence, it weakens the overall increase of $\mathcal{L}_\nu$ with T_s which leads to a more destabilizing (positive) λ_ν. In contrast, a stronger foreign continuum mostly reduces $\mathcal{L}_\nu$ at lower T_s and thus has an opposite, stabilizing effect on λ_ν (Figure 5.1h,l).

These opposite effects of self and foreign continuum on the atmospheric feedback result from shifts in the absorption species that control atmospheric emission in different spectral regions as T_s increases. In short, the quadratic dependence of the self continuum on water vapor volume mixing ratio x means that its absorption features the strongest increase with T_s among all considered species, even stronger than the water vapor line absorption. This means that the self continuum controls atmospheric emission in more parts of the spectrum as T_s — and thus x — increases. In contrast, the linear dependence of the foreign continuum on x means that its absorption increases less strongly with T_s than water vapor line absorption. This means that it controls atmospheric emission in fewer parts of the spectrum as T_s increases.

5.2 EFFECT OF CONTINUUM UNCERTAINTY

To investigate the effect of continuum uncertainty, I have to consider that the uncertainties in self and foreign continuum are negatively correlated (e. g., Shine et al., 2016). To account for this, I represent real-world continuum uncertainty in an idealized way by assuming that the total continuum absorption τ_{cont} is perfectly constrained, and thus an increase in the self continuum leads to an equal decrease in the foreign continuum, and vice versa.

In this context, the previous assumption of a symmetric self continuum uncertainty of $\pm 10\,\%$ is physically inconsistent. This is because in the atmospheric window, the self continuum is several orders of magnitudes stronger than the foreign continuum. Thus, even eliminating foreign continuum absorption τ_{foreign} entirely would not suffice to compensate a $10\,\%$ increase in the self continuum absorption τ_{self}. In the following, I thus only consider the case were τ_{self} is decreased by $10\,\%$ and τ_{foreign} is increased accordingly.
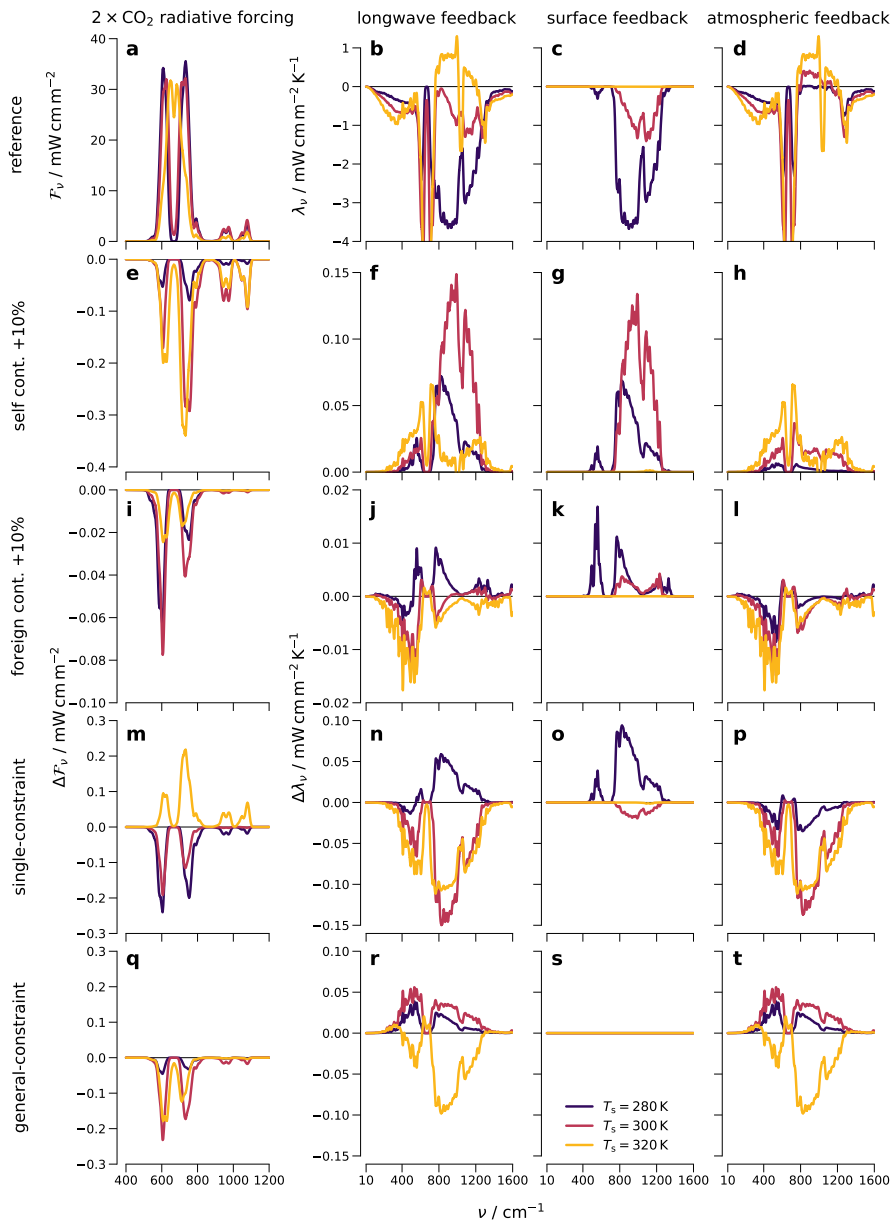
Figure 5.1: Spectrally-resolved effect of water vapor continuum absorption on CO_2 forcing $\mathcal{F}_\nu$ (a, e, i, m, q) and longwave feedback λ_ν (b, f, j, n, r), which is also decomposed into surface feedback (c, g, k, o, s) and atmospheric feedback (d, h, l, p, t) for surface temperatures T_s of 280 K (black), 300 K (red), and 320 K (yellow). Shown are the baseline values (a–d), and the effects of 10 % increase in self continuum absorption (e–h) and foreign continuum absorption (i–l). Finally, the results are shown for the single-constraint (m–p) and general-constraint experiments (q–t).

Due to the lack of a comprehensive model of continuum uncertainty, I choose two different idealized approaches to represent continuum uncertainty. These two approaches showcase two important aspects of this uncertainty, both of which contribute to real-world continuum uncertainty.

In the *single-constraint* approach, I study the effect of changes in the column-integrated τ_{cont} with T_s. Thus, I assume that the constraint on τ_{cont} applies for a reference water vapor concentration of $x_0 = 0.02$. Due to the quadratic and linear dependencies on x of self and foreign continuum, respectively, the increasing τ_{foreign} dominates at $x < x_0$ and the decreasing τ_{self} dominates at $x > x_0$. Consequently, λ_v becomes slightly more destabilizing at $T_s \lesssim 290\,\mathrm{K}$ and substantially more stabilizing at $T_s \gtrsim 290\,\mathrm{K}$. Overall, the effect on λ is modest at 288 K, but reaches up to 7 % above 300 K (Figure 5.1n).

In the *general-constraint* approach, I study the effect of changes in the vertical distribution of $\tau_{\mathrm{cont}}(p)$ with pressure p. For this, I assume that the constraint on τ_{cont} applies for all atmospheric columns in my simulations. Given the different dependencies of self and foreign continuum on x and T, this implies that for a given decrease in τ_{self} by 10 %, the necessary increase in τ_{foreign} strongly increases with x and thus with T_s in my simulations. At a given T_s, the self continuum's quadratic dependence on x means that its absorption is more concentrated in the lower troposphere than that of the linear foreign continuum. Hence, replacing τ_{self} with τ_{foreign} redistributes absorption from the lower to the middle troposphere which moves the emission level upwards, reducing $\mathcal{L}$. The efficiency of this redistribution increases with x, but at high T_s, it is inhibited by the self continuum's negative dependence on T. This results in a destabilizing effect on λ_v below $T_s \approx 315\,\mathrm{K}$, peaking at around 2 % for 305 K, and a stabilizing effect on λ_v at very high T_s (Figure 5.1r).

The two approaches disagree on the exact effect of continuum uncertainty on the T_s dependence of $\mathcal{S}$. Generally, both approaches yield small effects at 288 K but substantial reductions in $\mathcal{S}$ of up to 0.2 K at T_s above 300 K.

In summary, the research questions of this study can be answered as follows:

1. Variations in self and foreign continuum have opposite effects on the atmospheric feedback due to their different dependencies on x.

2. Continuum uncertainty affects λ by impacting both T_s dependence and vertical distribution of total continuum absorption.

3. The effect of continuum uncertainty on $\mathcal{S}$ is modest at 288 K, but substantial above 300 K.

6

SUMMARY, CONCLUSIONS, AND OUTLOOK

In the studies presented in this thesis, I study Earth's clear-sky longwave feedback λ. My main focus lies on the central role of water vapor in shaping λ which originates from its generally well-understood thermodynamic and spectroscopic properties. The overarching theme of my thesis is to investigate the impact of remaining uncertainties in these properties on λ. In the first and second study, I investigate the effect on λ of uncertainty in the thermodynamic properties of water vapor, specifically how relative humidity $\mathcal{R}$ changes in a warming atmosphere. In the third study, I investigate the effect on λ of uncertainty in the spectroscopic properties of water vapor, specifically water vapor continuum absorption. Throughout this thesis, I analyze the spectrally resolved λ_ν which allows for a more insightful analysis of the underlying feedback mechanisms than λ.

In my first study, I infer the global-mean λ_ν from satellite observations of short-term variability. Whereas the spectral integral is similar to previous findings, the spectral distribution of λ_ν exhibits some differences. Similar to previous model studies, the largest contribution to the observed λ_ν comes from the atmospheric window, but this contribution differs between the λ_ν derived from seasonal and interannual variability, respectively. I show that seasonal variations in near-surface air temperature T_s are more concentrated over the relatively dry continents and polar regions of the Northern hemisphere, which favors a stronger surface feedback and thus a more negative λ_ν. This adds another dimension to the discussion of the pattern effect, the fact that warming in different regions has different effects on λ, which has often focused on differences between Eastern Pacific and Western Pacific warming (e.g., Dong et al., 2019). However, this strong extratropical surface feedback is another way in which the warming pattern affects λ. This is particularly relevant given the fact that continents and polar regions have warmed particularly strongly over the past few decades (e.g., Byrne and O'Gorman, 2018; Previdi et al., 2021).

The most striking difference between models and observations can be found in the absorption bands of water vapor: The observed λ_ν is substantially stabilizing, whereas idealized models exhibit near-zero λ_ν. I demonstrate that the stabilizing λ_ν in observations results from details in both the distribution of water vapor and its change with warming.

First, most water vapor is concentrated in the tropics and only very little in the polar regions, where thus parts of the water vapor bands

become optically thin. Consequently, λ_v is substantially influenced by the strongly stabilizing surface feedback at low T_s, but only affected by the near-zero atmospheric feedback at higher T_s where the water vapor bands are optically thick. I demonstrate this using radiative transfer simulations based on single-column simulations of λ_v at different T_s in my first study, and further corroborate it using direct observations of λ_v at different T_s in my second study. Due to these spatial variations, the surface feedback in the water vapor bands is non-zero in the global mean, but this is by design not captured by single-column models. This represents a limitation of these idealized models which are a popular tool to study Earth's climate due to their simplicity compared to complex circulation models. My results suggest that for some applications, it is worth using several atmospheric columns to represent spatial variations in temperature and humidity while still benefitting from the conceptual simplicity of single-column models (e. g., Feldl and Merlis, 2023).

Second, changes in $\mathcal{R}$ with warming are usually neglected in idealized models. However, in the short-term variability analyzed here, $\mathcal{R}$ decreases with T_s according to reanalysis. This decrease is relatively small, within the expected range of future changes in $\mathcal{R}$, but it has a substantial effect on λ_v and also a non-negligible impact on λ. Therefore, future research should prioritize approaches that can lead to a better constraint on sign, magnitude, horizontal and vertical distribution of future changes in $\mathcal{R}$. For the vertical distribution in particular, λ_v represents a powerful tool to constrain $\mathcal{R}$ changes. Due to the fact that different parts of the water vapor bands are sensitive to different layers of the atmosphere, the observed λ_v contains the radiative fingerprints of $\mathcal{R}$ changes in those different layers. I demonstrate this close relationship in my second study in which I observe λ_v at different T_s which feature different dependencies of the $\mathcal{R}$ profile on T_s. The deviations of the observed λ_v in the water vapor bands from the simulated λ_v under constant $\mathcal{R}$ can be almost entirely explained by the changes of the $\mathcal{R}$ profile in reanalysis. This demonstrates the direct link between λ_v and changes in the $\mathcal{R}$ profile. Consequently, the observational constraints on λ_v provided in my first two studies can be used to evaluate climate models regarding their representation of both short-term and spatial variability in $\mathcal{R}$ which can improve their representation of future changes in $\mathcal{R}$ with warming.

Beyond the global-mean picture, the observed λ_v at different T_s in my second study provide insights into how regional changes in $\mathcal{R}$ might affect the geographic distribution of λ. This can be thought of as higher-order effects that modulate the fundamental distribution of destabilizing *furnaces* in the deep tropics and stabilizing *radiator fins* in the subtropics (Pierrehumbert, 1995; McKim et al., 2021). Moreover, I demonstrate that the observed λ_v at a wide range of T_s can be understood using simple models with only a few variables. This

further boosts confidence in estimates of the clear-sky longwave λ, Earth's most important climate feedback. Because this understanding extends to T_s much lower and higher than Earth's current global average, this study also provides the foundation for similar studies of the climates of Earth's past or even that of other, Earth-like planets.

In my third study, I study the effect of uncertainty in water vapor continuum absorption, using radiative transfer simulations based on a single-column model. I find that separately increasing the self and foreign continuum weakens the surface feedback for both components. However, the two components have opposite effects on the atmospheric feedback, with a stronger foreign continuum — somewhat counterintuitively — having a stabilizing effect on λ. I demonstrate that this opposite behavior is the result of the different dependencies of self and foreign continuum on water vapor volume mixing ratio x. Therefore, constraining the partitioning between self and foreign continuum is essential to assess the continuum's impact on Earth's climate. Consequently, further efforts in constraining this partitioning are needed, which should include both improved measurement techniques and efforts to understand the fundamental processes governing the continuum. Understanding these processes would go a long way towards the eventual goal of explicitly modeling the continuum from the first principles of quantum mechanics.

In the real world, the total continuum is much better constrained than its components and thus uncertainties in self and foreign continuum are expected to be negatively correlated which I represent in two different idealized approaches. These approaches highlight two important ways by which continuum uncertainty affects λ_ν, namely by affecting the T_s dependence and the vertical distribution of total continuum absorption, respectively. To quantitatively assess the importance of these and other processes requires a comprehensive model of continuum uncertainty which does not yet exist. Developing such a model would be an important first step towards a better representation of the water vapor continuum in models.

From the idealized approaches used in my study, it seems that the overall effect of continuum uncertainty on λ — and thus also on climate sensitivity $\mathcal{S}$ — is small at T_s around the current global average of $288\,\text{K}$, but substantial at $T_s \geqslant 300\,\text{K}$. These temperatures frequently occur in the tropics which means that, due to the non-linear dependence of continuum absorption on x, the actual global-mean effect is presumably larger than that estimated for $T_s = 288\,\text{K}$ and quite possibly non-negligible. Furthermore, $T_s \geqslant 300\,\text{K}$ were even more widespread during warmer climates in Earth's past, such as the Paleocene-Eocene (e.g., Caballero and Huber, 2013). Consequently, uncertainty in continuum absorption directly affects the relationship between $\mathcal{S}$ in today's climate and $\mathcal{S}$ inferred from paleoclimate records. This should be considered when using these paleoclimate records as

a proxy to estimate $\mathcal{S}$ for studies of contemporary climate change. A more quantitative assessment of the overall effect on λ and $\mathcal{S}$ would again require a comprehensive model of continuum uncertainty. Such an assessment could then also use a more realistic global climatology of x, for example based on a general circulation model.

Overall, the studies included in this thesis provide deep insights into the fundamental processes that shape λ, the strongest radiative feedback in Earth's climate system. In particular, I develop a mechanistic understanding of how uncertainties in the thermodynamic and spectroscopic properties of water vapor affect the spectrally resolved λ_v. This way, I highlight the importance of better understanding the physical mechanisms behind changes in $\mathcal{R}$ with warming and water vapor continuum absorption.

The understanding developed in this thesis builds on the combination of two fundamentally different approaches: strongly idealized single-column models and real-world satellite observations. Whereas idealized models have provided many novel insights into the underlying mechanism of λ_v in recent years (e.g., Koll and Cronin, 2018; Kluft et al., 2021; Jeevanjee et al., 2021a; Seeley and Jeevanjee, 2021), satellite observations provide a powerful test to those ideas. Overall, the general spectral shape of λ_v in models is corroborated by satellite observations. However, these observations also highlight areas in which simplifying assumptions can miss important effects, for example when neglecting horizontal inhomogeneities or changes in the profiles of $\mathcal{R}$ and atmospheric temperature with warming.

Going forward, the spectral analysis in this thesis could be extended to the shortwave feedback λ_{sw}, whose spectral dimension so far remains mostly unexplored. However, shortwave water vapor absorption also strongly varies spectrally, and both surface and cloud albedo feedbacks might behave differently for near-infrared and visible radiation, respectively. This way, the spectral dimension of λ_{sw} provides the opportunity to diagnose and constrain the different underlying feedback mechanisms.

Based on the solidified understanding of the clear-sky longwave λ_v, an obvious next step is to further investigate the role clouds play in modifying it. The spectral perspective can be a valuable tool in this regard, because clouds behave differently throughout the spectrum; those spectral effects depend on altitude and opacity of the clouds, but also on the clear-sky background they replace (e.g., Huang et al., 2010; Huang et al., 2019; Stevens and Kluft, 2023). Such a spectral analysis could for example directly compare the all-sky longwave λ_v from satellite observations to that of global storm-resolving models that feature comparable spatial resolutions (e.g., Mauritsen et al., 2022; Merlis et al., 2024). This combination of observations and models represents a promising approach to better constrain λ — and thus Earth's climate sensitivity.

Part II

APPENDIX

A

DIRECT OBSERVATION OF EARTH'S SPECTRAL LONG-WAVE FEEDBACK PARAMETER

The work in this appendix has been published as:

CONTRIBUTIONS   S. A. Bühler proposed the idea for this study. I conducted the analysis and drafted the manuscript. M. Brath helped with developing the methodology, V. O. John helped with acquiring and processing the satellite data and L. Kluft helped with setting up and interpreting the single-column simulations. All authors participated in outlining the study, discussing the results and revising the manuscript.

NOTE   Compared to the published version, the version in this appendix includes minor formatting changes.

DIRECT OBSERVATION OF EARTH'S SPECTRAL LONG-WAVE FEEDBACK PARAMETER

F. E. Roemer[1,2], S. A. Buehler[1], M. Brath[1], L. Kluft[3], and V. O. John[4]

[1]*Center for Earth System Research and Sustainability (CEN), Meteorological Institute, Universität Hamburg, Hamburg, Germany*
[2]*International Max Planck Research School on Earth System Modelling (IMPRS-ESM), Hamburg, Germany*
[3]*Max Planck Institute for Meteorology, Hamburg, Germany*
[4]*European Organisation for the Exploitation of Meteorological Satellites (EUMETSAT), Darmstadt, Germany*

ABSTRACT

The spectral long-wave feedback parameter represents how Earth's outgoing long-wave radiation adjusts to temperature changes and directly impacts Earth's climate sensitivity. Most research so far has focused on the spectral integral of the feedback parameter. Spectrally resolving the feedback parameter permits inferring information about the vertical distribution of long-wave feedbacks, thus gaining a better understanding of the underlying processes. However, investigations of the spectral long-wave feedback parameter have so far been limited mostly to model studies. Here we show that it is possible to directly observe the global mean all-sky spectral long-wave feedback parameter using satellite observations of seasonal and interannual variability. We find that spectral bands subject to strong water-vapour absorption exhibit a substantial stabilizing net feedback. We demonstrate that part of this stabilizing feedback is caused by the change of relative humidity with warming, the radiative fingerprints of which can be directly observed. Therefore, our findings emphasize the importance of better understanding processes affecting the present distribution and future trends in relative humidity. This observational constraint on the spectral long-wave feedback parameter can be used to evaluate the representation of long-wave feedbacks in global climate models and to better constrain Earth's climate sensitivity.

The long-wave feedback parameter λ indicates how Earth's outgoing long-wave radiation responds to changes in near-surface air temperature T_s and thus directly affects Earth's climate sensitivity. Despite extensive research on λ throughout the past decades, the bulk of that research has focused on its spectrally integrated value (Hansen et al., 1984; Gregory et al., 2004; Soden et al., 2008; Sherwood et al., 2020). However, radiative feedbacks — and thus λ — fundamentally possess a spectral dimension. Therefore, we use satellite observations to directly infer Earth's spectral long-wave feedback parameter

$$\lambda_\nu = -\frac{dL_\nu}{dT_s}, \qquad\qquad (A.1)$$

where L_ν is the spectral outgoing long-wave radiation. In this framework, stabilizing feedbacks are negative and amplifying feedbacks are positive.

Spectrally resolving λ_ν offers clear advantages compared with considering only the spectrally integrated λ. First, the absorption of long-wave radiation by different atmospheric species strongly varies with wavenumber ν, making it possible to directly attribute changes in L_ν to the responsible absorbing species. Second, the spectrally varying absorption strength also causes strong variations in the emission level, the vertical layer L_ν is most sensitive to. This makes it possible to infer information about the vertical distribution of long-wave feedbacks. By considering only the integrated λ, this information can be lost due to cancelling effects in different spectral bands (Slingo and Webb, 1997; Huang et al., 2014; Brindley and Bantges, 2016; Pan and Huang, 2018).

The use of spectrally resolved satellite observations to study λ_ν was already suggested by Madden and Ramanathan (1980). However, the lack of hyperspectral satellite instruments with a sufficiently long time series has so far largely prevented observational investigations of λ_ν. For this reason, approaches to calculate and analyse spectrally resolved long-wave feedbacks have been limited mostly to model studies (Leroy et al., 2008; Soden et al., 2008; Huang et al., 2010; Huang et al., 2014; Pan and Huang, 2018; Kluft et al., 2019, 2021; Jeevanjee et al., 2021a; Seeley and Jeevanjee, 2021; Koll et al., 2023). Recent observational studies have demonstrated the feasibility of using hyperspectral satellite observations to derive spectral cloud radiative kernels (Yue et al., 2016) and to infer anomalies in temperature and humidity using the spectral fingerprinting method (Wu et al., 2020). Furthermore, satellite observations have been used to calculate the spectrally resolved cloud feedback (Huang et al., 2019) and to infer both clear-sky and all-sky λ_ν over parts of the tropical ocean (Huang and Ramaswamy, 2008). However, no study we are aware of has used observations to derive the global mean all-sky λ_ν, which comprises

all long-wave feedbacks. To close this gap, we infer λ_ν from hyper-spectral satellite observations

One of the main challenges in deriving feedbacks from satellite observations is that the available observational time series are much shorter compared with those usually realized in model studies, making it difficult to infer λ — or even λ_ν — from long-term trends. Instead, previous studies have used short-term variability on seasonal and interannual timescales to infer λ from both models and observations (Zhou et al., 2015, 2016; Colman and Hanson, 2017; Dong et al., 2020; Dessler, 2013; Dessler and Forster, 2018; Andrews et al., 2015; Dessler, 2020). The reasoning behind this approach is that most radiative feedbacks already occur on timescales of hours to weeks (Sherwood et al., 2020).

However, feedbacks derived from short-term variability are generally not the same as those derived from long-term trends (Dessler, 2013; Andrews et al., 2015; Zhou et al., 2016; Dessler and Forster, 2018; Dessler, 2020; Dong et al., 2020). These differences arise because aspects other than the global mean T_s can impact L_ν. Most prominently, the spatial distribution of the change in sea surface temperature is relevant because it affects overall stability and cloudiness — the so-called pattern effect (Dong et al., 2020; Ceppi et al., 2017 and references therein). The largest impact of the pattern effect can be seen in the short-wave cloud feedback (Andrews et al., 2015; Zhou et al., 2015, 2016; Colman and Hanson, 2017; Dessler, 2020; Dong et al., 2020), whereas the long-wave λ behaves similarly on short and long timescales (Zhou et al., 2015; Colman and Hanson, 2017). However, this is not necessarily the case for the spectrally resolved λ_ν due to the potential for spectral cancellation. In fact, the long-wave cloud feedback exhibits different spectral distributions between short and long timescales (Huang et al., 2019), meaning that the long-term λ_ν might differ from the short-term λ_ν. Nevertheless, investigating how long-wave feedbacks operate on seasonal and interannual timescales—regardless of their exact relation to long-term feedbacks—gives valuable insights into the inner workings of our climate system and improves our understanding of the processes affecting long-wave feedbacks on both short and long timescales.

Therefore, we infer λ_ν from short-term variability in L_ν calculated from observations by the infrared atmospheric sounding interferometer (IASI), and T_s, taken from the European Centre for Medium-Range Weather Forecasts' Reanalysis v.5 (ERA5). We perform linear regressions over both the global mean annual cycles and global monthly deviations from the mean annual cycles of both quantities to get two different estimates of λ_ν. In the following, we will refer to them as seasonal and interannual variability, respectively. Following Turner et al. (2015), we use a prediction model based on L_ν simulations to extend our estimate of λ_ν to the far infrared (FIR), which is not cov-
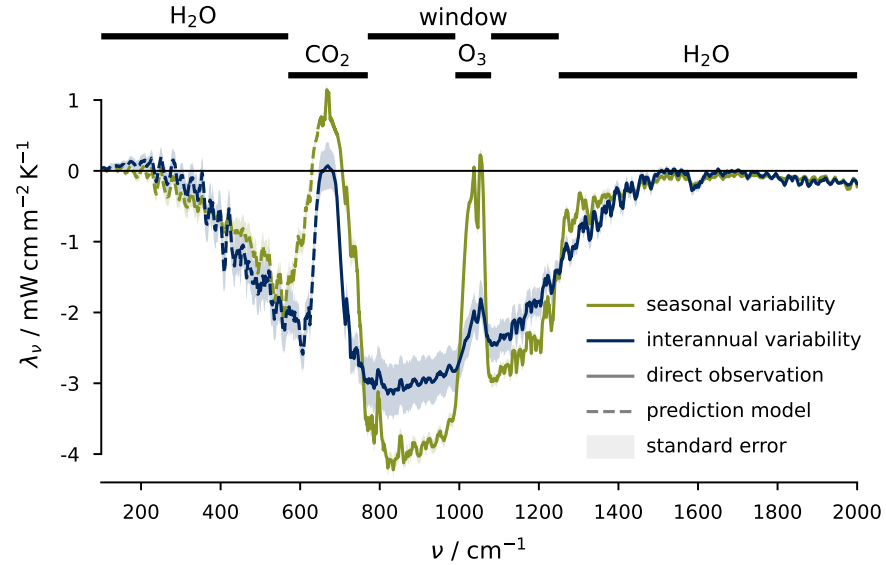
Figure A.1: All-sky spectral long-wave feedback parameter λ_ν ($10\,\mathrm{cm}^{-1}$ moving average) inferred from satellite observations by the IASI instrument. Shown are the λ_ν calculated from seasonal variability (green) and interannual variability (blue). The solid lines represent the part of the spectrum covered by IASI, the dashed lines show the λ_ν in the far-infrared, which are estimated using a prediction model developed by Turner et al. (2015) (Methods). Data are presented as mean values (lines) $\pm$ standard errors (shading). The ranges of different spectral bands are shown at the top. For better visibility, only the spectral range $100\text{–}2000\,\mathrm{cm}^{-1}$ is shown.

ered by IASI. This way, we provide an observational estimate of the global mean all-sky λ_ν, covering the full spectrum of Earth's outgoing long-wave radiation

A.2   SPECTRAL FEEDBACKS THROUGHOUT THE LONG-WAVE DOMAIN

First, we compare the observed all-sky spectral long-wave feedback parameters λ_ν with previous estimates of the all-sky long-wave feedback parameter λ by integrating spectrally. Our calculations based on seasonal and interannual variability both yield $\lambda \approx -2\,\mathrm{W\,m}^{-2}\,\mathrm{K}^{-1}$, in agreement with previous studies (Table A.1). The observed λ_ν from seasonal and interannual variability are shown in Figure A.1, their integrals over different spectral bands are listed in Table A.2. The sensitivity of the λ_ν to the selected period, orbital drift and calibration is discussed in Supplementary Discussion 3.

For comparison, we also show the seasonal and interannual λ_ν simulated on the basis of the Max Planck Institute high-resolution Earth system model version 1.2 (MPI-ESM1-2-HR) (Methods, Figure A.2

Table A.1: Long-wave feedback parameter λ as estimated by different studies.

study	data	approach	λ / $\mathrm{W\,m^{-2}\,K^{-1}}$
Sherwood et al. (2020)	–	review	-2.05 ± 0.18[a,b]
Soden et al. (2008)	coupled models	long-term trend	-2.05[a]
Huang et al. (2014)	coupled models	long-term trend	-1.98
Colman and Hanson (2017)	coupled models	long-term trend	-1.75 ± 0.40[b]
Jeevanjee (2018)	1D model	long-term trend	-2.0[a]
Kluft et al. (2019)	1D model	long-term trend	-2.33[a]
Budyko (1969)	observations	regional variability	-2.26[a]
Chung et al. (2010)	observations[c]	regional variability	-2.2[a]
Chung et al. (2010)	coupled models	regional variability	-2.1[a]
Koll and Cronin (2018)	observations	regional variability	-2.22[a]
Forster and Gregory (2006)	observations[c]	interannual variability	-3.7 ± 0.9
Murphy et al. (2009)	observations[c]	interannual variability	-2.78 ± 0.8
Murphy et al. (2009)	observations[d]	interannual variability	-1.64 ± 0.84
Chung et al. (2010)	observations[c]	interannual variability	-2.4[a]
Chung et al. (2010)	coupled models	interannual variability	-2.3[a]
Dessler (2013)	observations[d]	interannual variability	-1.45 ± 0.73[b]
Donohoe et al. (2014)	observations[d]	interannual variability	-2.0 ± 0.3
Trenberth et al. (2015)	observations[d]	interannual variability	-1.7 ± 0.3
Colman and Hanson (2017)	coupled models	interannual variability	-1.42 ± 0.82[b]
This study	observations	interannual variability	-2.03 ± 0.005
Tsushima et al. (2005)	observations[c]	seasonal variability	-2.05 ± 0.17
Forster and Gregory (2006)	observations[c]	seasonal variability	-2.7 ± 1.2
Chung et al. (2010)	observations[c]	seasonal variability	-2.3[a]
Chung et al. (2010)	coupled models	seasonal variability	-2.0[a]
Tsushima and Manabe (2013)	observations[c]	seasonal variability	-2.09[e]
Tsushima and Manabe (2013)	observations[d]	seasonal variability	-2.31[e]
This study	observations	seasonal variability	-1.96 ± 0.002

[a] only including clear-sky feedbacks

[b] We calculate the error of the total λ by adding the errors of the individual feedbacks in quadrature.

[c] Earth Radiation Budget Experiment (ERBE)

[d] Clouds and the Earth's Radiant Energy System (CERES)

[e] We calculate $\lambda = \lambda_0 \cdot (1 - g)$ from the gain factor g, which quantifies by how much the absolute value of λ is reduced compared to the reference Planck feedback $\lambda_0 = -3.21\,\mathrm{W\,m^{-2}\,K^{-1}}$ (Tsushima and Manabe, 2013).

Table A.2: Spectral long-wave feedback parameter λ_ν derived from observations by the IASI instrument of seasonal and interannual variability and integrated over different spectral bands. The λ_ν for wavenumbers $\nu < 645\,cm^{-1}$ are estimated using a prediction model (Turner et al., 2015) (Methods). All errors are $< 0.005\,W\,m^{-2}\,K^{-1}$.

spectral band	spectral range cm^{-1}	seasonal variability $W\,m^{-2}\,K^{-1}$	interannual variability $W\,m^{-2}\,K^{-1}$
FIR H_2O	100–570	−0.27	−0.28
CO_2	570–770	−0.11	−0.32
window	770–990, 1080–1250	−1.25	−0.99
O_3	990–1080	−0.12	−0.21
MIR H_2O	1250–2000	−0.16	−0.19
combined H_2O	100–570, 1250–2000	−0.42	−0.47
total	100–2760	−1.96	−2.03

and Table A.3). This simulated λ_ν includes only clear-sky feedbacks because the model's horizontal resolution of about 100 km is too coarse to reliably assess the radiative impact of clouds.

In both observation and model, the largest contribution to the integrated λ comes from the atmospheric window. However, the water-vapour absorption bands in the mid-infrared (MIR) and FIR also contribute substantially. Due to their different radiative properties, the processes controlling λ_ν differ between the water-vapour bands and the atmospheric window. In the following, we separately analyse the observed λ_ν in those two spectral regions.

A.3   STABILIZING FEEDBACK IN THE WATER-VAPOUR BANDS

The two water-vapour absorption bands in the MIR and FIR exhibit combined contributions to the total λ of $-0.42\,W\,m^{-2}\,K^{-1}$ and $-0.47\,W\,m^{-2}\,K^{-1}$ in the seasonal and interannual variability, respectively. Both all-sky λ_ν are in very good visual agreement with the findings of Huang et al. (2014), who calculated both clear-sky λ_ν (their Figure 2e) and all-sky λ_ν (their Figure 2f) on the basis of coupled climate models under forced warming. However, studies based on idealized models have found clear-sky λ_ν that are much closer to zero in the water-vapour bands (Koll and Cronin, 2018; Jeevanjee et al., 2021a).

At first, one might expect clouds to be responsible for this discrepancy. Conceptually, clouds can affect λ_ν in two different ways. First, changes in cloud fraction or cloud radiative properties can cause a
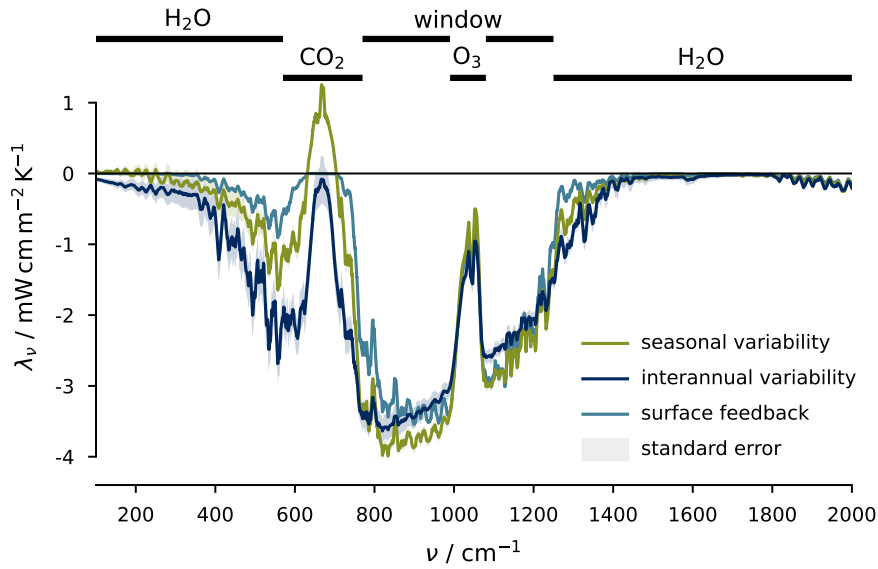
Figure A.2: Simulated clear-sky spectral long-wave feedback parameter λ_ν ($10\,\mathrm{cm}^{-1}$ moving average) based on the MPI-ESM1-2-HR model. Shown are the λ_ν calculated from seasonal variability (green) and interannual variability (blue), as well as the surface feedback $\lambda_{\nu,\mathrm{sfc}}$ (turquoise). Data are presented as mean values (lines) $\pm$ standard errors (shading). The ranges of different spectral bands are shown at the top. For better visibility, only the spectral range 100–2000 cm^{-1} is shown.

Table A.3: Simulated spectral long-wave feedback parameter λ_ν. The λ_ν are derived from seasonal and interannual variability calculated from simulations based on the MPI-ESM1-2-HR model. The surface feedback is an estimate based on those simulations, calculated using Equation (A.10) (Methods). All λ_ν are integrated over different spectral bands. All errors are $< 0.004\,\mathrm{W\,m^{-2}\,K^{-1}}$.

spectral band	spectral range cm^{-1}	seasonal variability $\mathrm{W\,m^{-2}\,K^{-1}}$	interannual variability $\mathrm{W\,m^{-2}\,K^{-1}}$	surface feedback $\mathrm{W\,m^{-2}\,K^{-1}}$
FIR H_2O	100–570	−0.14	−0.32	−0.07
CO_2	570–770	−0.11	−0.32	−0.07
window	770–990, 1080–1250	−1.21	−1.11	−1.09
O_3	990–1080	−0.16	−0.17	−0.16
MIR H_2O	1250–2000	−0.11	−0.15	−0.06
combined H_2O	100–570, 1250–2000	−0.25	−0.47	−0.13
total	100–2760	−1.78	−2.12	−1.49

cloud feedback, the net effect of which is thought to be slightly positive in the water-vapour bands (Huang et al., 2010; Huang et al., 2019). Second, even in the absence of cloud feedbacks, clouds impact the all-sky feedback by masking part of the clear-sky feedback due to the fixed anvil temperature mechanism (Hartmann and Larson, 2002). Both of these mechanisms indicate that clouds presumably act to dampen any negative clear-sky λ_ν. Furthermore, the negative all-sky λ_ν observed in the water-vapour bands is reproduced largely by the simulations of the clear-sky λ_ν mentioned in the preceding (Figure A.2), consistent with the findings of Huang et al. (2014). We therefore conclude that clouds are unlikely to explain the negative λ_ν observed in the water-vapour bands.

Rather, we will demonstrate in the following that the close-to-zero clear-sky λ_ν in the water-vapour bands found by idealized studies (Koll and Cronin, 2018; Jeevanjee et al., 2021a) result partly from two assumptions impacting the clear-sky physics. These assumptions pertain to the atmospheric feedback and the surface feedback, which comprise the radiative effects of atmospheric processes and surface warming, respectively (Koll and Cronin, 2018).

First, for the atmospheric feedback, we consider a framework first postulated by Simpson (1928a,b). This framework, discussed in more depth in other studies (Ingram, 2010; Jeevanjee et al., 2021a), states that for parts of the spectrum dominated by water-vapour absorption, constant relative humidity $\mathcal{R}$ means that the specific humidity — and thus the optical depth τ — depends only on temperature. This has implications for the emission level p_{em}, the layer the spectral outgoing long-wave radiation L_ν is most sensitive to, located where $\tau \approx 1$. If τ depends only on temperature, p_{em} is always located at the same temperature, causing constant L_ν. Applied to the feedback framework, this implies a λ_ν of close to zero. In the real world, the assumption that τ depends only on specific humidity is violated because of pressure broadening. This induces a negative feedback that is discussed in more depth in other studies (Ingram, 2010; Feng et al., 2023a; Koll et al., 2023) and accounted for in the idealized studies mentioned in the preceding (Koll and Cronin, 2018; Jeevanjee et al., 2021a).

Another assumption underlying Simpson's framework is that $\mathcal{R}$ does not change with T_s, an assumption also made by idealized studies investigating λ_ν (Koll and Cronin, 2018; Kluft et al., 2019, 2021; Jeevanjee et al., 2021a; Seeley and Jeevanjee, 2021). To first order, this is a reasonable assumption: changes in $\mathcal{R}$ with T_s are generally thought to lie within $\pm 1\,\%\,K^{-1}$ and this is believed to cause only a weak feedback (Sherwood et al., 2010; Held and Shell, 2012; Jeevanjee, 2018; Zelinka et al., 2020). To investigate how $\mathcal{R}$ varies with T_s in the analysed period, we calculate seasonal and interannual variability in $\mathcal{R}$ from the ERA5 reanalysis. In both cases, the global monthly $\mathcal{R}$ decreases with T_s between $300\,hPa$ and $700\,hPa$ (Figure A.3b), the
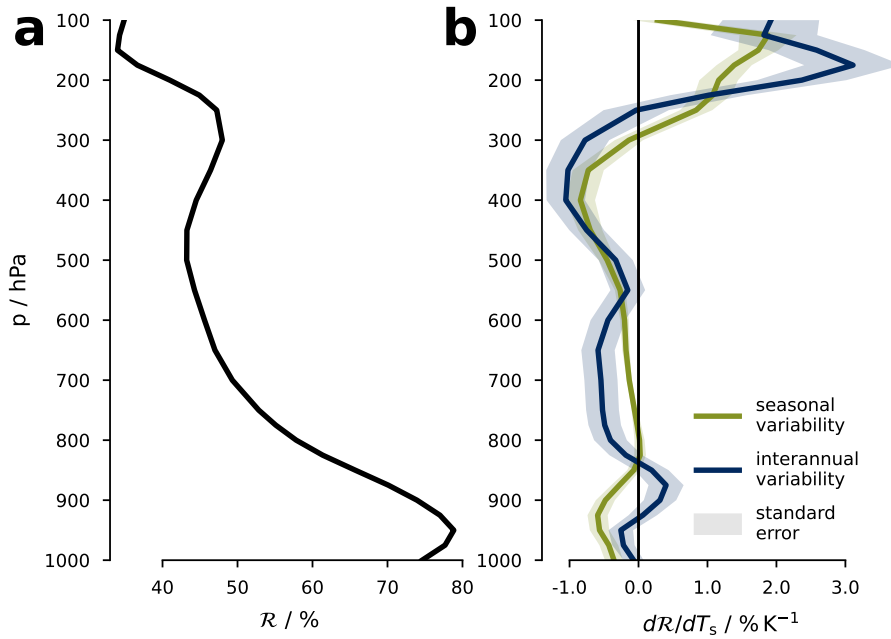
Figure A.3: Global mean profile of relative humidity $\mathcal{R}$ and its variability in ERA5 (07/2007–03/2020). (a) Global mean $\mathcal{R}$ profile (black). (b) Change of global mean $\mathcal{R}$ with near-surface air temperature T_s due to seasonal variability (green) and interannual variability (blue). Data are presented as mean values (lines) $\pm$ standard errors (shading).

layer where p_{em} in the water-vapour bands is mostly located (Figure A.4). The change in $\mathcal{R}$ within that layer amounts to on average $-0.4 \pm 0.05 \,\% \,\mathrm{K}^{-1}$ in the seasonal variability and $-0.6 \pm 0.09 \,\% \,\mathrm{K}^{-1}$ in the interannual variability — in contrast to the $\mathcal{R}$ increase in the multi-decadal trend found by Bourdin et al. (2021).

To quantify the impact of these $\mathcal{R}$ changes, we simulate λ_{ν} on the basis of the one-dimensional radiative-convective equilibrium model konrad (Kluft et al., 2022) (Figure A.5). We distinguish among three different scenarios: constant $\mathcal{R}$ with warming (black), decreasing $\mathcal{R}$ with T_s by $-0.5 \,\% \,\mathrm{K}^{-1}$ (brown), and increasing $\mathcal{R}$ with T_s by $+0.5 \,\% \,\mathrm{K}^{-1}$ (green). Assuming a C-shaped $\mathcal{R}$ profile (dark shading), the feedback in the water-vapour bands is $-0.34 \,\mathrm{W} \,\mathrm{m}^{-2} \,\mathrm{K}^{-1}$ for constant $\mathcal{R}$ with warming compared with $-0.45 \,\mathrm{W} \,\mathrm{m}^{-2} \,\mathrm{K}^{-1}$ for decreasing $\mathcal{R}$ and $-0.23 \,\mathrm{W} \,\mathrm{m}^{-2} \,\mathrm{K}^{-1}$ for increasing $\mathcal{R}$ with warming. This corresponds to a variation of $\pm 30 \,\%$ in the water-vapour bands and of $\pm 10 \,\%$ in the spectrally integrated λ (Table A.4). The results are similar for a vertically uniform $\mathcal{R} = 75\%$, although the effect is slightly weaker (Figure A.5, light shading). This implies that, as long as $\mathcal{R}$ is a function of temperature only, the exact shape of the $\mathcal{R}$ profile only weakly affects λ_{ν} in the water-vapour bands, in agreement with existing studies (Simpson, 1928a,b; Ingram, 2010). Because we perform the simulations under clear-sky conditions and assume that $\mathcal{R}$ variations are ver-
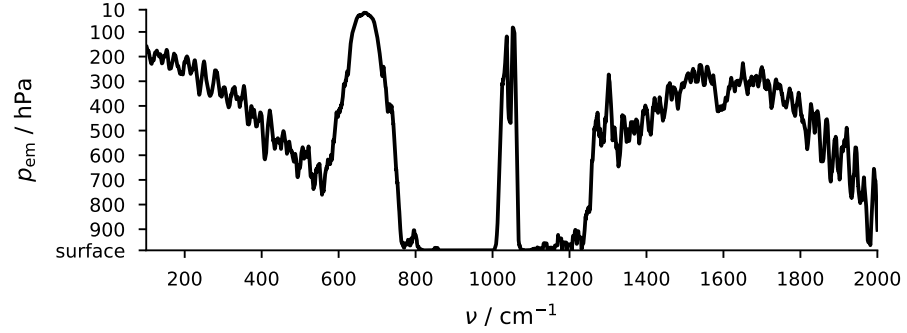
Figure A.4: Emission level p_{em} ($10 \, cm^{-1}$ moving average) of spectral outgoing long-wave radiation L_{ν}. The pressure level to which L_{ν} is most sensitive is calculated based on the MPI-ESM1-2-HR model (Methods). In the optically thin atmospheric windows, this emission level is located at the surface.

tically uniform, these numbers might be a slight overestimate. Nevertheless, these results show that even small changes in $\mathcal{R}$ with T_s represent a first-order effect for both the spectral λ_{ν} and the broadband λ.

Second, we calculate the surface feedback, the change in L_{ν} caused by surface warming alone, on the basis of the MPI-ESM1-2-HR model (turquoise line in Figure A.2, Table A.3, Methods). Integrated over both water-vapour bands, the surface feedback amounts to $-0.13 \, W \, m^{-2} \, K^{-1}$, while it is zero in Jeevanjee et al. (2021a) (their Figure 2f). However, their single-column set-up by design does not account for horizontal variations in temperature and thus absolute humidity. To demonstrate the effect of these variations, we simulate the surface feedback for different T_s using konrad (Figure A.6, Methods). For the simulations, we assume the same C-shaped $\mathcal{R}$ profile mentioned in the preceding for all T_s, and thus exponentially increasing integrated water vapour $\mathcal{W}$ (Methods). While the surface feedback in the water-vapour bands is zero for the moist atmospheres with T_s at or above the global mean (purple lines), it is strongly negative for the dry atmospheres at low T_s (blue lines). This causes the mean surface feedback to also be negative (black line) — analogous to the concept of "radiator fins" (Pierrehumbert, 1995; McKim et al., 2021).

As mentioned, the λ_{ν} values derived from IASI observations for the FIR are based on a prediction model introduced by Turner et al. (2015). Future missions such as the Far-infrared Outgoing Radiation Understanding and Monitoring (FORUM) and the Polar Radiant Energy in the Far Infrared Experiment (PREFIRE) will provide spectrally resolved observations of the entire FIR. These observations will also provide a test of the method presented here, shedding light on how well the λ_{ν} in the MIR water-vapour band is suited as a proxy for the λ_{ν} in the FIR. In contrast to the MIR, substantial parts of the FIR are sensitive to the layer above $300 \, hPa$, and the parts of the FIR

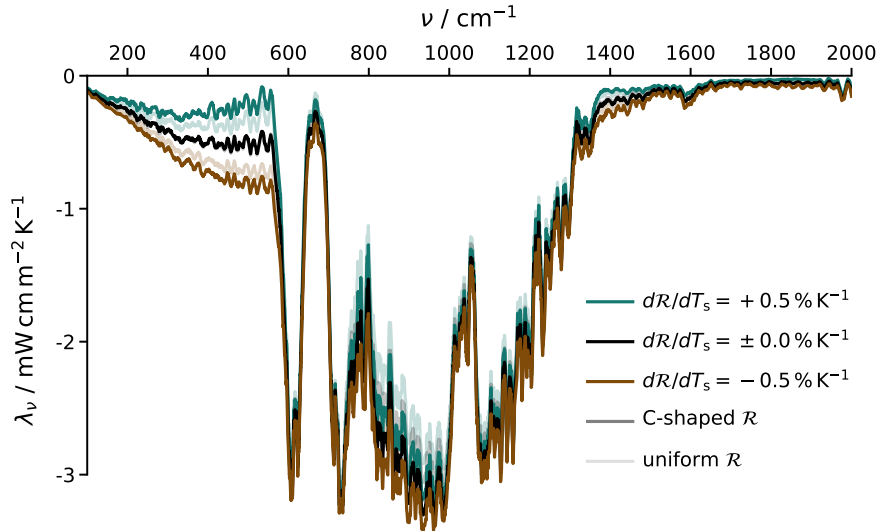Figure A.5: Simulated clear-sky spectral long-wave feedback parameter λ_ν ($10\,\mathrm{cm}^{-1}$ moving average) based on simulations using konrad (Kluft et al., 2022). Shown are the λ_ν for constant $\mathcal{R}$ with warming (black) and for changes of $\mathcal{R}$ with T_s of $-0.5\,\%\,\mathrm{K}^{-1}$ (brown) and $+0.5\,\%\,\mathrm{K}^{-1}$ (green). For all three cases, we separately show the λ_ν for the C-shaped global mean $\mathcal{R}$ profile shown in Figure A.3a (dark shading) and for a vertically uniform $\mathcal{R} = 75\%$ (light shading). For better visibility, only the spectral range 100–$2000\,\mathrm{cm}^{-1}$ is shown.

Table A.4: Spectral long-wave feedback parameter λ_ν derived from konrad simulations and integrated over different spectral bands. Shown are the results from four different experiments: "uniform" refers to a vertically uniform profile of relative humidity $\mathcal{R} = 75\%$, "C-shape" refers to a $\mathcal{R}$ profile as shown in Figure 3a. The term "constant" means that $\mathcal{R}$ did not change with increasing near-surface air temperature T_s, while "drying" refers to a change of $\mathrm{d}\mathcal{R}/\mathrm{d}T_s = -0.5\,\%\,\mathrm{K}^{-1}$.

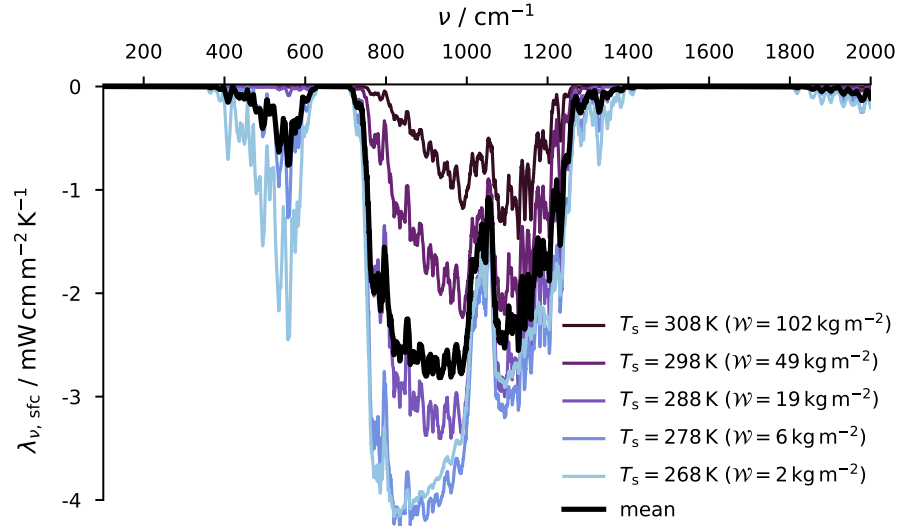| spectral band	spectral range	uniform constant	uniform drying	C-shape constant	C-shape drying
	cm^{-1}	$\mathrm{W\,m}^{-2}\,\mathrm{K}^{-1}$	$\mathrm{W\,m}^{-2}\,\mathrm{K}^{-1}$	$\mathrm{W\,m}^{-2}\,\mathrm{K}^{-1}$	$\mathrm{W\,m}^{-2}\,\mathrm{K}^{-1}$
FIR H_2O	100–570	−0.19	−0.24	−0.18	−0.27
CO_2	570–770	−0.34	−0.36	−0.36	−0.38
window	770–990, 1080–1250	−0.90	−0.96	−0.98	−1.04
O_3	990–1080	−0.19	−0.19	−0.20	−0.20
MIR H_2O	1250–2000	−0.14	−0.16	−0.15	−0.18
combined H_2O	100–570, 1250–2000	−0.33	−0.40	−0.33	−0.45
total	100–2760	−1.82	−1.96	−1.93	−2.13

Figure A.6: Simulated clear-sky spectral surface feedback $\lambda_{\nu,\mathrm{sfc}}$ based on simulations using konrad for different near-surface air temperatures T_s (coloured lines). The surface feedback averaged over all five different T_s is also shown (thick black line). For better visibility, only the spectral range 100–2000 cm^{-1} is shown.

that are sensitive to layers below 500 hPa do not exhibit absorption by methane.

A.4   SURFACE FEEDBACK VARIATIONS IN THE ATMOSPHERIC WINDOW

In the atmospheric window, our interannual λ_ν is in good visual agreement with modelling studies of both clear-sky and all-sky λ_ν, whereas our seasonal λ_ν is 0.26 W m^{-2} K^{-1} more negative (Figure 2f in Huang et al., 2014; Figure 7 (bottom) in Kluft et al., 2019; Figure 2f in Jeevanjee et al., 2021a). To explain this difference between seasonal and interannual variability, we first consider the surface feedback, which is the dominating factor impacting λ_ν in the window (turquoise line in Figure A.2, Table A.3). Conceptually, the strength of the surface feedback depends on two factors: (1) how much surface emission varies with near-surface air temperature T_s and (2) how much of that surface emission is absorbed by the atmosphere.

First, the variability of surface emission with T_s to first order depends on how much the skin temperature T_{skin}, the temperature of the ocean or land surface, varies with T_s. In ERA5, the global mean T_{skin} changes about 6 % more strongly with global mean T_s in the seasonal variability (1.03 ± 0.004 K K^{-1}) compared with the interannual variability (0.97 ± 0.012 K K^{-1}). Approximating the Planck curve as linear, this stronger variability in T_{skin} would explain a difference in λ_ν in the window of about 0.06 W m^{-2} K^{-1}.
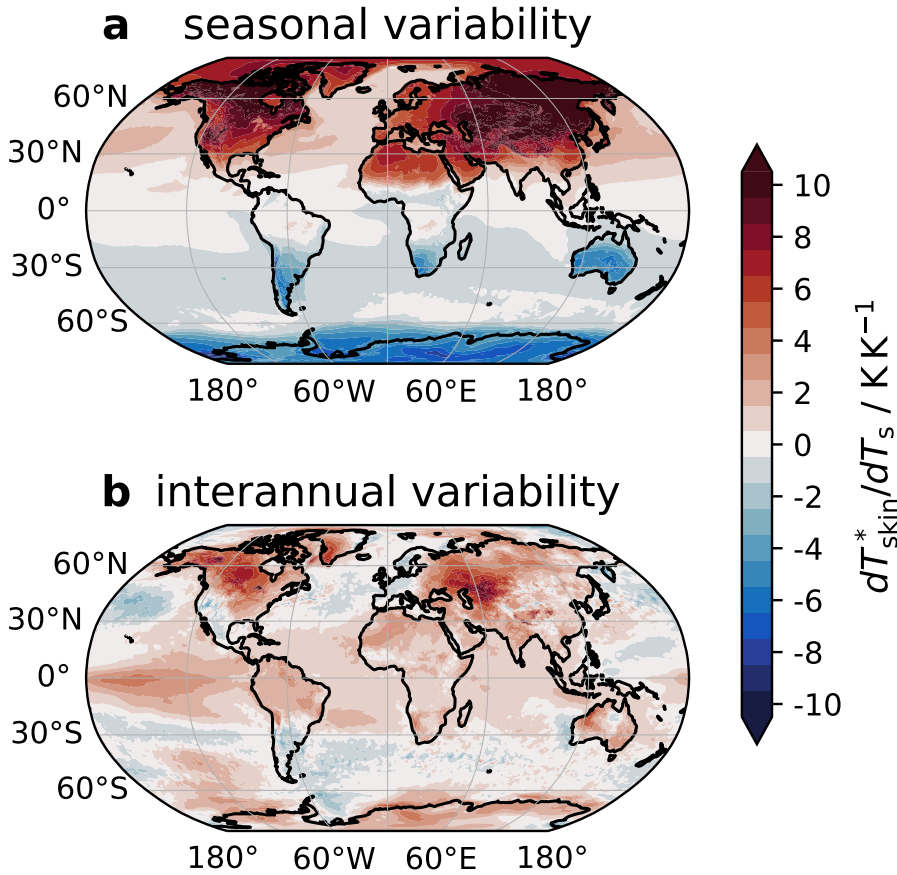
Figure A.7: Change in local skin temperature T^*_{skin} with global mean near-surface air-temperature T_s in ERA5 (07/2007–03/2020). Shown are the changes of T^*_{skin} in seasonal variability (a) and interannual variability (b)..

Second, the atmospheric absorption of surface emission in the window is caused mainly by water vapour. Therefore, the surface feedback in the window is stronger for dry atmospheres compared with moist atmospheres (Figure A.6). When we compare the spatial patterns of seasonal and interannual variability in the local skin temperature T^*_{skin} with global T_s, we find that the seasonal variability in T^*_{skin} originates mostly from the continents of the Northern Hemisphere, particularly at high latitudes, whereas the interannual variability is also substantial in the tropics (Figure A.7). Hence, the seasonal variability occurs under drier atmospheres on average, which causes a stronger surface feedback and thus a more negative seasonal λ_ν.

Apart from the clear-sky processes discussed in the preceding, clouds also play an important role in the atmospheric window. The simulated clear-sky λ_ν from seasonal and interannual variability differ by only about $0.1 \, W \, m^{-2} \, K^{-1}$ — much less than the observed all-sky λ_ν (Figure A.2, Table A.3). Furthermore, according to Huang et al. (2019), the cloud feedback in the window is about $0.1 \, W \, m^{-2} \, K^{-1}$ in the short term but about 25 % weaker in the long term. Therefore,

it seems plausible that the cloud feedback also differs between seasonal and interannual timescales, explaining some of the observed difference in λ_ν.

A.5   SPECTRAL OBSERVATIONS CAN CONSTRAIN CLIMATE SENSITIVITY

We infer the spectral long-wave feedback parameter λ_ν from satellite observations of seasonal and interannual variability. This way, we demonstrate that the spectral fingerprint of the net long-wave feedback can be directly observed using hyperspectral satellite instruments such as IASI. Furthermore, we use a prediction model to extend the spectra observed by IASI to the FIR. In the future, analogous models could be used to calculate λ_ν from other infrared sounders that have gaps in their spectral coverage, such as the atmospheric infrared sounder (AIRS) and the cross-track infrared sounder (CrIS).

When integrating λ_ν spectrally, we find a long-wave feedback parameter $\lambda \approx -2\,\mathrm{W\,m^{-2}\,K^{-1}}$, in agreement with the existing body of evidence. When spectrally integrating over the water-vapour absorption bands alone, we find a considerably negative feedback of almost $-0.5\,\mathrm{W\,m^{-2}\,K^{-1}}$. This negative λ_ν results partly from the change of relative humidity $\mathcal{R}$ with warming. Because direct observations of λ_ν contain the radiative fingerprint of this $\mathcal{R}$ change, they can provide a more realistic picture of λ_ν compared with idealized model studies.

Our findings emphasise the importance of better understanding processes affecting the present distribution and the future trends of $\mathcal{R}$. Despite recent progress in this field, due partly to the development of global storm-resolving models (GSRMs), substantial uncertainties remain (Lang et al., 2021). By providing an observational constraint on λ_ν, our results can be used to evaluate whether GSRMs correctly represent long-wave feedbacks — and thus by extension variability in $\mathcal{R}$ — on seasonal and interannual timescales. Due to the high spatial resolution of GSRMs, comparable to observations, this evaluation can also include the effect of clouds. This can put powerful constraints on the processes that also govern the long-term long-wave feedback and thus Earth's climate sensitivity.

A.6   METHODS

A.6.1   *Data*

IASI provides hyperspectral measurements of outgoing spectral radiances in 8461 channels in the thermal infrared (645–$2760\,\mathrm{cm^{-1}}$) with a spectral sampling of $0.25\,\mathrm{cm^{-1}}$ and a spectral resolution after apodisation of $0.5\,\mathrm{cm^{-1}}$. IASI scans across-track, with 30 different elementary fields of view (EFOV) symmetrically spanning $\pm 48.33°$ relative to

nadir. This corresponds to a maximum satellite zenith angle θ_{max} as seen from Earth of about $\pm 59°$. Each EFOV is sampled by a 2×2 array of circular instantaneous fields of view (IFOV). The highest horizontal resolution is reached directly below the satellite, with an IFOV diameter of 12 km. The swath width on ground is about 2200 km, causing the IFOV diameter to increase to 20×39 km at swath edge (Blumstein et al., 2004; August et al., 2012). We use the IASI level 1c (L1C) data from the meteorological operational satellite (Metop) A from 07/2007 to 12/2016 (EUMETSAT, 2018) and operational IASI L1C data from Metop A from 01/2017 to 03/2020.

For the full period (07/2007–03/2020), we use the Clouds and the Earth's Radiant Energy System CERES EBAF-TOA-Level 3b dataset for comparison (Loeb et al., 2018).

Atmospheric variables are taken from ERA5. This includes hourly fields of 2 m air temperature and skin temperature (Hersbach et al., 2019a) as well as hourly profiles of relative humidity (Hersbach et al., 2019b). We use ERA5's global mean monthly 2 m air temperature to calculate λ_ν, as it is a very robust variable constantly validated against observations (Hersbach et al., 2020). Hence we are confident that any errors in T_s have a negligible effect on our estimates of λ_ν. Furthermore, ERA5's temperature and humidity profiles, as well as its skin temperature are used for the analysis of the underlying feedback processes.

To simulate the model-based clear-sky λ_ν, we use model output of the MPI-ESM1-2-HR Earth system model (Müller et al., 2018) prepared for the "historical" experiment of the sixth phase of the Coupled Model Intercomparison Project (CMIP6) (Eyring et al., 2016). For the simulated years 2000–2014, the used data include daily profiles of atmospheric temperature and specific humidity on 95 vertical levels, near-surface values of air temperature, specific humidity, air pressure and horizontal wind components, as well as skin temperature, surface type, surface elevation and sea ice concentration (Jungclaus et al., 2019).

A.6.2   *Spectral outgoing long-wave radiation from observations*

The spectral long-wave feedback parameter λ_ν is defined in Equation (A.1) in terms of spectral outgoing long-wave radiation L_ν, a spectral flux. However, IASI measures outgoing spectral radiances $I_\nu(\theta)$ for different satellite zenith angles θ as seen from Earth. Hence, the $I_\nu(\theta)$ need to be integrated over all θ to yield the desired L_ν. However, some intermediary steps are necessary before we proceed to this angular integration.

First, we account for the fact that high latitudes are oversampled by IASI due to Metop's polar-orbiting track. We sort all observed $I_\nu(\theta, l)$ into $1°$ latitude bins l centred at latitude l_c, whose area is proportional

to $\cos(l_c)$. Relating this area to the actual number of observed $I_v(\theta, l)$ within that bin, $N(l)$, yields the correction factor

$$\alpha(l) = \frac{\cos(l_c)}{N(l)}, \tag{A.2}$$

which we estimate by averaging over 40 orbits.

Second, we use $\alpha(l)$ as weights to average over all $M(\theta)$ spectra in each orbit b that are observed under the same θ. Thereby, we assume azimuthal symmetry to aggregate the left and right side of the swath. This yields the spectral radiance averaged over orbit b for 15 different zenith angles θ as

$$\bar{I}_{v,b}(\theta) = \frac{1}{A_b} \sum_{i=1}^{M(\theta)} I_{v,i}(\theta, l) \, \alpha_i(l), \tag{A.3a}$$

$$A_b = \sum_{i=1}^{M(\theta)} \alpha_i(l), \tag{A.3b}$$

$$\theta \in [0°, \theta_{max}], \tag{A.3c}$$

where $\theta_{max} \approx 59°$ is the maximum θ under which spectra are observed by IASI.

Third, we need to account for the fact there are no IASI observations of $I_v(\theta)$ for $\theta > \theta_{max}$. Hence, we perform a linear interpolation between θ_{max} and $90°$ of $\bar{I}_{v,b}(\theta) \cos(\theta)$, which is zero for $\theta = 90°$, to calculate $\bar{I}_{v,b}(\theta)$ for those angles as

$$\bar{I}_{v,b}(\theta) \cos(\theta) = \bar{I}_{v,b}(\theta_{max}) \cos(\theta_{max}) + \frac{\theta - \theta_{max}}{90° - \theta_{max}} \tag{A.4a}$$

$$\left(\overbrace{\bar{I}_{v,b}(90°) \cos(90°)}^{\equiv 0} - \bar{I}_{v,b}(\theta_{max}) \cos(\theta_{max}) \right), \tag{A.4b}$$

$$= \bar{I}_{v,b}(\theta_{max}) \cos(\theta_{max}) \left(1 - \frac{\theta - \theta_{max}}{90° - \theta_{max}} \right), \tag{A.4c}$$

$$\theta \in \,]\theta_{max}, \, 90°]. \tag{A.4d}$$

For each orbit separately, we calculate the mean $L_{v,b}$ by conducting an angular integration over the $\bar{I}_{v,b}(\theta)$ calculated in Equations (A.3) and (A.4), respectively. Assuming azimuthal symmetry, this yields

$$L_{v,b} = 2\pi \int_{\theta=0°}^{90°} \bar{I}_{v,b}(\theta) \cos(\theta) \sin(\theta) \, d\theta. \tag{A.5}$$

Finally, we calculate the monthly mean L_v by averaging over all orbits in the respective month as

$$L_v = \frac{\sum_b L_{v,b} A_b}{\sum_b A_b}. \tag{A.6}$$

The spectral integral of this monthly mean L_v is compared with CERES observations in the Supplementary Discussion 2 and Supplementary Figure 2.

A.6.3   *Spectral outgoing long-wave radiation from model*

We use the Radiative Transfer for TOVs (RTTOV) model version 12.2 (Saunders et al., 2018) to simulate outgoing spectral radiances I_v in all 8461 IASI channels between $645\,\text{cm}^{-1}$ and $2760\,\text{cm}^{-1}$ with a spectral sampling of $0.25\,\text{cm}^{-1}$. In addition, we simulate I_v in 1817 channels of the planned Far-infrared Outgoing Radiation Understanding and Monitoring mission (Palchetti et al., 2020) between $100\,\text{cm}^{-1}$ and $645\,\text{cm}^{-1}$ with a spectral sampling of $0.3\,\text{cm}^{-1}$.

As input for the radiative transfer simulations, we use the MPI-ESM1-2-HR model output described in the preceding. The profiles of temperature and humidity, which represent the mean over the respective vertical layer, are interpolated in log pressure to the layer bounds, as required by RTTOV. We perform clear-sky simulations only by setting the cloud liquid and cloud ice contents to zero. For ozone, we use RTTOV's internal climatology (Hocking et al., 2019). We conduct those radiative transfer simulations for 500 randomly selected profiles per day.

For every selected profile, we calculate outgoing radiances $I_v(\theta)$ in all 10 278 channels for two different satellite zenith angles $(\theta_1, \theta_2) = (37.9°, 77.8°)$. We then apply a two-angle Gauss-Legendre quadrature (Kythe and Puri, 2011) to approximate L_v as

$$L_v \approx 2\pi \sum_{i=1}^{2} I_v(\mu_i)\, \mu_i\, w_i, \qquad\qquad (\text{A.7})$$

where $\mu_i = \cos(\theta_i)$ and the weights $w_i = 0.5$. RTTOV only supports simulations for $\theta \leqslant 75°$, so we infer $I_v(\theta_2)$ by interpolating between $75°$ and $90°$, analogous to Equations (A.4). The L_v spectra are averaged monthly.

A.6.4   *Prediction model for far-infrared*

The spectral range covered by IASI does not include the FIR, which contributes substantially to the total outgoing long-wave radiation L. Hence, we extend our calculation of the observed all-sky L_v to the FIR. The different steps are described in the following.

The simulated monthly clear-sky L_v spectra are used to set up a prediction model, closely following Turner et al. (2015). For every channel between $100\,\text{cm}^{-1}$ and $645\,\text{cm}^{-1}$, we calculate the correlation coefficient of $\ln(L_v)$ with every IASI channel from $645\,\text{cm}^{-1}$ to $2760\,\text{cm}^{-1}$. Then, the IASI channel with the highest correlation

is selected as predictor channel for the respective channel between $100\,\mathrm{cm}^{-1}$ and $645\,\mathrm{cm}^{-1}$. The L_ν of these channels are then calculated analogous to Equation (1) in Turner et al. (2015) as

$$\ln(L_{\nu,\mathrm{FIR}}) = \alpha_0 + \alpha_1\,\ln(L_{\nu,\mathrm{predictor}}), \tag{A.8}$$

where $L_{\nu,\mathrm{predictor}}$ are the monthly mean IASI observations and α_0 and α_1 are the regression coefficients.

A.6.5 *Calculation of spectral long-wave feedback parameter*

We use both the simulated clear-sky L_ν spectra and the extended observational all-sky L_ν spectra to calculate λ_ν from both seasonal and interannual variability, respectively. To this end, we perform linear ordinary least-squares regressions of monthly means, with L_ν as dependent variable and T_s as independent variable, and subtract the means over the whole time period, yielding monthly anomalies of L_ν and T_s.

To calculate λ_ν from seasonal variability, we then calculate the mean annual cycles of those monthly anomalies in both L_ν and T_s (Supplementary Figure 1b). We then regress the mean annual cycle in L_ν against the mean annual cycle of T_s. The slope of the regression delivers an estimate of λ_ν from seasonal variability (Supplementary Figure 1c).

To calculate λ_ν from interannual variability, we subtract these mean annual cycles of L_ν and T_s from the respective time series of monthly anomalies, yielding the deviations from the mean annual cycles for every single month. Assuming that the radiative forcing changes linearly over the analysed period, we calculate the linear trend in those deviations using an ordinary least-squares regression and then subtract that trend from the time series as well, following Dessler and Forster (2018). The detrended deviations from the mean annual cycle in L_ν (Supplementary Figure 1d), are then regressed against the deviations in T_s to infer λ_ν from interannual variability (Supplementary Figure 1e).

A.6.6 *Calculation of atmospheric variability*

We use the same methodology as for the feedback calculation described above to calculate seasonal and interannual variability with T_s for the global mean profile of relative humidity $\mathcal{R}$, as well as for both the global mean and spatially resolved skin temperature T_{skin}. All calculations are performed for monthly mean values.
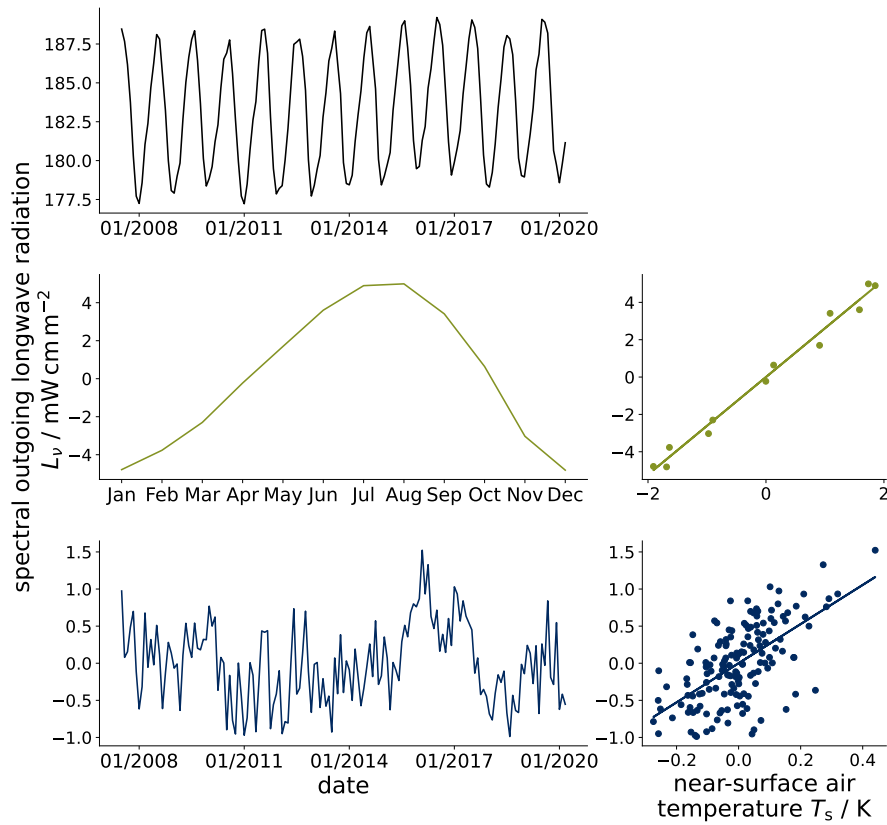
Figure A.8: Visualisation of λ_ν calculation. (a) Time series of monthly mean $L_\nu(\nu_1 = 1000.0\,\mathrm{cm}^{-1})$. (b) Mean seasonal cycle of $L_\nu(\nu_1)$. (c) Linear regression of mean seasonal cycles of $L_\nu(\nu_1)$ and T_s, yielding estimate of $\lambda_\nu(\nu_1)$ from seasonal variability. (d) Monthly deviations from mean seasonal cycle of $L_\nu(\nu_1)$. (e) Linear regression of monthly anomalies of $L_\nu(\nu_1)$ and T_s, yielding estimate of $\lambda_\nu(\nu_1)$ from interannual variability.

A.6.7 *Calculation of surface feedback*

We use the same radiative transfer simulations described in the preceding to calculate global mean values of an idealized surface feedback. In those simulations, we calculate $t_{v,\theta_i}(p, TOA)$, the transmittance of the simulated spectral radiances $I_v(\theta_i)$ from every input pressure level p to the top of the atmosphere (TOA), from which we then approximate $t_v(p, TOA)$, the transmittance with respect to L_v, as

$$t_v(p, TOA) \approx \sum_{i=1}^{2} t_{v,\theta_i}(p, TOA) \cos(\theta_i). \tag{A.9}$$

We use $t_v(sfc, TOA)$, the transmittance from the surface to TOA, to calculate an idealized estimate of the spectral long-wave surface feedback as

$$\lambda_{v,sfc} \approx t_v(sfc, TOA)\, \pi\, \frac{dB_v}{dT}\bigg|_{T=288\,K}. \tag{A.10}$$

Conceptually, the surface feedback represents the radiative signature of surface warming at TOA. This signature consists of (1) the additional radiation emitted by the surface per 1 K of warming, estimated by the derivative of the Planck function B_v with temperature T at the global mean T_s of 288 K, multiplied by π to convert to a spectral flux, and (2) the fraction of this additional surface emission that reaches TOA, estimated by $t_v(sfc, TOA)$, the global mean transmittance of the whole atmospheric column for each spectral channel. The T_s dependence of $\lambda_{v,sfc}$ is derived from the single-column simulations discussed in the following.

A.6.8 *Calculation of emission level*

From the $t_v(sfc, TOA)$, we calculate the optical depth with respect to L_v as

$$\tau_v(p, TOA) = -\ln(t_v(p, TOA)), \tag{A.11}$$

from which we calculate the emission level with respect to L_v as

$$p_{em,v} = \max\left(p[\tau_v(p, TOA) \leqslant 1]\right). \tag{A.12}$$

A.6.9 *Idealized single-column simulations*

We use the single-column model konrad v.1.0.1 (Kluft et al., 2022), developed by Kluft et al. (2019) and Dacie et al. (2019), which provides an idealized representation of the clear-sky tropical atmosphere assuming radiative-convective equilibrium. We calculate L_v for a "cool" profile with $T_s = 288$ K and a "warm" profile with $T_s = 289$ K. We then

calculate λ_ν as the difference between the warm L_ν and the cool L_ν. The L_ν are calculated using the line-by-line radiative transfer model ARTS (Eriksson et al., 2011; Buehler et al., 2018) in the same spectral range used in the preceding (100–2760 cm^{-1}) with a spectral resolution of about 0.1 cm^{-1}.

To quantify the impact of changes in $\mathcal{R}$ with T_s on λ_ν, we perform six different experiments. In three of them, we use a C-shaped $\mathcal{R}$ distribution (Figure A.3a); in the other three experiments, we assume a vertically uniform $\mathcal{R} = 75\,\%$. To predict changes of $\mathcal{R}$ with surface warming, we use T as a vertical coordinate, following Romps (2014). For both mean $\mathcal{R}$ distributions we consider three different cases. In the first case, we keep $\mathcal{R}(T)$ constant with increasing T_s. In the second and third cases, we let $d\mathcal{R}(T)/dT_s = -0.5\,\%\,K^{-1}$ and $d\mathcal{R}(T)/dT_s = 0.5\,\%\,K^{-1}$ throughout the atmospheric column, respectively. For each of the six experiments, we calculate λ_ν as described in the preceding.

We also use konrad to investigate the temperature dependence of the surface feedback. To this end, we calculate L_ν for five different T_s between 268 K and 308 K in 10 K increments. For the calculations, we again use a C-shaped $\mathcal{R}$ distribution (Figure A.3a). In contrast to the preceding, we derive the surface feedback by increasing T_s by 1 K, but not adjusting the atmospheric profiles of temperature and humidity, which isolates the radiative effects of surface warming. For reference, we also calculate the integrated water vapour of those profiles as

$$\mathcal{W} = -\frac{1}{g} \int q(p)\,dp, \tag{A.13}$$

where q is the specific humidity and g is the gravitational acceleration.

A.7 SUPPLEMENTARY DISCUSSION

A.7.1 *Visualisation of calculation of spectral longwave feedback parameter*

We calculate λ_ν using two different approaches. In the first approach, we calculate the mean annual cycles of monthly anomalies (Supplementary Figure A.8b). We then regress this mean annual cycle in L_ν against that of T_s. The slope of a linear regression delivers an estimate of λ_ν from seasonal variability (Supplementary Figure A.8c). In the second approach, we subtract the mean annual cycles from the time series of monthly anomalies, yielding deviations from the mean annual cycles. Assuming that the radiative forcing changes linearly, we remove the linear trend from the time series. The detrended deviations from the mean annual cycle (Supplementary Figure A.8d) are then regressed linearly to infer λ_ν from interannual variability (Supplementary Figure A.8e).
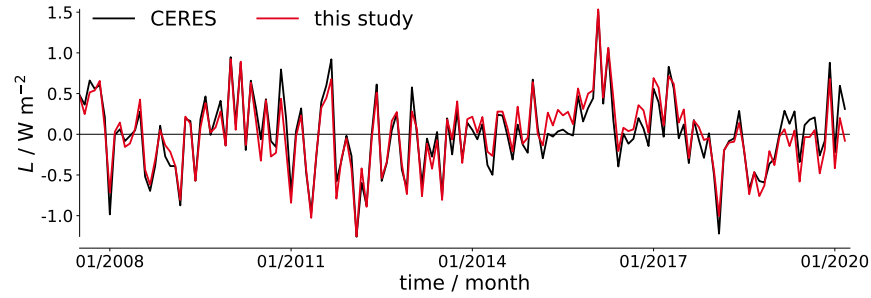
Figure A.9: Interannual variability in spectrally integrated outgoing long-wave radiation L from this study (red) and from CERES (black).

A.7.2 *Comparison to CERES observations*

When we integrate the L_ν calculated from the IASI observations spectrally, we can compare it to the broadband L provided by CERES. The two estimates of L agree very well, with a correlation coefficient of $r > 0.99$. On average, the L found here is $0.74\,\mathrm{W\,m^{-2}}$ (0.3%) lower than that of CERES, which can be attributed to contributions by spectral regions outside of the spectral coverage considered here (100–$2760\,\mathrm{cm^{-1}}$). Furthermore, we calculate the interannual variability of both time series as defined for the feedback calculation and compare the resulting time series for CERES and that derived using our method (Supplementary Figure A.9). The two time series are still very similar, with $r = 0.95$.

A.7.3 *Sensitivity to period, calibration and orbital drift*

To test the sensitivity of the λ_ν from the IASI observations to the length and starting year of the selected time period, we plot the deviations from the λ_ν calculated over the whole time period (07/2007–03/2020) for eight different alternative time periods (Supplementary Figure A.10): Three different 2-year periods, three different 5-year periods and two different 10-year periods. We find that for the seasonal λ_ν, already two years are sufficient to achieve a very similar result as for the full period. The interannual λ_ν depends much more on the selected time period, here about 5-10 years are needed for a good agreement with the full period, with the largest deviations occurring in the CO_2 absorption band.

Regarding instrument calibration, the reprocessed IASI level 1c data (which we used from 07/2007 through 12/2016) and operational IASI level 1c data (which we used from 01/2017 through 03/2020), differ by $\leqslant 0.1\,\mathrm{K}$ (Bouillon et al., 2020), which shows a very stable calibration that does not substantially affect our results. Regarding orbital drift, Metop-A only started drifting in autumn 2017. Performing
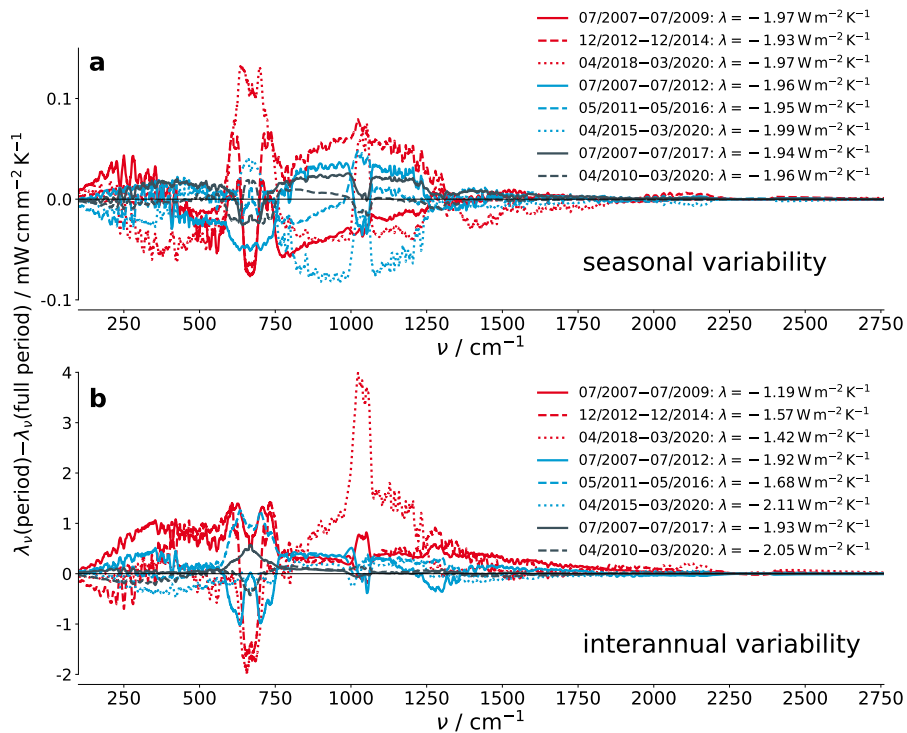
Figure A.10: Dependency of λ_ν on selected time period. Shown is the deviation from the λ_ν derived from the full period (07/2007–03/2020) of three different 2-year periods, three different 5-year periods and two different 10-year periods. (Top) seasonal variability. (Bottom) Interannual variability.

the analysis only for the period 07/2007–07/2017 yields very similar results, with the only non-negligible difference occurring in the CO_2 absorption band (Supplementary Figure A.10).

COMPETING INTERESTS

The authors declare no competing interests.

DATA AVAILABILITY

The processed data used to derive the main results of this study are available at `https://doi.org/10.26050/WDCC/FluxFeedb_ObsSim_v2` (Roemer et al., 2023b). This includes global monthly averages of the spectrally resolved outgoing long-wave radiation derived from IASI observations and calculated on the basis of both the MPI-ESM1-2-HR and konrad models. Furthermore, IASI Level 1C Climate Data Record Release 1 - Metop-A (`10.15770/EUM_SEC_CLM_0014`) can be ordered through the EUMETSAT User Helpdesk (`https://www.eumetsat.int/contact-us`). The operational IASI L1c data can be directly downloaded from the EUMETSAT Data Store (`https://data.eumetsat.int/data/map/EO:EUM:DAT:METOP:IASIL1C-ALL#`). The ERA5 reanalysis data can be downloaded from the Copernicus Climate Change Service (C3S) Climate Data Store for the data on pressure levels (`https://doi.org/10.24381/cds.bd0915c6`) and single levels (`https://doi.org/10.24381/cds.adbb2d47`). The MPI-ESM1-2-HR model output prepared for CMIP6 can be downloaded from `https://esgf-data.dkrz.de/search/cmip6-dkrz`. The CERES EBAF Ed4.0 dataset can be downloaded from `https://ceres.larc.nasa.gov/data`.

CODE AVAILABILITY

The computer code used to produce the central results of this study is available upon request from the corresponding author.

B

OBSERVATIONS OF THE CLEAR-SKY SPECTRAL LONGWAVE FEEDBACK AT SURFACE TEMPERATURES BETWEEN 210 K AND 310 K

The work in this appendix is under review at *Journal of Climate* and available as a preprint at:

CONTRIBUTIONS   Both I and S. A. Bühler conceived and outlined the study. I conducted the analysis and drafted the manuscript. Both I and S. A. Bühler participated in discussing the results and revising the manuscript.

NOTE   Compared to the preprint version, the version in this appendix includes minor formatting changes.

OBSERVATIONS OF THE CLEAR-SKY SPECTRAL LONGWAVE FEEDBACK AT SURFACE TEMPERATURES BETWEEN 210 K AND 310 K

F. E. Roemer[1,2] and S. A. Buehler[1]

[1]*Center for Earth System Research and Sustainability (CEN), Meteorological Institute, Universität Hamburg, Hamburg, Germany*
[2]*International Max Planck Research School on Earth System Modelling (IMPRS-ESM), Hamburg, Germany*

ABSTRACT

The longwave feedback λ characterizes how Earth's outgoing longwave radiation changes with surface temperature T_s, directly impacting climate sensitivity. Compared to λ, its spectrally resolved counterpart λ_ν offers deeper insights into the underlying physical processes. Both λ and λ_ν vary with T_s, but this T_s dependence has so far only been investigated using models. Here, we derive the clear-sky λ_ν for T_s between 210 K and 310 K based on observations of the AIRS instrument. We disentangle the radiative signatures of the atmospheric general circulation by simulating λ_ν based on a single-column model with different degrees of idealization. We find that at low T_s, the observed λ_ν is dominated by the surface response and sensitive to biases in Earth's skin temperature. At higher T_s, changes in the vertical distributions of atmospheric temperature and relative humidity play an important role in shaping λ_ν. These changes impact both the absorption of surface emission in the atmospheric window and the atmospheric emission in the water vapor and CO_2 absorption bands. Our results demonstrate that we can fully understand the observed λ_ν at a wide range of T_s using a simple model of Earth's atmosphere, lending further support to estimates of the clear-sky longwave λ, Earth's most fundamental climate feedback. They also highlight the effect of different assumptions about Earth's atmosphere on λ. Similar approaches can be used to better constrain changes in relative humidity and temperature with warming using satellite observations, as well as for paleoclimate and exoplanet studies.

SIGNIFICANCE STATEMENT

The longwave feedback describes how much the thermal radiation Earth emits to space increases with warming. It is the strongest feedback in Earth's climate and determines the warming in response to an increase in CO_2 concentration. We use satellite observations to analyze the dependence of the longwave feedback on radiation frequency at a wide range of surface temperatures which allows insights into the underlying physical processes. We reproduce these observations using a simple model of Earth's atmosphere, demonstrating the complete physical understanding of this fundamental climate feedback. Our results can be used to constrain changes in atmospheric temperature and humidity with warming from satellite observations and to better understand the climates of Earth's past and of other planets.

B.1   INTRODUCTION

The longwave feedback λ quantifies the change in Earth's outgoing longwave radiation $\mathcal{L}$ with near-surface air temperature T_s. It is by far the strongest radiative feedback in Earth's climate system and thus substantially affects climate sensitivity, the temperature change caused by a doubling of atmospheric CO_2 concentration. Traditionally, the focus has been on the spectrally integrated λ (e.g., Sherwood et al., 2020, and references therein). In the past few years, however, there has been increased interest in λ_ν, which quantifies λ as a function of wavenumber ν (e.g., Huang et al., 2014; Pan and Huang, 2018; Koll and Cronin, 2018; Kluft et al., 2019, 2021; Jeevanjee et al., 2021a; Seeley and Jeevanjee, 2021; Feng et al., 2023a; Koll et al., 2023; Stevens and Kluft, 2023). Given that electromagnetic radiation — and in particular its interaction with greenhouse gases — is inherently spectral in nature, this spectral perspective allows for deeper insights into the underlying physical processes governing λ.

Most of the studies on λ_ν have been based on models, but spectral satellite observations have been used to investigate trends in the spectral $\mathcal{L}_\nu$ (Raghuraman et al., 2023; Brindley and Bantges, 2016, and references therein), to study the super-greenhouse effect (Huang and Ramaswamy, 2008), to derive the spectral cloud feedback (Huang et al., 2019), and to infer the global-mean all-sky λ_ν (Roemer et al., 2023a). These studies demonstrate that spectral satellite observations of $\mathcal{L}_\nu$ are a powerful tool that allows us to test our understanding of the key processes governing λ.

A good way to test this understanding of λ is to investigate its dependence on T_s, because the relative importance of different processes governing λ depends on T_s. For example, recent studies have shown how the roles of the surface, H_2O, and CO_2 vary with T_s and thus directly affect the temperature dependence of the clear-sky λ_ν

(Koll and Cronin, 2018; Kluft et al., 2021; Seeley and Jeevanjee, 2021; Feng et al., 2023a; Koll et al., 2023). To our knowledge, all studies on this topic have solely relied on strongly idealized models, partly because they conveniently allow for controlled variations of different variables independently of each other. However, this means that these studies make quite strong assumptions about the behavior of Earth's atmosphere which directly affects λ_ν. So how well-suited are these simple models to reproduce the actual λ_ν at different T_s? To answer this question, we derive λ_ν from satellite observations for T_s ranging from 210 K to 310 K, exploiting Earth's large spatial variations in monthly mean T_s.

In contrast to model worlds, changes in $\mathcal{L}$ with T_s over Earth's surface — and thus also λ_ν derived from these variations — not only include the signature of the T_s dependence itself, but also the signature of variations in atmospheric temperature and humidity caused by the general circulation (e.g., Feng et al., 2023b). For example, column relative humidity $\mathcal{R}_c$, the ratio between actual and satured water vapor column, strongly varies with T_s over Earth's surface: $\mathcal{R}_c$ is high in the polar regions through the mid-latitudes but also in the areas of deep tropical ascent, while $\mathcal{R}_c$ is lower both in the cooler maritime subtropics and the warmer continental subtropics (Figure B.1). This means that the observed λ_ν at those different T_s will be impacted by differences in the circulation-induced average column relative humidity $\overline{\mathcal{R}_c}$ (McKim et al., 2021) and the average vertical distributions of relative humidity $\overline{\mathcal{R}}$ (Bourdin et al., 2021), as well as by changes of column relative humidity with near-surface air temperature $d\mathcal{R}_c$ (Roemer et al., 2023a) and the vertical distribution of these changes $d\mathcal{R}$ (Pan and Huang, 2018).

However, while those factors complicate isolating the pure T_s dependence of λ_ν, they provide a powerful test case to probe our understanding of the processes governing Earth's clear-sky longwave feedback and how they depend on ν and T_s. We therefore derive the clear-sky $\lambda_\nu(T_s)$ for bins of $\Delta T_s = 10$ K, ranging from 210 K to 310 K. We then assess the effect of circulation-induced variations in atmospheric temperature and humidity on the clear-sky λ_ν using a simple atmospheric model which represents temperature and humidity profiles with different degrees of idealization. This approach allows us to separate the spectral signature of the pure T_s dependence from that of circulation-induced atmospheric temperature and humidity variations. This way, we showcase both the validity and limitations of different assumptions about the behavior of Earth's atmosphere with warming and unpin the fundamental understanding of the observed λ_ν at a wide range of T_s. The solid understanding of this essential climate feedback provides the foundation to study climates of Earth's past and of other planets.
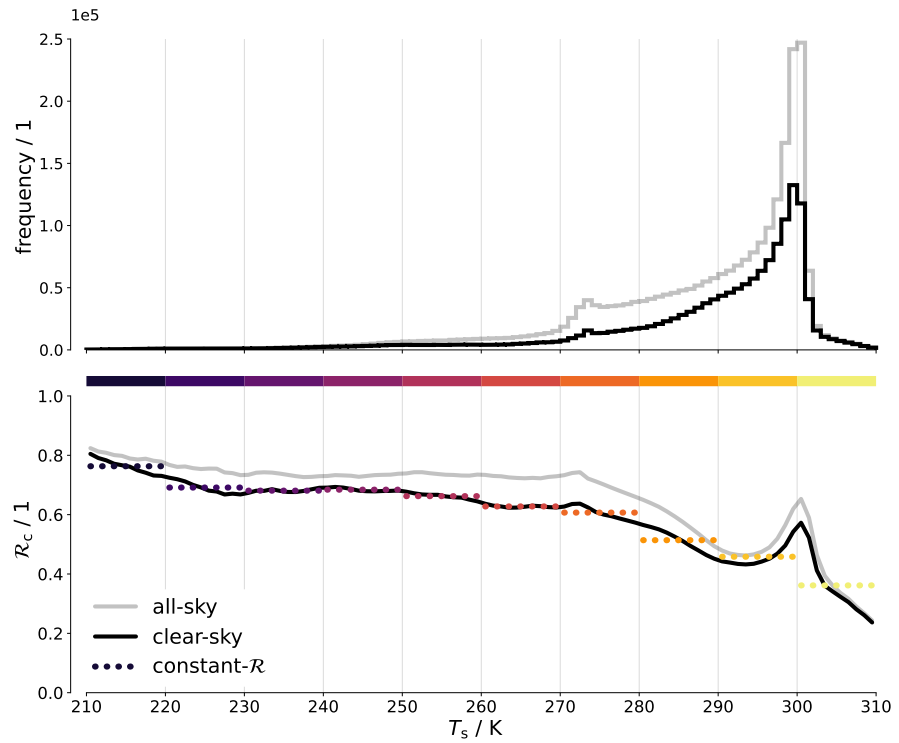
Figure B.1: Occurences of near-surface air temperatures T_s in ERA5 in 1 K bins (top) and average column relative humidity $\mathcal{R}_c$ in those bins (bottom). Shown are the values for all-sky conditions (gray) and those accounting for the clear-sky sampling of the used satellite data set (black). Furthermore, the $\mathcal{R}$ values used in the constant-$\mathcal{R}$ experiment are shown for each $\Delta T_s = 10$ K regime.

B.2   DATA

We use the *Aqua AIRS Level 3 Spectral Outgoing Longwave Radiation (OLR) Monthly* dataset (Huang, 2020), which provides the monthly-mean all-sky and clear-sky spectrally resolved outgoing longwave radiation $\mathcal{L}_\nu$ spanning the spectral range $10\,\text{cm}^{-1}$ to $2000\,\text{cm}^{-1}$ with a spectral resolution of $10\,\text{cm}^{-1}$. The spectra are available on a $2° \times 2°$ longitude-latitude grid from September 2002 through December 2022. The dataset is based on observations by the AIRS instrument (Aumann et al., 2003), which observes outgoing spectral radiances in 2378 spectral channels in three spectral bands: $649.6\,\text{cm}^{-1}$–$1136.6\,\text{cm}^{-1}$, $1217.0\,\text{cm}^{-1}$–$1613.9\,\text{cm}^{-1}$, and $2181.5\,\text{cm}^{-1}$–$2665.2\,\text{cm}^{-1}$ (Chen and Huang, 2016). To derive $\mathcal{L}_\nu$ outside of these spectral bands, a multiregression scheme based on principal component analysis is used, as described in detail in Huang et al. (2008).

As input for our atmospheric model, we take data from the ERA5 reanalysis (Hersbach et al., 2020). We use atmospheric profiles of temperature T, relative humidity $\mathcal{R}$, and cloud fraction f_c (Hersbach et al., 2019b). Furthermore, we use near-surface values of air temperature T_s and pressure p_s, as well as skin temperature T_{skin} over ocean (Hersbach et al., 2019a), whereas T_{skin} over land is taken from ERA5-Land (Muñoz-Sabater et al., 2021; Muñoz-Sabater, 2019).

B.3   METHODS

B.3.1   *Observations*

For our analysis we average together daytime and nighttime values, yielding one average spectrum per grid square and month. We use the clear-sky $\mathcal{L}_\nu$ spectra, which are only available for a subset of grid squares (57 % of spectra, corresponding to 59 % of the global surface area when averaged over the entire period).

To derive λ_ν from satellite observations, we sort the clear-sky $\mathcal{L}_\nu$ into bins of $\Delta T_s = 1\,\text{K}$ (centered at $210.5\,\text{K}$, $211.5\,\text{K}$, ..., $309.5\,\text{K}$) and calculate the bin-average $\overline{\mathcal{L}_\nu}$. The binning is performed to remove effects due to the strongly varying number of observed $\mathcal{L}_\nu$ at different T_s, which makes the results better comparable to those of idealized simulations described below. We calculate the spectral feedback λ_ν for ten different regimes of $\Delta T_s = 10\,\text{K}$ (centered at $215\,\text{K}$, $225\,\text{K}$, ..., $305\,\text{K}$) by linearly regressing $\overline{\mathcal{L}_\nu}$ against T_s within those regimes. We only consider T_s between $210\,\text{K}$ and $310\,\text{K}$, because of the very small relative sample size of T_s below $210\,\text{K}$ (0.03 %) and above $310\,\text{K}$ (0.13 %), respectively, which is not enough for a robust analysis.

B.3.2   *Simulations*

To test our understanding of the observed λ_ν, we simulate λ_ν for a simple atmospheric model that produces profiles of temperature T and relative humidity $\mathcal{R}$ for each T_s bin based on reanalysis data from ERA5 (see Section B.2). We use different versions of this model which use different assumptions about the atmosphere and thus represent different degrees of idealization. Those profiles are then plugged into a radiative transfer model (see Section B.3.2.4) to calculate $\mathcal{L}_\nu$. From those $\mathcal{L}_\nu$ spectra, λ_ν is calculated as described above for the observed λ_ν.

B.3.2.1   *Representation of clear-sky sampling*

Before we can use the reanalysis data as input for our simulations, we need to account for the fact that they represent all-sky values, whereas we use observations of the clear-sky $\mathcal{L}_\nu$ which are subject to clear-sky sampling biases (John and Soden, 2007). We account for this by adjusting the atmospheric data in two ways.

First, the observed clear-sky $\mathcal{L}_\nu$ are not available for every grid square in every month and thus we average all atmospheric quantities only over those grid squares and months where there are clear-sky $\mathcal{L}_\nu$ available. Second, the clear-sky $\mathcal{L}_\nu$ is only derived from the clear-sky part of the grid square which on average is drier than the cloudy-sky part of the grid square. We account for this by assuming that the all-sky $\mathcal{R}_{all}$ is a weighted average of the clear-sky $\mathcal{R}_{clear}(p)$ and cloudy-sky $\mathcal{R}_{cloudy} = 100\%$, with the weights being the clear-sky fraction $1 - f_{cloud}(p)$ and cloud fraction $f_{cloud}(p)$ at each pressure level p, respectively. We then use this to calculate $\mathcal{R}_{clear}(p)$ as

$$\mathcal{R}_{clear}(p) = \frac{\mathcal{R}_{all}(p) - \mathcal{R}_{cloudy} \cdot f_{cloud}(p)}{1 - f_{cloud}(p)}. \tag{B.1}$$

This $\mathcal{R}_{clear}$ is used for all calculations in the following, but is for simplicity simply referred to as $\mathcal{R}$.

B.3.2.2   *Column-integrated humidity variables*

Column relative humidity $\mathcal{R}_c$ is defined as

$$\mathcal{R}_c = \frac{\frac{1}{g} \int_{p_{cp}}^{p_s} q(p)\, dp}{\frac{1}{g} \int_{p_{cp}}^{p_s} q^*(p)\, dp}, \tag{B.2}$$

where g is the gravitational acceleration, p_s is the surface pressure, p_{cp} is the pressure at the cold-point tropopause, q is the specific humidity, and q^* is the saturation specific humidity.

Similarly, the partial column relative humidity $\mathcal{R}_c^\uparrow$, representing the column relative humidity above a given pressure level p, is defined as

$$\mathcal{R}_c^\uparrow(p) = \frac{\frac{1}{g}\int_{p_{cp}}^{p} q(p')\,dp'}{\frac{1}{g}\int_{p_{cp}}^{p} q^*(p')\,dp'}. \tag{B.3}$$

B.3.2.3 *Atmospheric model*

Our model is based on the single-column model konrad (Kluft et al., 2019; Dacie et al., 2019). We use it to create profiles of temperature T and water vapor volume mixing ratio q on 128 vertical levels for near-surface air temperature T_s in 1 K steps from 210.5 K to 309.5 K, for the different experiment setups described below. The atmospheric profiles of T and $\mathcal{R}$, as well as skin temperature T_{skin} and surface pressure p_s are based on the ERA5 reanalysis data (see Section B.2), the concentrations of the other greenhouse gases are given as vertically uniform concentrations of CO_2 = 410 ppm, CH_4 = 1866 ppb and N_2O = 332 ppb (Lee et al., 2023). We do not consider the effects of O_3 because defining realistic O_3 concentration profiles for the given range of T_s is beyond the scope of this work. We also focus on clear-sky conditions only. We perform the following experiments:

THE SURFACE-PLANCK EXPERIMENT   This most basic experiment differs from all the other experiments in that it does not have an atmosphere, but simply quantifies the change in surface emission due to changes in skin temperature T_{skin}. Furthermore, it does not use a radiative transfer model but rather calculates the feedback as

$$\lambda_{\nu,\text{surface−Planck}}(T_s) = -\pi\frac{dB_\nu}{dT}\bigg|_{T=\overline{T}_{skin}} \cdot \frac{\Delta T_{skin}}{\Delta T_s}. \tag{B.4}$$

Here, the first term quantifies the derivative of the Planck function B_ν with respect to T, evaluated at the average T_{skin} of each regime; the second term quantifies the change in T_{skin} with T_s within each regime, calculated from a linear regression. This model is not meant to be realistic at most T_s, but it is useful to demonstrate the impact of surface emission at different T_s.

THE CONSTANT-$\mathcal{R}$ EXPERIMENT   The temperature profile for a given T_s follows a moist adiabatic lapse rate in the troposphere, whereas the stratosphere is isothermal with T = 200 K. Relative humidity $\mathcal{R}$ is vertically uniform and equal to the clear-sky column relative humidity $\mathcal{R}_c$ in ERA5, averaged over all T_s-bins within the respective regime. In the stratosphere, q is equal to the tropopause value. With this approach, we account for the "zero-order" effects on λ_ν, namely T_s and the average column relative humidity $\overline{\mathcal{R}_c}$ in each regime, while removing the effect of changes in $\mathcal{R}_c$ with T_s, similar to other single-column

studies (Jeevanjee et al., 2021a; Kluft et al., 2021; Seeley and Jeevanjee, 2021).

THE VARIABLE-$\mathcal{R}$ EXPERIMENT   The temperature profile for a given T_s again follows a moist adiabatic lapse rate, and $\mathcal{R}$ is again vertically uniform, but now it is set to the mean value of each given T_s bin. This way, we account for the effect of changes in $\mathcal{R}$ with T_s within each regime, the so-called relative humidity feedback, which is a first-order effect on λ_ν (Roemer et al., 2023a).

THE CONSTANT-LR EXPERIMENT   The temperature profile for a given T_s has a vertically uniform lapse rate (LR) of $\Gamma = 6.5\,\mathrm{K\,km^{-1}}$, while $\mathcal{R}$ is the same as in the variable-$\mathcal{R}$ experiment. However, due to the different T profiles, this corresponds to different values of q. This experiment was designed to produce a change in the T profile with T_s that is more in line with reanalysis than the assumption of a moist adiabat, which strongly overestimates the upper tropospheric amplification.

THE CLOSURE EXPERIMENT   The first three experiments do not capture the vertical variations of T and $\mathcal{R}$ changes with T_s seen in the reanalysis. These variations are very specific to our chosen T_s regimes and presumably mainly caused by the atmospheric circulation. Thus, an idealized representation of those vertical variations is not possible. To nevertheless assess the effect of those vertical variations, we perform a final experiment, where we use the actual average T and $\mathcal{R}$ profiles from ERA5 for each T_s bin. Furthermore, this experiment is used to test whether our simple model setup indeed produces convergence towards the observations.

B.3.2.4   *Radiative transfer model*

The atmospheric profiles from the different experiments are used to calculate clear-sky $\mathcal{L}_\nu$ spectra using the line-by-line radiative transfer model ARTS (Eriksson et al., 2011; Buehler et al., 2018). We calculate $\mathcal{L}_\nu$ between $10\,\mathrm{cm^{-1}}$ and $2000\,\mathrm{cm^{-1}}$ with a spectral resolution of $0.1\,\mathrm{cm^{-1}}$, using four streams per hemisphere. We include absorption of CO_2, H_2O, CH_4, and N_2O. Line absorption in ARTS is calculated using the internal ARTS Catalog Data, which in turn is based on the high-resolution transmission molecular absorption database (HITRAN, Gordon et al., 2022) as of 2022–05–02. Continuum absorption is calculated using the MT_CKD models for O_2 (version 1.0), CO_2 and N_2 (both version 2.5), as well as water vapor (version 4.0), which has also been included in both HITRAN and the ARTS Catalog Data (Mlawer et al., 2023). The simulated $\mathcal{L}_\nu$ spectra are then regressed against T_s to calculate λ_ν as described above.

These simulations are also used to derive brightness temperature spectra $T_{b,\nu}$ for each T_s, assuming isotropic radiation. These brightness temperatures are then averaged over the mid-infrared window excluding the O_3 absorption band ($800\,\text{cm}^{-1}$–$990\,\text{cm}^{-1}$ and $1080\,\text{cm}^{-1}$–$1200\,\text{cm}^{-1}$).

B.4   RESULTS

The observed spectral feedback λ_ν strongly varies with T_s (Figure B.2). Many of these variations can be explained using our existing understanding of λ_ν and the processes that are relevant at different T_s.

At very cold temperatures, λ_ν almost perfectly follows the derivative of the Planck curve, with the only exception being the reduced negative feedback in the CO_2 band (215 K, black line). As T_s increases, two major changes occur (245 K, purple line). First, the negative feedback weakens in the strongest part of the water vapor band (below $400\,\text{cm}^{-1}$), which already becomes opaque at these T_s. Second, the feedback becomes more strongly negative in the spectral regions that are still optically thin, namely the windows in the mid-infrared (MIR) and far-infrared (FIR) above $400\,\text{cm}^{-1}$, as the Planck response strengthens with T_s.

When increasing T_s further, λ_ν weakens throughout the FIR, as the atmosphere there becomes opaque and thus the FIR window closes (275 K, red line). At the same time, the feedback in the MIR window continues to get more strongly negative. At even higher T_s, the feedback starts to become less negative the MIR window (285 K, dark orange) as water vapor absorption there becomes non-negligible. In the FIR however, the feedback changes little, as it is now decoupled from T_s. The closing of the MIR window accelerates as T_s — and thus q — increases (295 K, light orange).

So far, the T_s dependence of λ_ν has been more or less consistent with model studies (Seeley and Jeevanjee, 2021; Kluft et al., 2021; Koll et al., 2023). However, this is decidedly not the case for the highest T_s bin, where the feedback abruptly becomes much more negative in the MIR window (305 K, yellow line). This is in stark contrast to model studies, which show a continuous weakening of the negative λ_ν in the window with T_s. This strongly negative λ_ν is not caused by its pure T_s dependence, but by circulation-induced variations in atmospheric temperature and humidity (see also Feng et al., 2023b).

However, from these observations alone, it is not obvious how exactly the observed λ_ν at different T_s is affected by those circulation-induced variations. This is therefore explored further in the following by comparing the observed λ_ν with simulated λ_ν for different experiments. Each of these experiments is designed to isolate the effect of different assumptions about the atmosphere, and thus to test our understanding of the processes governing λ_ν.
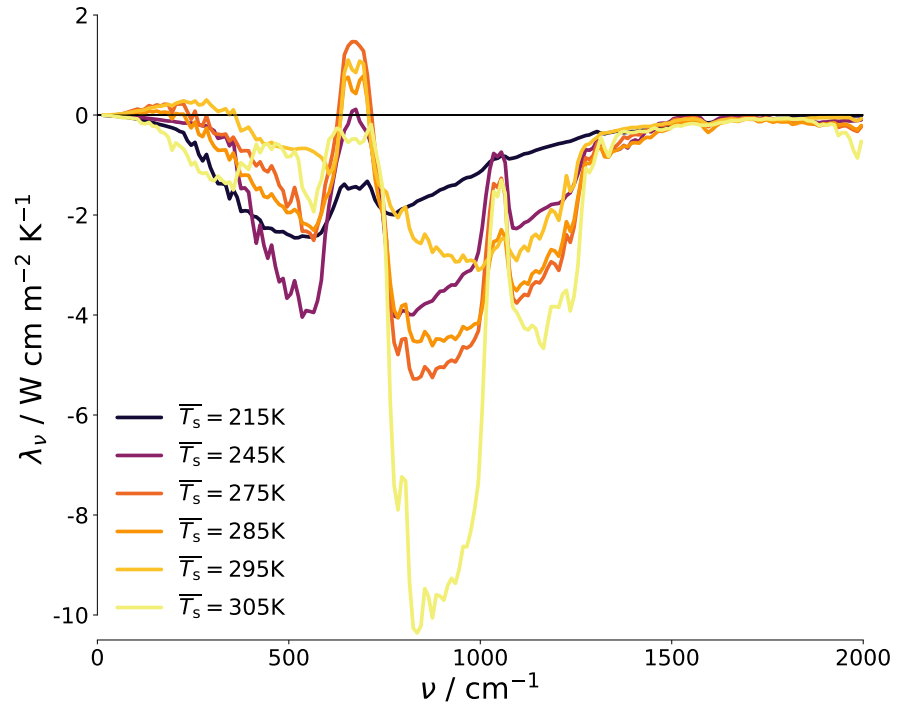
Figure B.2: Observed spectral longwave feedback λ_ν for different near-surface air temperatures T_s.

B.4.1   *Surface determines spectral feedback at low surface temperatures*

At $T_s < 270\,\text{K}$, λ_ν is mainly controlled by the surface. This is because the atmosphere contains very little water vapor and thus is almost transparent in large parts of the spectrum, particularly below $240\,\text{K}$. This leads to both observed and simulated λ_ν to be similar to the surface-Planck experiment in the window regions in the mid-infrared (MIR, $800\,\text{cm}^{-1}$–$1200\,\text{cm}^{-1}$) and far-infrared (FIR, $400\,\text{cm}^{-1}$–$550\,\text{cm}^{-1}$) (Figure B.3, bottom panel). The dominance of the surface also means that the simulated spectral feedbacks of the different atmospheric models are very similar, despite the fact that three of them have a far too cold atmosphere (Figure B.3, upper left panel).

However, the simulations systematically underestimate the observed spectral feedback in the MIR and FIR windows which are primarily sensitive to the surface. This discrepancy stems from differences in the skin temperature T_{skin}, which controls the radiation emitted by the surface and generally differs from the near-surface air temperature T_s. Generally speaking, $T_{skin} < T_s$ under strong radiative cooling of the surface, for example during (polar) night, and thus at low T_s. In contrast, $T_{skin} > T_s$ under strong radiative heating of the surface, for example in hot, dry regions with high T_s (see Figure B.4, solid gray line). The correct representation of T_{skin} is challenging, particularly for land, leading to substantial biases and errors in reanalysis T_{skin} compared to satellite observations (Trigo et al., 2015). The ERA5-Land reanalysis

we use as input overestimates T_{skin} by 1.4 K in the global mean, and errors are particularly large in polar regions (Muñoz-Sabater et al., 2021).

To estimate the effect of this error in T_{skin} on our simulations, we compare simulated and observed brightness temperatures T_b in the window (Figure B.4, black and teal dashed lines, respectively). These T_b are compared to the reanalysis T_{skin} from ERA5-Land which we use as input for our simulations (solid gray). As expected, the simulated T_b agree well with T_{skin} at low T_s because in the absence of atmospheric absorption by water vapor the radiation at the top of the atmosphere — and thus T_b — is almost entirely determined by T_{skin}. However, the observed T_b are around 5 K smaller than T_{skin} for $T_s < 240$ K. This means that with increasing T_s, the reanalysis T_{skin} used for our simulations increases much less than the actual T_{skin} implied by observations. This leads to the simulations substantially underestimating the observed spectral feedback in parts of the spectrum where surface emission can escape to space, namely in the windows in the MIR (for $T_s \leqslant 280$ K) and in the FIR (for $T_s \leqslant 250$ K).

B.4.2   *Changes in humidity affect spectral feedback for intermediate surface temperatures*

At T_s between 270 K and 290 K, the atmosphere is optically thick in the water vapor bands and thus atmospheric processes also affect the spectral feedback. In large parts of the spectrum, the observed spectral feedback is fairly well reproduced by the most simple constant-$\mathcal{R}$ experiment (Figure B.5). However, this experiment underestimates the negative spectral feedback in most parts of the optically thick water vapor bands in MIR and FIR, but also slightly in the window. This is because $\mathcal{R}$ decreases with T_s, which is not accounted for in the constant-$\mathcal{R}$ experiment. This decrease in $\mathcal{R}$ is due to the fact that within this T_s range, we move from the relatively humid storm-tracks in the mid-latitudes towards the drier subtropical regions (see Figure B.1).

To understand the effect of changes in $\mathcal{R}$ with T_s on λ_ν, it is important to note that for parts of the spectrum where water vapor is optically thick (and absorption by other greenhouse gases is negligible), constant $\mathcal{R}$ with T_s causes $\mathcal{L}_\nu$ in that part of the spectrum to approximately stay constant, implying a close-to-zero λ_ν (Simpson, 1928a,b; Ingram, 2010). In simple terms, constant $\mathcal{R}$ under warming can be thought of as roughly cancelling the opposite effects of increasing emission due to increasing atmospheric temperature and increased absorption due to increasing water vapor concentration q (Jeevanjee et al., 2021a). While this is a simplification neglecting the effect of pressure broadening (Feng et al., 2023a), it is a useful heuristic to understand the effect of changes in $\mathcal{R}$ with T_s on λ_ν. This framework
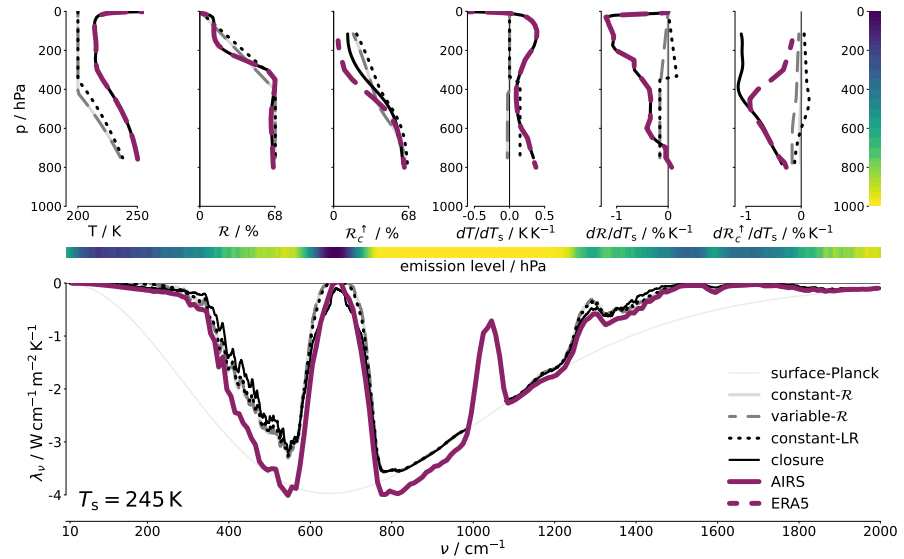
Figure B.3: Spectral longwave feedback λ_ν at near-surface air temperature $T_s = 245\,\mathrm{K}$ from observations (purple) and for the different single-column experiments (bottom). Also shown are the atmospheric profiles of temperature T, relative humidity $\mathcal{R}$, partial column relative humidity $\mathcal{R}_c^\uparrow$, as well as their changes with T_s between $240\,\mathrm{K}$ and $250\,\mathrm{K}$ for ERA5 (dashed purple) and for the different single-column experiments (top panels from left to right). For reference, the spectrally resolved emission level of outgoing longwave radiation $\mathcal{L}_\nu$ is color-coded to allow for a visual reference between the spectral and vertical dimensions. The simulated λ_ν (except for the Surface-Planck experiment) between $990\,\mathrm{cm}^{-1}$ and $1080\,\mathrm{cm}^{-1}$ are not shown because this spectral region is strongly impacted by O_3 absorption which we neglect in our simulations (see Section B.3.2.3)
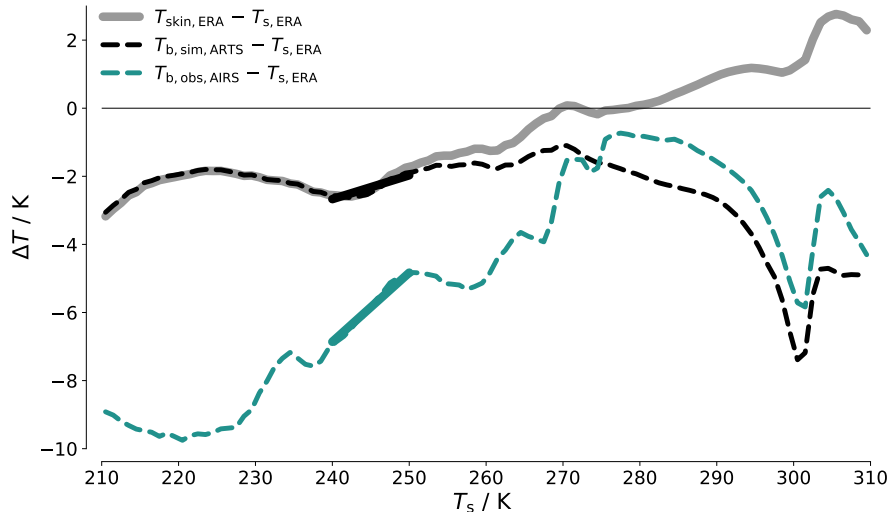
Figure B.4: Skin temperature from ERA5 reanalysis $T_{skin,ERA}$ as function of near-surface air temperature T_s (gray). For comparison, the simulated (black) and observed (teal) brightness temperatures T_b, averaged over the mid-infrared window, are shown as dashed lines. For better visibility, the reanalysis $T_{s,ERA}$ is subtracted from all variables. The different changes of $T_{b,sim}$ and $T_{b,obs}$ with T_s between 240 K and 250 K are exemplarily visualized as solid black and teal lines.

further implies that an increase in $\mathcal{R}$ with T_s causes a less negative (or even positive) λ_ν, while a decrease in $\mathcal{R}$ with T_s causes a more negative λ_ν (Roemer et al., 2023a).

Assuming a vertically uniform change in $\mathcal{R}$ with T_s in the variable-$\mathcal{R}$ experiment leads to a much better agreement with the observations in both the window and the FIR, where it reduces the deviations from the observed value by around half. This again demonstrates the importance of changes in $\mathcal{R}$ with T_s to accurately capture λ_ν (Roemer et al., 2023a). However, discrepancies remain, most notably in the FIR. The inclusion of a more realistic lapse rate in the constant-LR experiment does not provide any substantial improvements, showing that at these T_s, the major impact on λ_ν comes from changes in $\mathcal{R}$ with T_s. Rather, the remaining discrepancies in the far-infrared occur because the change in $\mathcal{R}$ with T_s varies vertically.

To understand the effect of these variations in more detail, it is useful to refine the heuristic approach from above, specifying how λ_ν depends on changes in $\mathcal{R}$ in different vertical layers. In the optically thick water vapor bands, most emission escaping to space originates from a relatively narrow layer, also called emission level. Any radiation emitted from lower atmospheric levels is completely absorbed by the atmosphere above. This in turn implies that changes in $\mathcal{R}$ below the emission level have no effect on the spectral outgoing longwave radiation $\mathcal{L}_\nu$, while changes in $\mathcal{R}$ at and above the emission level do.
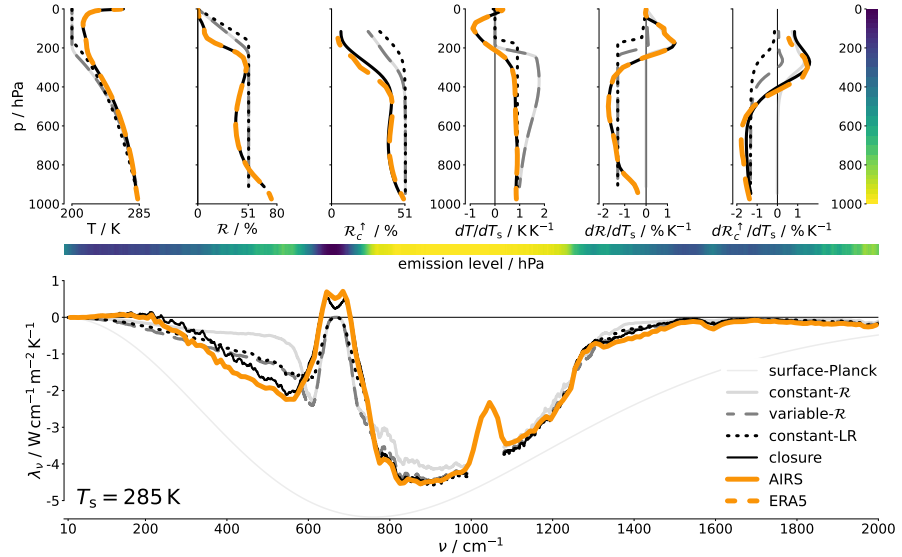
Figure B.5: Same as Figure B.3, but for $T_s = 285\,\text{K}$.

In particular, $\mathcal{R}$ around the emission level is important due to the strong decrease in q with altitude. To accurately represent this, we introduce the partial column relative humidity $\mathcal{R}_c^{\uparrow}(p)$. It is defined analogously to the column relative humidity, but only considers the parts of the atmosphere located above pressure level p. This means that λ_ν at wavenumbers with emission level p_{em} will be sensitive to changes in $\mathcal{R}_c^{\uparrow}(p_{em})$ with T_s.

We now come back to the observed spectral feedback around $285\,\text{K}$ (Figure B.5). Our simulations underestimate the negative feedback below $350\,\text{cm}^{-1}$, which is sensitive to the middle troposphere below around $500\,\text{hPa}$. In this region, our idealized experiments underestimate the decrease in $\mathcal{R}_c^{\uparrow}(p)$ with T_s (Figure B.5, upper right). Conversely, our simulations overestimate the negative feedback above $350\,\text{cm}^{-1}$, which is sensitive to the upper troposphere above around $250\,\text{hPa}$. In this region, our idealized experiments do not capture the increase in $\mathcal{R}_c^{\uparrow}(p)$ with T_s. Accounting for those vertical variations in the closure experiments reproduces the observed spectral feedback very well.

Similarly, our idealized experiments do not capture the decrease in stratospheric temperature with T_s and thus the positive observed feedback in the CO_2 band center. The inclusion of this effect in the closure experiment resolves this issue. In contrast, the variable-$\mathcal{R}$ and constant-LR experiments already reproduce the feedback in the MIR window very well. This demonstrates that in this spectral region, the feedback is not very sensitive to the exact vertical distributions of T and $\mathcal{R}$ or their changes with T_s, whereas these distributions are relevant for λ_ν in both the water vapor bands and the CO_2 band.

B.4.3   *Changes in humidity and temperature lapse rate affect the spectral feedback for high surface temperatures*

At $T_s > 290\,K$, λ_ν is also governed by both surface and atmosphere. The atmospheric part is strongly influenced by the atmospheric circulation, as with increasing T_s we move from the mild and dry maritime subtropics, to the warm and moist convective regions in the inner tropis, and finally to the hot and dry continental subtropics (see Figure B.1). Consequently, the λ_ν look very different at $295\,K$ and $305\,K$, respectively (Figures B.6 and B.7).

At $295\,K$, the observed feedback is less negative than at $285\,K$ throughout almost the entire spectrum. In the window, this effect can be explained by the increasing q, which continuously closes the window. This is demonstrated by the fact that the observed feedback is much less negative than that of the surface-Planck experiment (Figure B.6, bottom panel). In the far-infrared, however, the atmosphere is already optically thick, meaning that changes in the feedback only occur due to atmospheric processes. Most importantly, $\mathcal{R}$ increases with T_s around $295\,K$, which leads to a less negative atmospheric feedback, analogous to the arguments outlined in the previous section. For that reason, the constant-$\mathcal{R}$ experiment overestimates the negative feedback in large parts of the water vapor bands.

Furthermore, both variable-$\mathcal{R}$ and constant-LR experiments only capture the band-integrated feedback in the FIR, but not its spectral shape, because the increase in $\mathcal{R}$ also varies with height: $\mathcal{R}_c^\uparrow(p)$ increases with T_s below $700\,hPa$ and above $350\,hPa$, but slightly decreases with T_s in between. This means that the variable-$\mathcal{R}$ and constant-LR, which assume a vertically uniform change in $\mathcal{R}_c^\uparrow(p)$ overestimate the increase with T_s below $300\,hPa$, and thus simulate a slightly positive feedback between around 300 and $550\,cm^{-1}$, the spectral regions sensitive to that atmospheric layer, in contrast to the observed negative feedback. Conversely, these experiments underestimate the $\mathcal{R}_c^\uparrow(p)$ increase with T_s above $300\,hPa$ and thus simulate a negative feedback below $300\,cm^{-1}$, in contrast to the observed positive spectral feedback. Accounting for this vertical variation in the closure experiments produces good agreement with the observations.

The change in $\mathcal{R}$ with T_s also has a similar effect in the window, although this effect is much smaller relative to the total feedback there and occurs due to a slightly different mechanism: Changes in $\mathcal{R}$ with T_s can accelerate or decelerate the closing of the window due to increasing q with T_s: The variable-$\mathcal{R}$ experiment underestimates the negative feedback because it overestimates the increase in temperature — and thus absolute humidity — in the upper troposphere. The temperature increase is much better captured by the constant-LR experiment, which leads to a much more similar λ_ν compared to observations.

Finally, the experiments that assume a moist adiabatic temperature lapse rate (constant-$\mathcal{R}$ and variable-$\mathcal{R}$) substantially overestimate the negative feedback at the CO_2 band flanks. This is because the moist adiabatic lapse rate assumes a strong increase in upper tropospheric T with T_s, which leads to a strong spectral "radiator fin" feedback there (Seeley and Jeevanjee, 2021). However, the actual increase of tropospheric T with T_s on Earth's surface is much closer to a uniform increase, which is represented in the constant-LR experiment. Consequently, the "radiator fin" feedback in this experiment is much weaker and thus more similar to observations. This is consistent with previous findings that the moist adiabatic lapse rate overestimates the upper tropospheric amplification compared to both more comprehensive climate models and observations by radiosondes (Keil et al., 2021).

We can use similar arguments as above to explain the strongly negative observed feedback at 305 K, which is in stark contrast to modelling studies (Seeley and Jeevanjee, 2021; Kluft et al., 2021; Koll et al., 2023). Out of all analyzed T_s bins, $\mathcal{R}$ shows by far the strongest decrease with T_s at 305 K, which even exceeds 5 %/K in the lowest part of the troposphere. Consequently, the already partially closed window abruptly "re-opens", leading to much more surface emission escaping to space at 310 K than at 300 K. This is not captured by the constant-$\mathcal{R}$ experiment which strongly underestimates the negative feedback in the window at 305 K, but is mostly captured by the variable-$\mathcal{R}$ and constant-LR experiments. It is imortant to again emphasize that the mean $\mathcal{R}$ between 300 K and 310 K is the same by design in all experiments. Thus, it is the change in $\mathcal{R}$ with T_s that is needed to understand λ_v in the window at 305 K. Admittedly, these $\mathcal{R}$ changes are quite extreme, because they result from combining the moist Western Pacific Warm Pool region as well as dry desert regions into one regime, and not realistic to occur under global climate change. However, this still demonstrates that changes in $\mathcal{R}$ with T_s can have a substantial impact on λ_v even in the window.

However, even when accounting for this change in $\mathcal{R}$ with T_s, not even the closure experiment is able to capture the magnitude of the negative feedback between $800 \, cm^{-1}$ and $1000 \, cm^{-1}$. In fact, the observed λ_v is also more negative than the surface-Planck experiment in this spectral region. This discrepancy can be presumably explained by discrepancies between T_{skin} in reanalysis and observations. Although the largest discrepancies in T_{skin} occur at very low T_s, the reanalysis also seems to underestimate the increase of T_{skin} with T_s above 300 K (Figure B.4).

More generally, some discrepancies between our closure experiment and observations are to be expected due to the non-linear nature of radiative transfer. The observed λ_v is derived from averaging $\mathcal{L}_v$ spectra, while the modeled λ_v is derived by first averaging atmo-
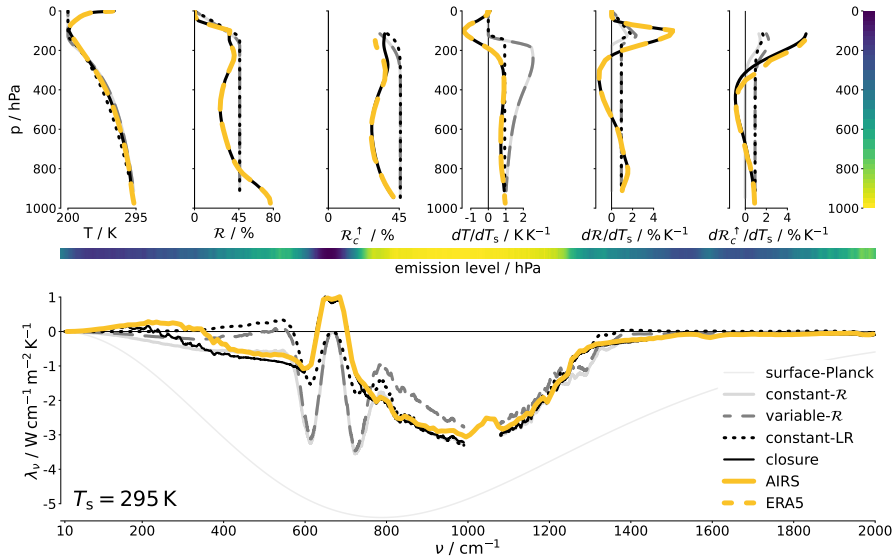
Figure B.6: Same as Figure B.3, but for $T_s = 295\,K$.

spheric profiles and then performing radiative transfer simulations based on those averaged profiles.

In the FIR, there are two compensating effects at play. The constant-$\mathcal{R}$ experiment happens to capture the observed feedback quite well, but for the wrong reasons. First, it does not account for the decrease in $\mathcal{R}$ with T_s. The experiments that account for this (variable-$\mathcal{R}$, constant-LR) exhibit much more negative feedbacks in the FIR. Second, all experiments strongly overestimate the change in tropospheric T with T_s. This is somewhat improved in the upper troposphere for the constant-LR experiment, leading to better agreement in λ_ν below $400\,\mathrm{cm}^{-1}$. However, even the constant-LR experiment does not capture the near-zero dT/dT_s above $600\,\mathrm{hPa}$ in reanalysis. This near-zero dT/dT_s is again presumably a feature of the atmospheric circulation, because the free-tropospheric temperature is determined by the convective regions with $T_s \approx 300\,\mathrm{K}$ and thus is roughly independent of local T_s. Accounting for this in the closure experiment leads to a much less negative λ_ν, which happens to almost exactly compensate the effect of decreasing $\mathcal{R}$ with T_s. Again, these changes in $\mathcal{R}$ and T with T_s are not realistic for global climate change, but they are useful to understand the effect of these changes on λ_ν.

B.5 CONCLUSIONS

We use satellite observations to investigate the dependence of the clear-sky spectral longwave feedback λ_ν on near-surface air temperature T_s between $210\,\mathrm{K}$ and $310\,\mathrm{K}$. Using single-column simulations we disentangle this T_s dependence from the effect of changes in atmospheric temperature and humidity induced by the general circulation.
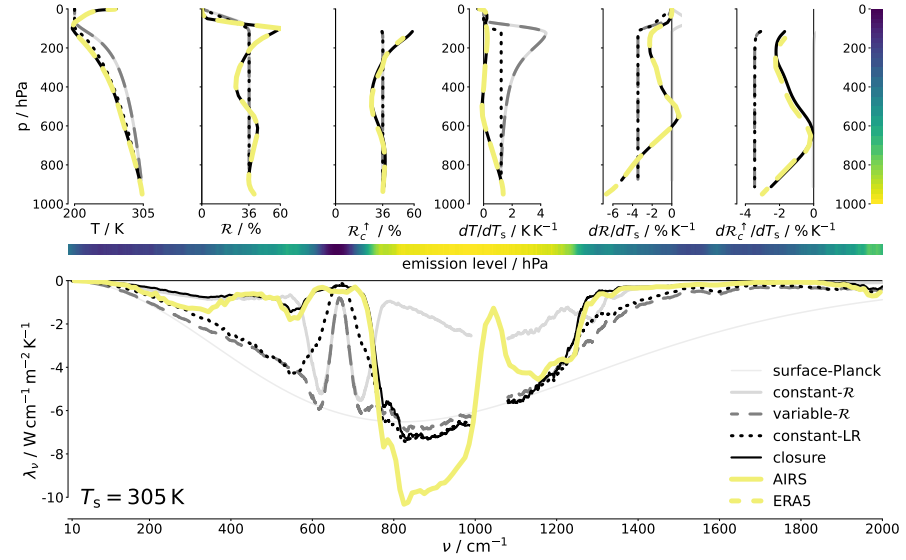
Figure B.7: Same as Figure B.3, but for $T_s = 305\,\mathrm{K}$.

We find that the "zero-order feedback" which only includes the effect of T_s and average column relative humidity $\overline{\mathcal{R}_c}$ (McKim et al., 2021) is not sufficient to understand the observed λ_ν at high T_s. Rather, "first-order" effects like the atmospheric profiles of T and $\mathcal{R}$ (Bourdin et al., 2021) and their column-mean changes with T_s (Roemer et al., 2023a) have a substantial effect. We even show that "second-order effects" like the vertical variations of the change in T and $\mathcal{R}$ with T_s (Pan and Huang, 2018) also play a role. This is particularly pronounced for $\mathcal{R}$ who's zero-, first- and second-order effects impact λ_ν throughout almost the entire spectrum, highlighting the uniquely important role of water vapor in shaping Earth's climate.

The substantial changes in $\mathcal{R}$ seen in some T_s regimes are caused by sampling different branches of the general circulation. Hence, they are unlikely to be representative of the changes under global climate change which are expected to be much smaller, at least in the global mean. However, these findings offer insights into how regional changes in $\mathcal{R}$ might affect the geographic distribution of λ. These regional $\mathcal{R}$ changes can be thought of as higher-order effects that modulate the fundamental distribution of λ — from deep tropical "furnaces" to subtropical "radiator fins" (Pierrehumbert, 1995; McKim et al., 2021).

Future warming will strongly depend on future changes in $\mathcal{R}$ and T with T_s. In the case of $\mathcal{R}$, these changes are thought to lie between $-1\,\%\,\mathrm{K}^{-1}$ and $+1\,\%\,\mathrm{K}^{-1}$, but both the sign and spatial distribution of this change are uncertain (e.g., Sherwood et al., 2010; Bourdin et al., 2021). Future changes in tropospheric T with T_s presumably follow a moist adiabatic lapse rate to first order, but substantial uncertainties remain regarding the effects of entrainment, freezing, and heat capacity (e.g., Keil et al., 2021, and references therein). While we make no

statement about sign or magnitude of these future changes in T and $\mathcal{R}$ with warming, our study provides the framework to understand how such changes affect λ_ν. Going forward, spectrally resolved satellite observations will thus be a valuable tool to better constrain the changes in T and $\mathcal{R}$ with warming, including their vertical distributions.

In this study, we build a step-by-step conceptual understanding what processes impact λ_ν at a wide range of T_s and show that the observed λ_ν can be fully explained using a simple atmospheric model with a small number of variables. With this observational constraint on the T_s dependence of λ_ν, we underpin the complete physical understanding of the strongest and most fundamental feedback in Earth's climate system, complementing model studies on this topic (e.g., Koll et al., 2023). Our findings also show that this understanding extends to T_s much lower and higher than Earth's current global-mean T_s. Given the fact that the global-mean λ determining Earth's climate sensitivity results from both spectral integration and spatial averaging, this full understanding of λ_ν at a wide range of T_s and ν provides further confidence in current estimates of λ. Furthermore, the solid understanding at a wide range of T_s also makes this approach suitable to study both past and future climates of Earth, but also climates of other Earth-like planets. On such planets, the uniquely important role of water vapor seen in Earth's atmosphere could instead be occupied by another condensable greenhouse gas such as CO_2, NH_3, or even CH_4, which might lead to surprising parallels to Earth's climate (e.g., Koll and Cronin, 2018).

DATA AVAILABILITY STATEMENT

The satellite data can be downloaded from https://disc.gsfc.nasa.gov/datasets/AIRSIL3MSOLR_6.1/summary?keywords=AIRSIL3MSOLR_6.1 (Huang, 2020). The reanalysis data from ERA5 and ERA5-Land can be downloaded from https://cds.climate.copernicus.eu (Hersbach et al., 2019a,b; Muñoz-Sabater, 2019). The radiative transfer model ARTS is available at 10.5281/zenodo.10868342 (Buehler et al., 2024). The processed data used in our analysis is available at 10.5281/zenodo.11394082 (Roemer and Buehler, 2024b).

C

EFFECT OF UNCERTAINTY IN WATER VAPOR CONTINUUM ABSORPTION ON CO$_2$ FORCING, LONGWAVE FEEDBACK, AND CLIMATE SENSITIVITY

The work in this appendix has been published as:

CONTRIBUTIONS Together with S. A. Bühler and R. Pincus, I conceived and outlined the study. L. Kluft helped with setting up the single-column atmospheric model. I performed the simulations, conducted the analysis and drafted the manuscript. All authors participated in discussing the results and revising the manuscript.

NOTE Compared to the published version, the version in this appendix includes minor formatting changes.

EFFECT OF UNCERTAINTY IN WATER VAPOR CONTINUUM ABSORPTION ON CO_2 FORCING, LONGWAVE FEEDBACK, AND CLIMATE SENSITIVITY

F. E. Roemer[1,2], S. A. Buehler[1], L. Kluft[3], and R. Pincus[4]

[1]*Center for Earth System Research and Sustainability (CEN), Meteorological Institute, Universität Hamburg, Hamburg, Germany*
[2]*International Max Planck Research School on Earth System Modelling (IMPRS-ESM), Hamburg, Germany*
[3]*Max Planck Institute for Meteorology, Hamburg, Germany*
[4]*Lamont-Doherty Earth Observatory, Columbia University, Palisades, New York, USA*

KEY POINTS

- Effect of continuum uncertainty on climate sensitivity is modest for a surface temperature of 288 K but substantial at higher temperatures

- Self and foreign continuum have opposite effects on longwave feedback at high surface temperatures

- Better understanding of continuum absorption is important to better constrain the temperature dependence of climate sensitivity

ABSTRACT

We investigate the effect of uncertainty in water vapor continuum absorption at terrestrial wavenumbers on CO_2 forcing $\mathcal{F}$, longwave feedback λ, and climate sensitivity $\mathcal{S}$ at surface temperatures T_s between 270 and 330 K. We calculate this uncertainty using a line-by-line radiative-transfer model and a single-column atmospheric model, assuming a moist-adiabatic temperature lapse-rate and 80 % relative humidity in the troposphere, an isothermal stratosphere, and clear skies. Due to the lack of a comprehensive model of continuum uncertainty, we represent continuum uncertainty in two different idealized approaches: In the first, we assume that the total continuum absorption is constrained at reference conditions; in the second, we assume

that the total continuum absorption is constrained for all atmospheres in our model. In both approaches, we decrease the self continuum by 10 % and adjust the foreign continuum accordingly. We find that continuum uncertainty mainly affects $\mathcal{S}$ through its effect on λ. In the first approach, continuum uncertainty mainly affects λ through a decrease in the total continuum absorption with T_s; in the second approach, continuum uncertainty affects λ through a vertical redistribution of continuum absorption. In both experiments, the effect of continuum uncertainty on $\mathcal{S}$ is modest at $T_s = 288\,\mathrm{K}$ ($\approx 0.02\,\mathrm{K}$) but substantial at $T_s \geqslant 300\,\mathrm{K}$ (up to $0.2\,\mathrm{K}$), because at high T_s, the effects of decreasing the self continuum and increasing the foreign continuum have the same sign. These results highlight the importance of a correct partitioning between self and foreign continuum to accurately determine the temperature dependence of Earth's climate sensitivity.

PLAIN LANGUAGE SUMMARY

Water vapor in Earth's atmosphere acts as a strong greenhouse gas by absorbing thermal radiation and thus plays a central role in controlling Earth's climate. Although water vapor absorption is well-understood overall, uncertainties remain in the so-called water vapor continuum, an absorption component that cannot yet be calculated from first principles. We investigate the impact of continuum uncertainty at terrestrial wavenumbers on climate sensitivity, the expected temperature increase that would result from a doubling of atmospheric CO_2 concentration. For this, we use a very simple climate model and represent continuum uncertainty in an idealized way. We find that uncertainty in the continuum mostly affects climate sensitivity by affecting the additional thermal radiation Earth emits to space as it warms. At temperatures similar to the current global average this effect is modest: changes in the water vapor continuum within the uncertainty only change climate sensitivity by 0.02 K, or about 1 %. However, at temperatures similar to those in tropical regions, changes in the continuum within the uncertainty change climate sensitivity by up to 0.2 K, or about 6 %. This shows that uncertainty in the water vapor continuum substantially contributes to uncertainty in the temperature dependence of climate sensitivity.

C.1   INTRODUCTION

Water vapor plays a central role in determining Earth's climate because it strongly absorbs and emits infrared radiation (Foote, 1856; Tyndall, 1861a,b). Absorption by water vapor is well-understood overall but substantial uncertainty remains in the water vapor continuum, an absorption component that varies smoothly in the spectral dimension, and that is more uncertain than the line spectrum (e. g., Baranov

et al., 2008; Ptashnik et al., 2011; Shine et al., 2012, 2016). Here we investigate the effect of this uncertainty at terrestrial wavenumbers on CO_2 forcing, longwave feedback, and climate sensitivity.

Uncertainty in the water vapor continuum fundamentally arises from uncertainty in the underlying physical processes. Possible explanations for the continuum discussed in the literature include far-wing absorption of single water vapor molecules (e. g., Clough et al., 1989; Ma and Tipping, 1991), absorption by bound and quasi-bound complexes of two water vapor molecules (e. g., Ptashnik et al., 2011; Mukhopadhyay et al., 2015) and of water and non-water molecules such as nitrogen or oxygen (e. g., Vigasin, 2000), as well as collision-induced absorption (e. g., Baranov and Lafferty, 2012). Although it seems likely that no single process is sufficient to explain the continuum, substantial uncertainty remains regarding the relative importance of these processes (e. g., Shine et al., 2012, 2016; Mlawer et al., 2023).

Therefore, continuum absorption cannot yet be calculated from first principles but is rather estimated using semi-empirical continuum models, most commonly the Mlawer-Tobin-Clough-Kneizys-Davies model (MT_CKD, Mlawer et al., 2023). This is commonly done by — somewhat arbitrarily — truncating water vapor absorption lines at $25\,cm^{-1}$ from the line center; the remaining water vapor absorption is then defined as continuum absorption (e. g., Clough et al., 1989; Tipping and Ma, 1995; Shine et al., 2012; Mlawer et al., 2023). This continuum absorption is further split into two components: (a) The self continuum comprises absorption due to interactions between two water molecules and thus depends quadratically on water vapor volume mixing ratio q; furthermore, self continuum absorption decreases with temperature T. (b) The foreign continuum comprises absorption due to interactions between a water molecule and a non-water molecule and thus depends linearly on q, with no known dependence on T (e. g., Burch and Alt, 1984; Shine et al., 2016; Mlawer et al., 2023).

To accurately determine the water vapor continuum and its components, models rely on data from laboratory measurements (e. g., Paynter et al., 2009; Odintsova et al., 2022; Fournier et al., 2024), satellite observations (e. g., Newman et al., 2012), and field campaigns (e. g., Serio et al., 2008; Liuzzi et al., 2014). However, those measurements still exhibit both substantial spread and spectral gaps which further contribute to uncertainty (Baranov et al., 2008; Ptashnik et al., 2011; Shine et al., 2016). This uncertainty concerns both the absorption of solar radiation in the visible and near-infrared spectral ranges as well as the absorption of terrestrial radiation in the mid- and far-infrared spectral ranges (Shine et al., 2016). In this study, we exclusively focus on the effect of the continuum on terrestrial radiation.

Continuum absorption is strongest within water vapor absorption bands but its climate impact is strongest in the atmospheric windows where the self continuum is often the dominant absorber (Figure C.1). In the context of terrestrial radiation, the mid-infrared window ($750\,\text{cm}^{-1}$ to $1250\,\text{cm}^{-1}$) is particularly relevant because a substantial part of the outgoing longwave radiation $\mathcal{L}$ is emitted here.

As surface temperature T_s increases — and relative humidity stays constant — q increases exponentially. This increase in q causes both self and foreign continuum absorption to strongly increase with T_s, more than offsetting the self continuum's negative direct dependence on T (Pierrehumbert, 2010). At $T_s \approx 300\,\text{K}$ continuum absorption becomes optically thick which closes the mid-infrared window and strongly inhibits Earth's ability to radiate energy to space (e.g., Koll and Cronin, 2018). This directly affects Earth's longwave feedback λ, the change in $\mathcal{L}$ with T_s. Furthermore, both self and foreign continuum mask part of the absorption by CO_2 and thus reduce the magnitude of CO_2 forcing $\mathcal{F}$ (Jeevanjee et al., 2021b). Consequently, continuum absorption directly affects climate sensitivity $\mathcal{S} = -\mathcal{F}/\lambda$, the temperature increase caused by a CO_2 doubling (e.g., Stevens and Kluft, 2023).

At the same time, uncertainty in self continuum absorption in the mid-infrared window is still around 10–20 % and does not seem to decrease over time (see Figure C.2, also e.g., Baranov et al., 2008; Shine et al., 2016). In many cases, uncertainty is even larger for the foreign continuum and within water vapor bands because measurements there are impeded by the very strong line absorption (Paynter and Ramaswamy, 2011, 2012). Furthermore, uncertainties in self and foreign continuum are usually correlated (see Section C.4, also e.g., Shine et al., 2016).

Given the direct effect of continuum absorption on $\mathcal{F}$ and λ, this substantial uncertainty raises two important questions: (a) How large is the resulting uncertainty in $\mathcal{F}$ and λ — and thus $\mathcal{S}$ — in the context of contemporary climate change? (b) How does this uncertainty affect the surface temperature dependence of these quantities (e.g., Meraner et al., 2013; Romps, 2020; Kluft et al., 2021; Seeley and Jeevanjee, 2021)? These surface temperature dependences can be helpful to investigate $\mathcal{F}$, λ, and $\mathcal{S}$ in past climates of Earth where the global-mean surface temperature was substantially lower or higher than it is today, but also to analyze how $\mathcal{F}$ and λ vary throughout different climate zones on present-day Earth.

To date, uncertainty in water vapor continuum absorption has mostly been discussed within the field of spectroscopy (e.g., Baranov et al., 2008; Ptashnik et al., 2011; Shine et al., 2012, 2016). In the climate community, the importance of the water vapor continuum for λ is well-established (e.g., Seeley and Jeevanjee, 2021; Koll et al., 2023; Stevens and Kluft, 2023), but much less is known about how uncertainty in
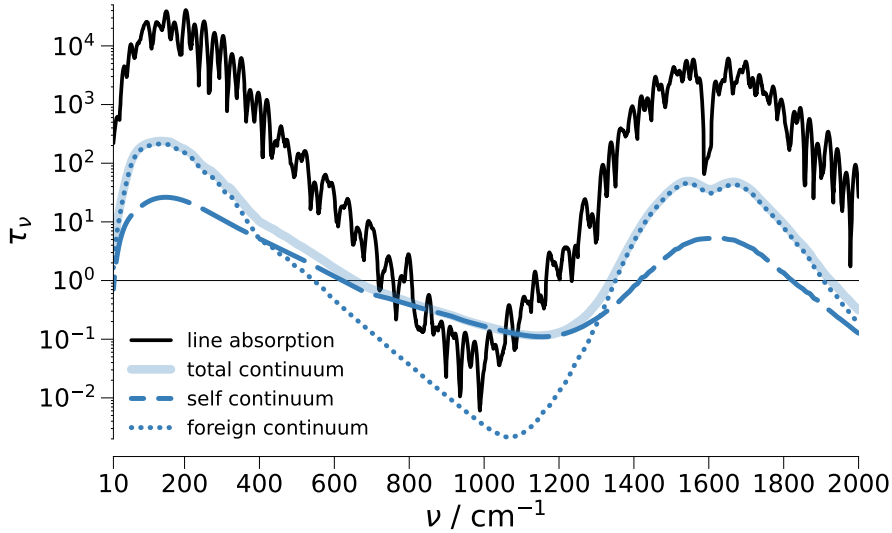
Figure C.1: Importance of water vapor continuum strongly varies spectrally. Shown are the spectrally resolved opacities τ_ν of water vapor as a function of wavenumber ν ($20\,cm^{-1}$ moving average) for an atmospheric column ($288\,K$ surface temperature, $80\,\%$ relative humidity). Shown are the τ_ν of water vapor lines (black), total water vapor continuum (light blue), as well as split into water vapor self continuum (dashed blue) and water vapor foreign continuum (dotted blue).
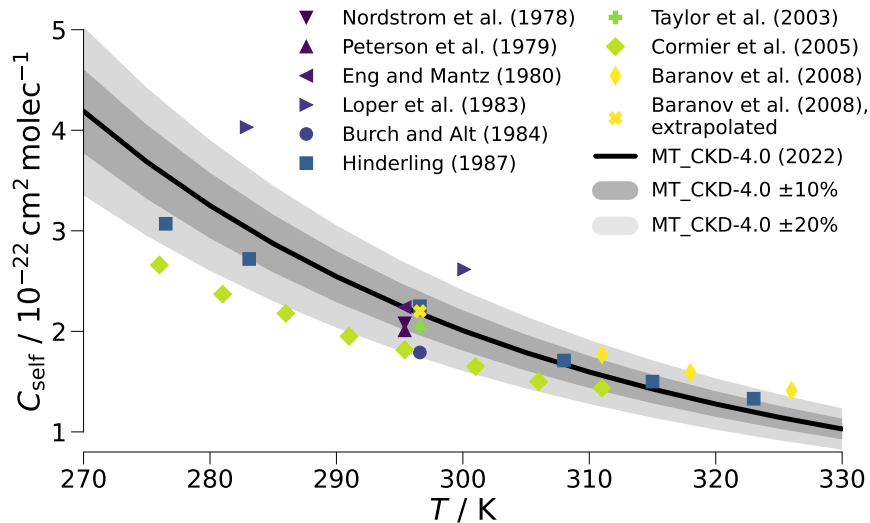

Figure C.2: Water vapor continuum absorption is still uncertain. As an example, the self continuum absorption cross-section C_{self} at $944.19\,cm^{-1}$ is shown as function of temperature T from MT_CKD version 4.0 (Mlawer et al., 2023) (line) and from laboratory measurements (symbols). The shaded areas correspond to differences of $\pm 10\,\%$ and $\pm 20\,\%$ from MT_CKD, respectively. The measurements at $296\,K$ are slightly offset along the temperature axis for better visibility. Laboratory data were read off from Baranov et al. (2008, their Figure 8) and Ptashnik et al. (2011, their Figure 7).

the continuum propagates to uncertainty in $\mathcal{L}$, $\mathcal{F}$, and λ (Kiehl and Ramanathan, 1982; Paynter and Ramaswamy, 2011, 2012), and how it affects $\mathcal{S}$.

To expand on those studies, we take a holistic look at the effect of uncertainty in water vapor continuum absorption at terrestrial wavenumbers on $\mathcal{F}$, λ and $\mathcal{S}$, as well as their temperature dependences, using an idealized atmospheric model. To this end, we first develop a conceptual understanding of how independent variations in self and foreign continuum absorption differently affect $\mathcal{F}$, λ, and $\mathcal{S}$ (Section C.3). We then investigate the effect of continuum uncertainty. Given the lack of a comprehensive model of continuum uncertainty, we represent this uncertainty using two different idealized approaches (Section C.4). Throughout, we illuminate the underlying processes by spectrally decomposing the effect of continuum uncertainty on $\mathcal{F}$ and λ, bridging the gap between spectroscopy and climate science.

C.2 METHODS

C.2.1 *Atmospheric model*

We use the single-column model konrad (Kluft et al., 2019; Dacie et al., 2019) to create profiles of temperature T and water vapor volume mixing ratio q on 256 vertical levels for surface temperatures $T_s \in [269\,\text{K}, 331\,\text{K}]$ in $1\,\text{K}$ increments. The T profiles follow a moist adiabat in the troposphere until they reach $175\,\text{K}$. Above, we assume a fixed isothermal stratosphere with $T = 175\,\text{K}$. This approach eliminates stratospheric feedbacks and allows us to focus exclusively on the troposphere.

Relative humidity is set to $80\,\%$ in the troposphere and stratospheric q is set to the tropopause value. The effect of this simplified assumption is discussed in Section C.5.1. The concentrations of trace gases follow the convention of the Aqua-Planet Experiment also used in the Radiative-convective equilibrium model intercomparison project (Wing et al., 2018): $348\,\text{ppm}$ CO_2, $1650\,\text{ppb}$ CH_4, and $306\,\text{ppb}$ N_2O. The O_3 concentration follows the profile derived by Wing et al. (2018), which is a function of pressure only and does not account for changes caused by the vertical expansion of the troposphere with T_s. However, this approach captures the first-order effect of ozone, namely the masking of emission in the window.

C.2.2 *Radiative transfer model*

For each T_s we calculate the spectrum of clear-sky outgoing longwave radiation $\mathcal{L}_\nu$ using the line-by-line radiative transfer model ARTS (Eriksson et al., 2011; Buehler et al., 2018). We perform the

calculations at 32768 (2^{15}) frequencies uniformly spanning the spectral range $10\,\text{cm}^{-1}$ to $3{,}250\,\text{cm}^{-1}$, accounting for absorption by water vapor, CO_2, CH_4, N_2O, O_3, N_2 and O_2.

Line absorption in ARTS is calculated using the internal ARTS Catalog Data, which in turn is based on the high-resolution transmission molecular absorption database (HITRAN, Gordon et al., 2022) as of 2022–05–02. Continuum absorption is calculated using the latest (at the time of analysis) MT_CKD models for CO_2 and N_2 (both version 2.5), O_2 (version 1.0), as well as water vapor (version 4.0), which has also been included in both HITRAN and the ARTS Catalog Data (Mlawer et al., 2023). At the time of writing, the only changes made since concern minor revisions of the water vapor foreign continuum in version 4.1.1 (Mlawer et al., 2023). Consistent with MT_CKD, water vapor lines are cut off at $25\,\text{cm}^{-1}$ from the line center. Wings beyond that wavenumber and the associated "pedestal" under the line are removed, as described in detail in Clough et al. (1989).

c.2.3 CO_2 forcing, longwave feedback, and climate sensitivity

For each T_s we calculate the spectrally resolved clear-sky $2 \times CO_2$ radiative forcing $\mathcal{F}_\nu$ by performing simulations of spectrally resolved clear-sky outgoing longwave radiation $\mathcal{L}_\nu$ at two different CO_2 concentrations: a baseline concentration of 348 ppm (note that this differs from the often-used pre-industrial value of 280 ppm) and a doubled CO_2 concentration of 696 ppm. The clear-sky spectral CO_2 forcing is then

$$\mathcal{F}_\nu(T_s) = -\left[\mathcal{L}_\nu(T_s, 696\,\text{ppm}\,CO_2) - \mathcal{L}_\nu(T_s, 348\,\text{ppm}\,CO_2)\right]. \quad \text{(C.1)}$$

Here $\mathcal{F}_\nu$ is the instantaneous radiative forcing, as our experimental setup does not allow for stratospheric cooling and the resulting radiative adjustment. However, as the stratosphere contains so little water vapor, the continuum presumably has no impact on the adjustment process, and thus continuum uncertainty is expected to have the same effect on instantaneous forcing as it would on effective forcing, the relevant quantity for calculating climate sensitivity.

For each T_s we calculate the spectrally resolved clear-sky longwave feedback λ_ν as the centered finite difference

$$\lambda_\nu(T_s) = -\frac{\mathcal{L}_\nu(T_s + 1\,\text{K}, T_{i+1}, q_{i+1}) - \mathcal{L}_\nu(T_s - 1\,\text{K}, T_{i-1}, q_{i-1})}{2\,\text{K}}, \quad \text{(C.2)}$$

where $x_{i\pm 1} = x(T_s \pm 1\,\text{K})$ for the profiles of temperature T and water vapor volume mixing ratio q, respectively.

The spectral surface feedback $\lambda_{\nu,\text{sfc}}$ is defined as the change in $\mathcal{L}_\nu$ that is caused by variations in T_s alone, with T and q unchanged. Therefore, we calculate it as

$$\lambda_{\nu,\text{sfc}}(T_s) = -\frac{\mathcal{L}_\nu(T_s + 1\,\text{K}, T_i, q_i) - \mathcal{L}_\nu(T_s - 1\,\text{K}, T_i, q_i)}{2\,\text{K}}, \quad \text{(C.3)}$$

where $x_i = x(T_s)$ for $x \in \{T, q\}$.

The spectral atmospheric feedback, the radiative signature of changes in T and q, is calculated as

$$\lambda_{\nu,\text{atm}}(T_s) = \lambda_\nu(T_s) - \lambda_{\nu,\text{sfc}}(T_s). \tag{C.4}$$

These spectrally resolved quantities are integrated to yield the broadband quantities as

$$a(T_s) = \int_{\nu_0}^{\nu_1} a_\nu(T_s)\, d\nu, \tag{C.5}$$

where $a \in \{\mathcal{F}, \lambda, \lambda_{\text{sfc}}, \lambda_{\text{atm}}\}$ and $(\nu_0, \nu_1) = (10\,\text{cm}^{-1}, 3250\,\text{cm}^{-1})$.

Finally, the longwave clear-sky climate sensitivity $\mathcal{S}$, the temperature increase caused by a CO_2 doubling assuming clear skies and constant albedo, is calculated as

$$\mathcal{S}(T_s) = -\frac{\mathcal{F}(T_s)}{\lambda(T_s)}. \tag{C.6}$$

C.2.4 *Emission fraction*

To analyze the different impacts of self and foreign continuum on λ_ν, we calculate the emission fraction f_{em} which represents which species dominates different spectral regions at different surface temperatures T_s. To this end, we calculate the spectrally resolved opacity $\tau_{\nu,s}(p)$ of each absorbing species s from the top of the atmosphere (TOA) to each pressure level p using ARTS. In addition to CO_2 and water vapor lines, we consider the self and foreign continuum separately.

The emission pressure $p_{\text{em},\nu,s}$ of each species is then defined as the largest p, that is, the lowest level, where $\tau_{\nu,s}(p) \leqslant 1$ as seen from TOA. From this, we define the "emitting" species at each wavenumber ν as the species with the smallest $p_{\text{em},\nu,s}$, that is, the species that emits from the highest level in the atmosphere. If no species has $\tau_{\nu,s} > 0.5$ at the surface, we neglect atmospheric emission and no "emitting" species is chosen for that wavenumber; if multiple species have the same $p_{\text{em},\nu,s}$, they all contribute to atmospheric emission so all of them are chosen as "emitting" species.

We separately consider three main spectral regions of interest: the FIR water vapor band (FIR, $200\,\text{cm}^{-1}$ to $600\,\text{cm}^{-1}$), the major CO_2 band ($600\,\text{cm}^{-1}$ to $750\,\text{cm}^{-1}$), and the atmospheric window ($750\,\text{cm}^{-1}$ to $1250\,\text{cm}^{-1}$). We define the emission fraction $f_{\text{em},s}(T_s)$ as the fraction of all simulated wavenumbers within each of those spectral regions at which each species s is the "emitting" species, estimating which species most strongly impacts atmospheric emission and thus λ at a given T_s.

C.2.5   *Uncertainty in continuum absorption*

We perform a number of different experiments in which we vary the magnitude of the water vapor continuum. Apart from the baseline experiment with the unaltered continuum, we separately vary the magnitude of self and foreign continuum by $\pm 10\%$. Finally, we perform two different experiments to represent continuum uncertainty in an idealized way. Both of them are based on the assumption that the total continuum absorption is well-constrained, and that the main uncertainty arises from the partitioning between self and foreign continuum. In the single-constraint experiment, we assume that the constraint on the total continuum applies at a single set of reference conditions, while in the general-constraint experiment, we assume that the constraint generally applies at all atmospheric conditions. In the following, these two experiments are described in more detail.

C.2.5.1   *The single-constraint experiment*

We assume that the spectrally resolved total continuum opacity $\tau_{,\text{cont}}$ is perfectly constrained for reference values of temperature $T_0 = 296\,\text{K}$, air pressure $p_0 = 1013\,\text{hPa}$, and water vapor volume mixing ratio $q_0 = 0.02$. These values are chosen to mimic conditions commonly present in both laboratory and field studies of the continuum, which provide a constraint on the total continuum absorption. For a discussion about the effect of the choice of q_0 see Section C.5.2.

We assume a spectrally uniform uncertainty in the self continuum of $\pm 10\%$, and account for the negative correlation between self and foreign continuum uncertainty by adjusting the foreign continuum accordingly. We derive this adjustment from the reference opacities $\tau_{,\text{self,o}} = \tau_{,\text{self}}(T_0, p_0, q_0)$ and $\tau_{,\text{foreign,o}} = \tau_{,\text{foreign}}(T_0, p_0, q_0)$. The scaling factor x_ν is then defined as the factor $\tau_{,\text{foreign,o}}$ has to be multiplied with to compensate for a change in $\tau_{,\text{self,o}}$ of $\pm 10\%$ so that the total continuum opacity at the given reference values is conserved. This yields

$$x_\nu^{\pm} = 1 \mp 0.1 \cdot \frac{\tau_{,\text{self,o}}}{\tau_{,\text{foreign,o}}}, \qquad (C.7)$$

where x_ν^{+} is the scaling factor for the foreign continuum if the self continuum is increased by $+10\%$ and vice versa.

This adjustment of the foreign continuum is only of $\mathcal{O}(10\%)$ in the water vapor bands, but exceeds 100% in the atmospheric windows, where the self continuum is much stronger than the foreign continuum. This large adjustment in the windows means that an increase of the self continuum by 10% would cause the new self continuum to be stronger than the current total continuum — and thus would require negative foreign continuum absorption to achieve radiative closure in the case of x_ν^{+}. This indicates that a substantially stronger
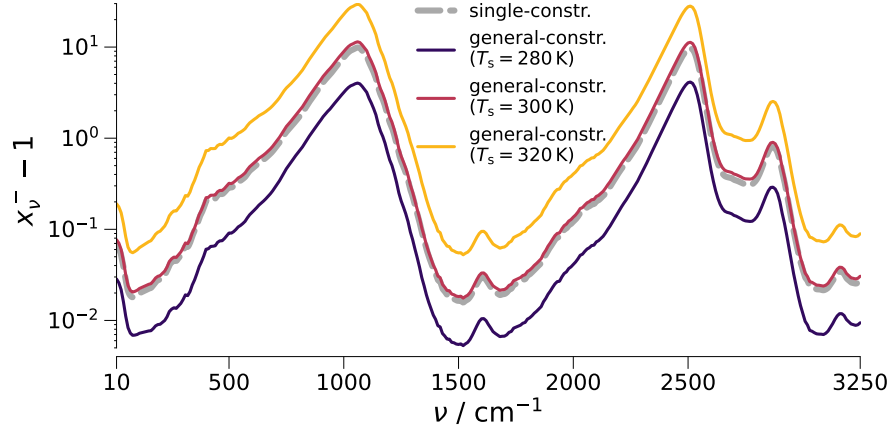
Figure C.3: Scaling factors x_ν^- for foreign continuum to compensate for change in self continuum of -10%. Shown are the x_ν^- for the single-constraint experiment (dashed) and the $x_\nu^-(T_s)$ general-constraint experiment for selected surface temperatures T_s (solid).

self continuum is unlikely, at least in the windows. This is also consistent with the fact that more recent laboratory studies based on cavity ring down spectroscopy observe weaker self continuum absorption in the $1000\,\text{cm}^{-1}$ window than predicted by MT_CKD 4.0 (Cormier et al., 2005; Fournier et al., 2024). Therefore, we only focus on the case where the self continuum is decreased by 10% and the foreign continuum is increased by factor x_ν^-.

C.2.5.2 *The general-constraint experiment*

We assume that the spectrally resolved column-integrated total continuum opacity $\tau_{,\text{cont}}$ is perfectly constrained for all of our atmospheric profiles. This means that we derive the foreign continuum scaling factor x_ν separately for each T_s, using the temperature and humidity profiles described in Section C.2.1. We calculate $\tau_{,\text{self}}(T_s) = \tau_{,\text{self}}(T_i, p_i, q_i)$ and $\tau_{,\text{foreign}}(T_s) = \tau_{,\text{foreign}}(T_i, p_i, q_i)$, where $x_i = x(T_s)$ for $x \in \{T, p, q\}$. From this, we analogously derive the scaling factor

$$x_\nu^-(T_s) = 1 + 0.1 \cdot \frac{\tau_{,\text{self}}(T_s)}{\tau_{,\text{foreign}}(T_s)}, \tag{C.8}$$

where, for the same reasons described above, we only consider the case of a 10% decrease in the self continuum and an increase in the foreign continuum by factor $x_\nu^-(T_s)$. Because the self continuum increases much more strongly with T_s than the foreign continuum, the adjustment of the foreign continuum strongly increases with T_s (Figure C.3).

C.3   EFFECT OF VARIATIONS IN SELF AND FOREIGN CONTINUUM

Before we proceed to investigate the impact of overall continuum uncertainty, this section first investigates the effect of variations in self and foreign continuum absorption in order to understand the relevant physical mechanisms. To this end, we separately vary the magnitude of self and foreign continuum absorption by $\pm 10\%$ throughout the whole simulated spectral range ($10\,\mathrm{cm}^{-1}$ to $3{,}250\,\mathrm{cm}^{-1}$). This way, we investigate how self and foreign continuum differently affect both CO_2 forcing and longwave feedback.

C.3.1   *Effect on CO_2 forcing*

Conceptually, the clear-sky CO_2 forcing $\mathcal{F}$ depends on two factors (Jeevanjee et al., 2021b). First, the temperature contrast between surface and stratosphere determines $\mathcal{F}$ in a dry atmosphere because surface emission is replaced with stratospheric emission at the edges of CO_2 absorption bands. Second, the presence of water vapor means that part of the original emission originates from the troposphere rather than the surface, due both water vapor line and continuum absorption. This change in the original emission level reduces the temperature contrast with the stratosphere and thus weakens $\mathcal{F}$.

At low T_s the spectrally resolved forcing $\mathcal{F}_\nu$ is most pronounced at the edges of the major CO_2 band ($600\,\mathrm{cm}^{-1}$ to $750\,\mathrm{cm}^{-1}$). At high T_s — and thus large water vapor volume mixing ratios q — water vapor absorption masks $\mathcal{F}_\nu$ at the CO_2 band edges, while the concomitant vertical expansion of the troposphere "unlocks" a substantial $\mathcal{F}_\nu$ in the CO_2 band center (Jeevanjee et al., 2021b; Kluft et al., 2021; Seeley and Jeevanjee, 2021, see also Figure C.4a). Overall, $\mathcal{F}$ increases with T_s until around $295\,\mathrm{K}$ due to the increasing surface-stratosphere temperature contrast; at even higher T_s the weakening effect of the exponentially increasing q dominates (Kluft et al., 2021, see also Figure C.5a). For the minor CO_2 bands in the atmospheric window around $950\,\mathrm{cm}^{-1}$ and $1050\,\mathrm{cm}^{-1}$ this decrease in $\mathcal{F}$ is roughly uniform, while for the major CO_2 band at $667\,\mathrm{cm}^{-1}$ $\mathcal{F}$ decreases slowly at first and much more strongly above $T_s \approx 315\,\mathrm{K}$ (see Figure C.5a).

Together with water vapor line absorption, the water vapor continuum determines the atmospheric layer whose emission is replaced by stratospheric emission when CO_2 is doubled. When continuum absorption is increased, the original emission level is located at lower temperatures. Hence, the temperature contrast with the stratosphere is smaller which weakens $\mathcal{F}$, and vice versa for a decreased continuum. Consequently, the effect of the continuum on $\mathcal{F}_\nu$ is mostly limited to the edges of the CO_2 absorption bands (Figure C.4e, i).

Due to the exponential Clausius-Clapeyron relation and the quadratic dependence of the self continuum on q, the effect of the self
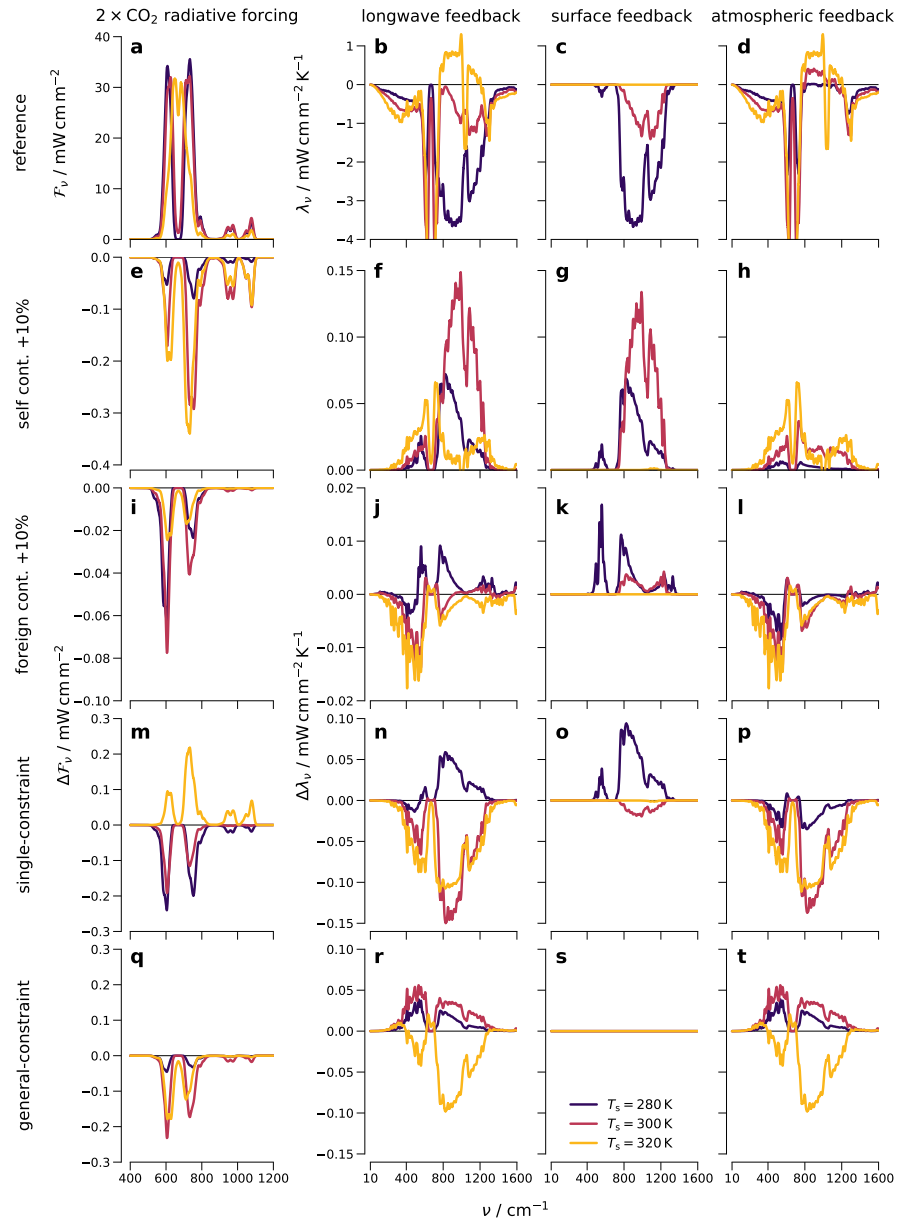
Figure C.4: Spectrally-resolved effect of water vapor continuum absorption on CO_2 forcing $\mathcal{F}_\nu$ (a, e, i, m) and longwave feedback λ_ν (b, f, j, n), which is also decomposed into surface feedback (c, g, k, o) and atmospheric feedback (d, h, l, p) for surface temperatures T_s of 280 K (black), 300 K (red), and 320 K (yellow). Shown are the baseline values (a-d), and the effects of 10 % increase in self continuum absorption (e-h) and foreign continuum absorption (i-l). Finally, the results are shown for the single-constraint (m-p) and general-constraint experiments (q-t).
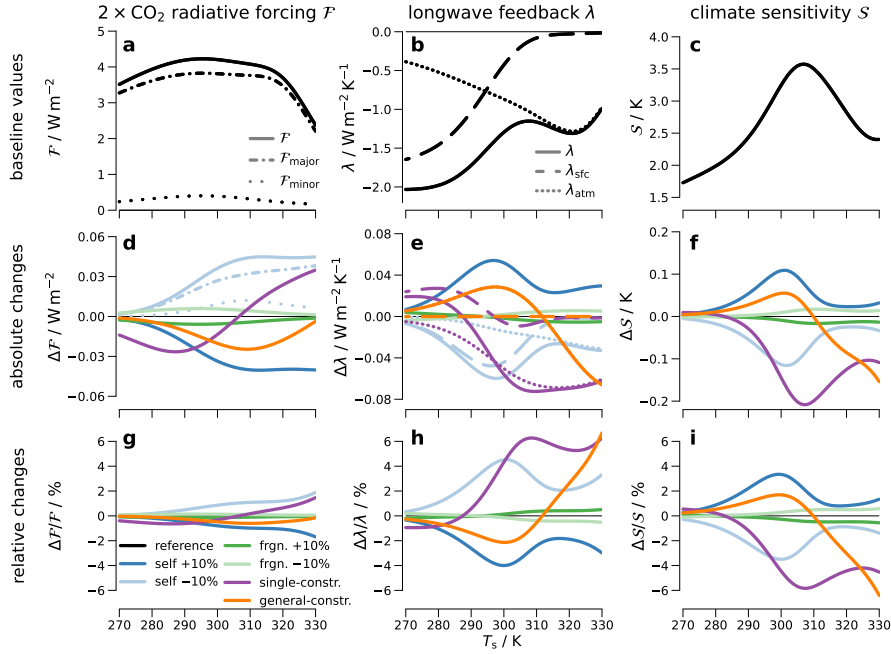
Figure C.5: Spectrally-integrated effect of water vapor continuum on CO_2 forcing $\mathcal{F}$ (a, d, g), longwave feedback λ (b, e, h), and climate sensitivity $\mathcal{S}$ (c, f, i). Shown are the total values (a, b, c) of the baseline simulation (black), as well as the absolute differences Δx (d, e, f) and relative differences $\frac{\Delta x}{x}$ (g, h, i) caused by variations in self continuum (blue) and foreign continuum (green) of $+10\%$ (dark shading) and -10% (light shading) for $x \in \{\mathcal{F}, \lambda, \mathcal{S}\}$. The same quantities are shown for the single-constraint experiment (purple), as well as for the general-constraint experiment (orange). For selected experiments, the forcing terms are split into the contribution by the major CO_2 band $\mathcal{F}_{major}$ ($\nu < 900\,\mathrm{cm}^{-1}$, dash-dotted) and minor CO_2 bands $\mathcal{F}_{minor}$ ($\nu > 900\,\mathrm{cm}^{-1}$, loosely dotted), and the feedback terms are split into surface feedback λ_{sfc} (dashed) and atmospheric feedback λ_{atm} (dotted).

continuum on $\mathcal{F}$ increases with T_s until around $310\,\text{K}$ and stays constant for even higher T_s (Figure C.5d,g). This results from compensation between the self continuum's effect on the forcing contributions of the major CO_2 band and the minor CO_2 bands. The effect of the self continuum on the forcing contribution of the minor CO_2 bands decreases above $310\,\text{K}$ because self continuum absorption becomes much stronger than CO_2 absorption in the window. This in turn is because CO_2 concentration stays constant with T_s in our experiments, while q increases exponentially. In contrast, the effect of the self continuum on the forcing contribution of the much stronger major CO_2 band continues to increase with T_s (Figure C.5d,g).

For the same perturbation of $\pm 10\,\%$, the foreign continuum has a much weaker effect on $\mathcal{F}$. Because it is much weaker in the atmospheric window than the self continuum, the foreign continuum only affects the major CO_2 band and mainly at $T_s \leqslant 310\,\text{K}$ (Figures C.4i and C.5d).

For $T_s = 288\,\text{K}$, the spectrally integrated effect of both water vapor self and foreign continuum on $\mathcal{F}$ is small: variations of $\pm 10\,\%$ in the self continuum only change $\mathcal{F}$ by less than $0.02\,\text{W}\,\text{m}^{-2}$ $(0.4\,\%)$, the same variations in the foreign continuum have an even smaller effect of $<0.01\,\text{W}\,\text{m}^{-2}$ $(0.1\,\%)$. Even at $T_s = 320\,\text{K}$ variations in the self continuum only change $\mathcal{F}$ by around $0.04\,\text{W}\,\text{m}^{-2}$ $(1\,\%)$. These uncertainties are smaller than those found by Paynter and Ramaswamy (2012), who assumed a larger, spectrally varying uncertainty in the continuum of up to $\pm 50\,\%$ and consequently found an uncertainty in $\mathcal{F}$ of up to $\pm 3\,\%$ (their Figure 14).

c.3.2 *Effect on longwave feedback*

Before we analyze the effect of variations in the water vapor self and foreign continuum on the longwave feedback λ, we briefly review the current understanding of its spectrally resolved counterpart λ_ν (Figure C.4b). In the atmospheric window ($750\,\text{cm}^{-1}$ to $1250\,\text{cm}^{-1}$), λ_ν is mostly governed by the strongly stabilizing (negative) surface feedback λ_{sfc}. However, the window continuously closes with increasing T_s which weakens λ_{sfc} and causes it to almost vanish at $T_s \approx 310\,\text{K}$ (e.g., Koll and Cronin, 2018; Kluft et al., 2021, see also Figures C.4c and C.5b). Above $310\,\text{K}$ the dependence of λ_ν in the window on water vapor volume mixing ratio q and thus on T_s is weaker than at lower T_s. This is because λ_{sfc} is replaced by a weakly destabilizing (positive) atmospheric feedback λ_{atm} caused by the water vapor continuum which is described in more detail below (Koll et al., 2023, see also Figures C.4d and C.5b). This atmospheric feedback is less sensitive to changes in T_s than λ_{sfc} is during the closing of the window, and thus the total feedback λ is less sensitive to T_s above $310\,\text{K}$.

Outside the window region, λ_v is almost entirely determined by λ_{atm}. In the center of the major CO_2 band ($600\,cm^{-1}$ to $750\,cm^{-1}$), λ_{atm} is close to zero at $T_s = 288\,K$ because the emission level there is located in the stratosphere but becomes strongly stabilizing at high T_s due to the vertical expansion of the troposphere. This stabilizing λ_{atm} is strongest at the band edges, where it is already present for $T_s < 288\,K$, but also reaches the band center at $T_s > 300\,K$. At $T_s > 320\,K$ the stabilizing λ_{atm} is weakened due to masking by water vapor absorption (Kluft et al., 2021; Seeley and Jeevanjee, 2021, see also Figures C.4d and C.5b).

Finally, λ_{atm} is weakly stabilizing in the water vapor bands in the far-infrared (FIR, $200\,cm^{-1}$ to $600\,cm^{-1}$) and mid-infrared (MIR, $1250\,cm^{-1}$ to $2000\,cm^{-1}$), which are dominated by water vapor line absorption. Here, the first-order approximation of a constant emission temperature would imply constant $\mathcal{L}$ with T_s — and thus a neutral λ_{atm} assuming $\tau \gg 1$ (Simpson, 1928a,b; Ingram, 2010; Jeevanjee et al., 2021a). However, this approximation does not hold entirely due to effects like pressure broadening which induce a weakly stabilizing λ_{atm} (Feng et al., 2023a; Koll et al., 2023, see also Figure C.4d).

Water vapor continuum absorption affects λ by altering both λ_{sfc} and λ_{atm} (Koll et al., 2023). In the following, we therefore discuss the partial feedbacks induced by separately increasing self and foreign continuum by 10 %. A destabilizing partial feedback means that the total feedback becomes less stabilizing, and vice versa.

The continuum dampens the stabilizing λ_{sfc} in the atmospheric window by damping surface emission. Hence, a stronger continuum dampens λ_{sfc} more and thus induces a destabilizing partial feedback at $T_s < 310\,K$, when the window is still open, and vice versa for a weaker continuum. This destabilizing partial feedback can be seen for both continuum components, but the effect of the self continuum (Figure C.4g) is much stronger than that of the foreign continuum (Figure C.4k) for the same perturbation of $+10\,\%$.

The continuum affects λ_{atm} because its emission temperature is sensitive to the temperature lapse rate. Because the moist-adiabatic lapse rate decreases with warming this leads to an additional increase in q. This in turn causes the continuum to emit at lower temperatures, giving rise to a destabilizing lapse-rate feedback (Koll et al., 2023). The effect of variations in the self continuum on λ_{atm} is weaker than that on λ_{sfc} below $T_s \approx 310\,K$ but becomes the dominant effect at higher T_s (Figure C.5e). Below $T_s \approx 300\,K$ the effect on λ_{atm} is mostly limited to the atmospheric window but it also reaches the absorption bands of water vapor and CO_2 at higher T_s. This destabilizing effect of an increased self continuum on λ_{atm} continuously increases with T_s in both water vapor and CO_2 absorption bands, while in the window it peaks at around 300 K and slowly decreases at higher T_s (Figure C.4h). In contrast, the foreign continuum has a weakly stabilizing effect on

λ_{atm} throughout the spectrum, particularly in the FIR water vapor band (Figure C.4l).

The stabilizing effect of a foreign continuum increase might seem surprising at first. To understand it, and also the other described changes, it is useful to think of them as resulting from shifts in the absorption species that control the main spectral regions as T_s increases. These shifts can be seen by looking at the emission fraction $f_{em,s}(T_s)$, which quantifies how much of the emission in a certain spectral band is controlled by species s at surface temperature T_s (see Section C.2.4 for details). This approach allows us to explain (a) differences between self and foreign continuum, (b) differences among spectral regions, and (c) dependence on surface temperature T_s (Figure C.6). The explanation relies on the dependences of the opacity of the different absorbing species on q and thus on T_s under constant relative humidity (Figure C.6 first column) which can be expressed as

$$\frac{dlog(\tau_{self})}{dT_s} > \frac{dlog(\tau_{H_2O\,lines})}{dT_s} > \frac{dlog(\tau_{foreign})}{dT_s} > \frac{dlog(\tau_{CO_2})}{dT_s}. \quad \text{(C.9)}$$

Regarding the opposite signs of the partial feedbacks of self and foreign continuum, the implications of Equation (C.9) are sketched for the FIR water vapor band (Figure C.6a). This sketch also builds on results of the radiative transfer simulations shown in Figure C.6b. The strong T_s dependence of τ_{self} means that the self continuum "gains ground" compared to the other species and thus $f_{em,self}$ strongly increases with T_s. In contrast, the weak T_s dependence of $\tau_{foreign}$ means that the foreign continuum "loses ground" compared to the other species and thus $f_{em,foreign}$ decreases with T_s. Accordingly, a stronger self continuum mostly reduces $\mathcal{L}$ at high T_s, while a stronger foreign continuum mostly reduces $\mathcal{L}$ at low T_s. Hence, $\mathcal{L}$ increases less strongly with T_s when the self continuum is increased but more strongly when the foreign continuum is increased. In other words, the self continuum induces a destabilizing partial feedback while the foreign continuum induces a stabilizing partial feedback. For the same perturbation of $\pm 10\,\%$ these partial feedbacks in the FIR have roughly the same magnitude at $T_s = 288\,\text{K}$, while the destabilizing self continuum partial feedback becomes much stronger at higher T_s (Figure C.6b).

Furthermore, this framework can also help us understand why the self continuum partial feedback varies among different spectral regions and with T_s. In contrast to the exponential Clausius-Clapeyron relation imposed on water vapor, CO_2 concentration stays constant with T_s in our experiments. Hence, $f_{em,self}$ in the CO_2 band strongly increases with T_s at the cost of CO_2 absorption. Therefore, the destabilizing lapse-rate feedback induced by the self continuum continuously masks more of the stabilizing Planckian response induced by CO_2 at the edges of the $667\,\text{cm}^{-1}$ CO_2 band, above $T_s \approx 320\,\text{K}$ this effect even reaches the band center (Figures C.4h and C.6c).
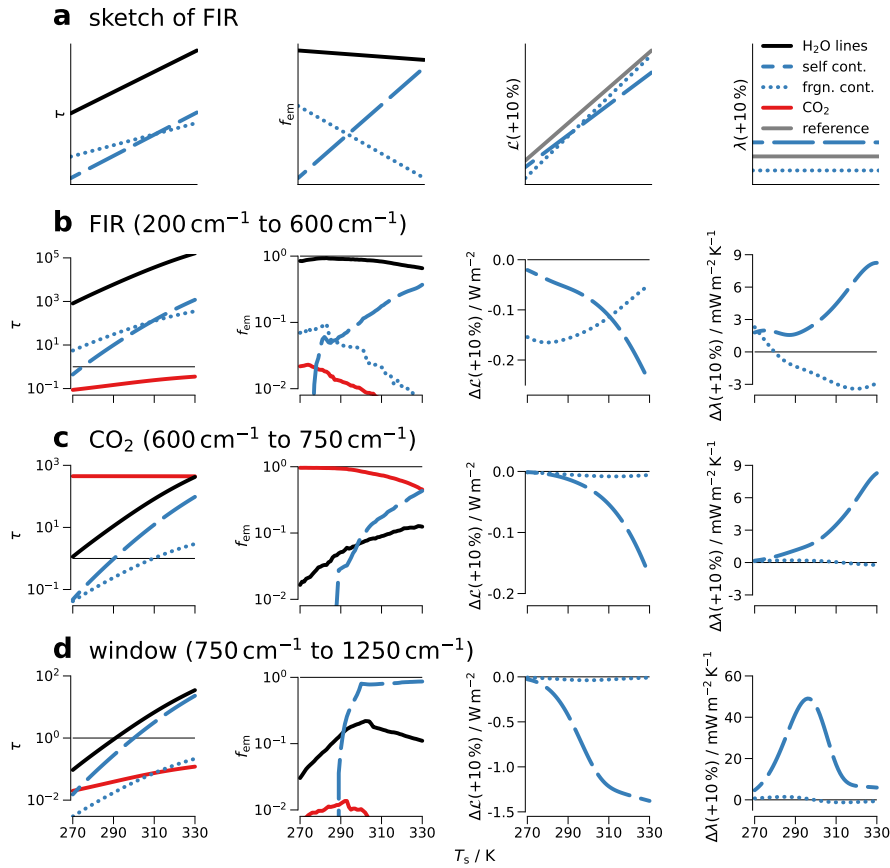
Figure C.6: Absorption species that control the different spectral regions shift with surface temperature T_s. Shown are band-averaged opacity τ (first column), band emission fraction f_{em} (second column), band-integrated outgoing longwave radiation $\mathcal{L}$ (third column), and band-integrated longwave feedback λ (fourth column). An idealized sketch of the mechanism in the far-infrared (FIR) water vapor absorption band is shown in the first row. Below, the actual values are shown for the FIR band, the major CO_2 band, and the atmospheric window. Note that the results shown in the third and fourth columns represent the changes in $\mathcal{L}$ and λ caused by increasing self and foreign continuum absorption by 10 %, except for the first row where the absolute values of $\mathcal{L}$ and λ are sketched.

In the window, $f_{\mathrm{em,self}}$ also increases with T_s along with the self continuum partial feedback. At $T_s \approx 300\,\mathrm{K}$, however, $f_{\mathrm{em,self}} \sim \mathcal{O}(1)$ which means that the self continuum controls most of the emission in the window. Further increasing T_s thus leads to a much weaker increase in $f_{\mathrm{em,self}}$ than below $300\,\mathrm{K}$ and thus the self continuum's destabilizing effect weakens (Figure C.6d).

Looking at the spectral integral, the effect of variations in the water vapor continuum on λ strongly varies with T_s. At $T_s = 288\,\mathrm{K}$ a $10\,\%$ stronger self continuum causes λ to become $0.04\,\mathrm{W\,m^{-2}\,K^{-1}}$ ($2\,\%$) less negative. This effect continuously increases with T_s and reaches a maximum of around $0.06\,\mathrm{W\,m^{-2}\,K^{-1}}$ ($4\,\%$) around $300\,\mathrm{K}$. Varying the foreign continuum by $\pm10\,\%$ has a much weaker effect. At T_s below around $295\,\mathrm{K}$ the foreign continuum's effect on the surface feedback dominates which causes a destabilizing partial feedback for an increase in foreign continuum absorption, and vice versa. At higher T_s the effect on the atmospheric feedback dominates, which causes a stabilizing partial feedback for an increase in foreign continuum absorption, and vice versa.

C.4   EFFECT OF CONTINUUM UNCERTAINTY

In the last section we have learned how variations in water vapor self and foreign continuum differently affect both CO_2 forcing $\mathcal{F}$ and longwave feedback λ by varying their magnitude separately. In this section, we build on this understanding and use it to investigate the effect of uncertainty in water vapor continuum absorption.

In order to properly represent this uncertainty, we need to consider that uncertainties in self and foreign continuum are not independent of each other. The foundation for our knowledge of the continuum is formed by field observations and laboratory measurements, both of which rely heavily on measurements of the total continuum. A change in the self continuum is thus usually accompanied by an opposite change in the foreign continuum to restore radiative closure, and thus uncertainties in self and foreign continuum are usually negatively correlated (Turner et al., 2004; Delamere et al., 2010; Mlawer and Turner, 2016; Shine et al., 2016; Mlawer et al., 2019, 2023). To explore the implications of this negative correlation, we consider two different idealized approaches, which are described in more detail in Section C.2.5.

C.4.1   *The single-constraint experiment*

The purpose of this experiment is to investigate the effect of uncertainty in the surface temperature dependence of the total continuum absorption. We therefore assume that the spectrally resolved total continuum opacity $\tau_{,\mathrm{cont}}$ is perfectly constrained at the reference condi-
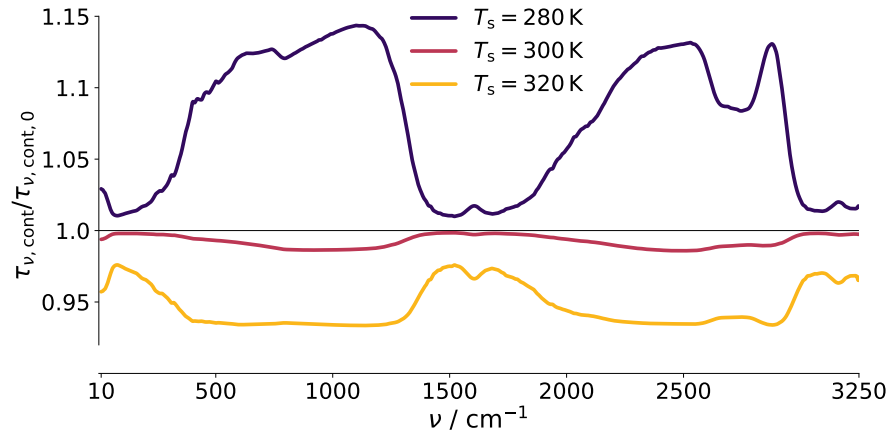
Figure C.7: Single-constraint experiment changes total continuum absorption in atmospheric profiles. Shown is the change in column-integrated total continuum opacity in the single-constraint experiment ($\tau_{\nu,\mathrm{cont}}$) relative to the baseline experiment ($\tau_{\nu,\mathrm{cont},0}$) for different surface temperatures T_s.

tions $T_0 = 296\,\mathrm{K}$, $p_0 = 1013\,\mathrm{hPa}$, $q_0 = 0.02$ (see Section C.2.5.1 for details). Due to the different dependences of self and foreign continuum on T and in particular q, this approach only conserves the total continuum opacity at the given reference conditions. This means that in atmospheres with $q < q_0$, the adjustment of the foreign continuum dominates, increasing the total continuum absorption relative to the baseline simulation. In contrast, in atmospheres with $q > q_0$, the adjustment of the self continuum dominates, decreasing the total continuum absorption (Figure C.7).

C.4.1.1   *Effect on CO$_2$ forcing*

Similar to the separate variations of self and foreign continuum discussed above, the CO_2 forcing $\mathcal{F}$ in the single-constraint experiment mainly changes at the edges of the main CO_2 band (Figure C.4m). At surface temperatures $T_s < 310\,\mathrm{K}$, the stronger foreign continuum dominates which leads to a slightly weaker $\mathcal{F}$; at $T_s > 310\,\mathrm{K}$ the weaker self continuum dominates which leads to a slightly stronger $\mathcal{F}$ (Figure C.5d). However, this effect on $\mathcal{F}$ is mostly weaker than $\pm 1\,\%$, at $T_s = 288\,\mathrm{K}$ $\mathcal{F}$ is reduced by $0.03\,\mathrm{W\,m^{-2}}$ ($0.6\,\%$).

C.4.1.2   *Effect on longwave feedback*

The effect on longwave feedback λ has different signs for different surface temperatures T_s as well (Figures C.4n and C.5e). At $T_s < 290\,\mathrm{K}$, the stronger foreign continuum dominates which causes a net destabilizing partial feedback. This mainly occurs because a stronger foreign continuum weakens the surface feedback which more than offsets the strengthening of the surface feedback due to the weaker self contin-

uum (Figure C.4g,k,o). However, this changes at $T_s \approx 300\,K$, when the effect of the self continuum on the surface feedback becomes dominant (Figures C.4o and C.5e). At $T_s \approx 315\,K$, the surface feedback diminishes, as already described in Section C.3.2.

Already at $T_s \approx 290\,K$, the stabilizing partial atmospheric feedback becomes stronger than the destabilizing partial surface feedback and thus the net partial feedback becomes stabilizing (Figure C.5e). In contrast to the surface feedback, the net effect on the atmospheric feedback is stabilizing throughout the simulated T_s range (Figure C.5e). This is because both a weaker self continuum and a stronger foreign continuum cause a stabilizing partial atmospheric feedback (see Section C.3.2 and Figure C.4h,l,p). This effect increases with T_s until around 320 K and stays roughly constant after (Figure C.5e).

The strongest effect occurs in the atmospheric window, where the magnitude of λ_{window} is increased by about $0.05\,W\,m^{-2}\,K^{-1}$ on average between 290 and 310 K. Because the magnitude of λ_{window} decreases by about $0.05\,W\,m^{-2}\,K^{-1}$ per 1 K increase in T_s, the single-constraint experiment lowers the value of T_s at which the atmospheric window closes by about 1 K. Phrased differently, because the opacity τ of continuum absorption continuously increases with T_s (Figure C.6 first column), variations in the continuum strength can be thought of as shifting τ in T_s space — and thus also the T_s at which the window closes.

At low T_s the partial feedback is destabilizing (positive) and almost entirely limited to the window. With increasing T_s the partial feedback becomes increasingly stabilizing (negative) throughout the spectrum, also affecting the far-infrared (FIR) water vapor absorption band (Figure C.4n). At very high T_s, the partial feedback becomes slightly less stabilizing in the window, while it continues to become more stabilizing in the FIR. This occurs because at those high T_s the continuum controls most of the emission in the window so further increasing T_s has a weaker effect on λ, while this is not the case in the FIR (see Section C.3.2 and Figure C.6).

Looking at the spectral integral, the effect on λ is modest at $T_s = 288\,K$: The destabilizing partial surface feedback and the stabilizing partial atmospheric feedback almost perfectly cancel, leading to a minimally stabilizing effect in λ of only $-0.002\,W\,m^{-2}\,K^{-1}$ (+0.1 %).

In contrast, the single-constraint experiment has a substantial effect at $T_s > 300\,K$, where it leads to a stabilizing partial feedback of around $-0.07\,W\,m^{-2}\,K^{-1}$ (+7 %) (dark purple line in Figure C.5e). At those T_s the single-constraint experiment has a much stronger effect on λ than a reduction of the self continuum by $-10\,\%$ alone (light blue line in Figure C.5e). This can be attributed to the strongly stabilizing effect of increasing the foreign continuum, which is discussed in detail in Section C.3.2.

c.4.1.3   *Implications for climate sensitivity*

The effect on climate sensitivity S is clearly dominated by the effect on the longwave feedback λ rather than on the CO_2 forcing F (Figure C.5g-i). At $T_s = 288\,K$ the effect is modest, with a reduction in S of only 0.02 K (0.8 %). At even lower T_s the slightly destabilizing effect on λ is compensated by its weakening effect on F which leads to almost no change in S. At higher T_s, however, the single-constraint experiment has a substantial effect: above 300 K the strongly stabilizing effect on λ clearly dominates over the increasing effect on F which reduces S by more than 0.2 K (7 %).

c.4.2   *The general-constraint experiment*

The purpose of this experiment is to investigate the effect of uncertainty in the vertical distribution of continuum absorption. We therefore assume that the column-integrated continuum opacity $\tau_{\nu,\text{cont}}$ is perfectly constrained for all of our atmospheric profiles (see Section C.2.5.2 for details). However, the redistribution of absorption between self and foreign continuum leads to changes in the vertical profile $\tau_{\nu,\text{cont}}(p)$. This vertical redistribution also occurs in the single-constraint experiment, but the general-constraint experiment allows for an isolation of the effect, without any changes in the column-integrated $\tau_{\nu,\text{cont}}$ with respect to the baseline simulation.

c.4.2.1   *Effect on outgoing longwave radiation*

To understand the effect on CO_2 forcing, longwave feedback, and climate sensitivity in the general-constraint experiment, it is helpful to take a step back and first analyze the effect on the outgoing longwave radiation spectrum $\mathcal{L}_\nu$. For almost all T_s, $\mathcal{L}_\nu$ is reduced compared to the baseline simulation, which is caused by changes in the vertical opacity profile $\tau_\nu(p)$. These changes occur because the quadratic dependence of the self continuum on q means that the self continuum is more concentrated in the lower troposphere ("bottom-heavy"), whereas the foreign continuum only depends linearly on q, and thus is somewhat less bottom-heavy. This is demonstrated by the ratio between self and foreign continuum opacity, which generally is highest in the lowest part of the troposphere (Figure C.8a). Consequently, by reassigning some of the absorption from the self to the foreign continuum, opacity is redistributed from the lower to the upper troposphere (Figure C.8b), which shifts atmospheric emission towards lower temperatures and thus reduces $\mathcal{L}_\nu$ (Figure C.8e).

   This reduction of $\mathcal{L}_\nu$ generally increases with T_s because self continuum opacity increases with T_s and thus more opacity is redistributed at higher T_s. However, at $T_s \gg 300\,K$, the effect starts to decrease again
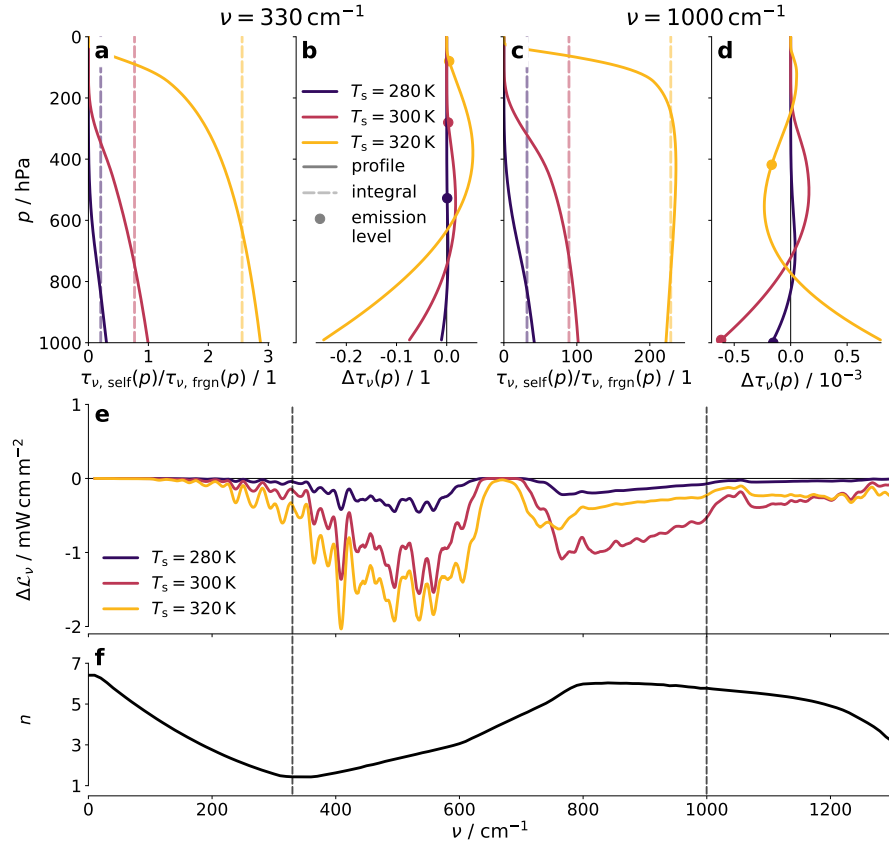
Figure C.8: Repartitioning of absorption between self and foreign contin-
uum vertically redistributes atmospheric opacity. Shown are the
vertically resolved ratio between opacities of self continuum
$\tau_{self}(p)$ and foreign continuum $\tau_{frgn}(p)$ (a, c) and change in total
opacity $\Delta\tau(p)$ in the general-constraint experiment with respect
to the baseline simulation (b, d) for wavenumbers $\nu = 330\,cm^{-1}$
(a, b) and $\nu = 1000\,cm^{-1}$ (c, d), for different surface tem-
peratures T_s. The column-integrated values are shown as light
dashed lines and the respective emission levels are shown as
solid circles. Also shown are the changes in spectrally resolved
outgoing longwave radiation $\Delta\mathcal{L}_\nu$ for the same T_s (e), and
the self continuum's temperature dependence exponent n from
MT_CKD 4.0 (f).

— first in the window (Figure C.8e) but at even higher T_s also in other parts of the spectrum (not shown).

This can be explained by the negative temperature dependence of the self continuum. In the MT_CKD 4.0 model, this is represented as

$$C_{self}(T) = C_{self}(296\,K) \left(\frac{296\,K}{T} \right)^n, \tag{C.10}$$

where C_{self} is the self continuum absorption cross-section and n is the spectrally varying temperature dependence exponent, which causes the self continuum absorption cross-section to decrease with T (Mlawer et al., 2023, see also Figures C.2 and C.8f).

Because $\tau_{self}(T) \propto C_{self}(T) \cdot q^2(T)$, the ratio $\tau_{self}/\tau_{foreign}$ still strongly increases with T_s throughout the troposphere in our experiments. Because of the strongly negative T dependence of C_{self} in the window, the high T in the lower troposphere causes the increase in $\tau_{self}/\tau_{foreign}$ with T_s to slow down substantially, while this effect is less pronounced in the cooler upper troposphere. In other words, while $\tau_{self}/\tau_{foreign}$ in the window is bottom-heavy at low T_s, it actually peaks at 400 hPa for $T_s = 320\,K$ (Figure C.8c)

Consequently, at sufficiently high T_s, replacing self continuum absorption with foreign continuum absorption becomes less effective in redistributing opacity from the lower to the upper troposphere in the window (Figure C.8d). In fact, most of the opacity is distributed from the middle troposphere to the lower troposphere. However, this presumably has no effect on $\mathcal{L}_\nu$ because the emission level in the window is around 400 hPa for $T_s = 320\,K$ (yellow circle in Figure C.8d). Conversely, some opacity is still redistributed from the middle to the upper troposphere. This redistribution reduces $\mathcal{L}_\nu$, but to a lesser extent than at lower T_s (Figure C.8e).

C.4.2.2   *Effect on CO_2 forcing*

In the context of CO_2 forcing $\mathcal{F}$, the redistribution of opacity from the lower to the upper troposphere means that this opacity can mask a larger part of the CO_2 absorption spectrum. Analogous to the arguments from Section C.3.1 (Jeevanjee et al., 2021b), this decreases $\mathcal{F}$ in the general-constraint experiment (Figure C.4q). Due to the vertical redistribution of absorption (Section C.4.2.1), the effect on $\mathcal{F}$ increases with T_s until around 310 K, and decreases again at higher T_s (Figure C.5d). Again, the effect is small in magnitude with around $-0.01\,W\,m^{-2}$ ($-0.2\,\%$) at 288 K and a maximum effect of $-0.025\,W\,m^{-2}$ ($-0.6\,\%$) at 310 K.

These results are similar in magnitude to the single-constraint experiment, both giving roughly an effect of $\mathcal{O}(1\,\%)$. However, the two approaches deliver quite different dependences on T_s. While the sign of the effect switches in the single-constraint experiment, it is negative for all T_s in the general-constraint experiment.

C.4.2.3 *Effect on longwave feedback*

At first glance, the effect on λ_v in the general-constraint experiment looks somewhat similar to that seen in the single-constraint experiment (Figures C.4n and C.4r). However, at closer inspection, it becomes clear that those results occur for quite different reasons. In the single-constraint experiment, the positive partial feedback at low T_s was due to the effect on λ_{sfc} (Figure C.4o). In the general-constraint experiment, however, the effect on λ_{sfc} is zero by construction (Figure C.4s), because λ_{sfc} is only affected by the column-integrated total τ_v, which is conserved. Rather, the entire effect on λ_v can be explained by the effect on the atmospheric feedback (Figure C.4t).

The reason for this is again the redistribution of absorption from the lower to the upper troposphere, as explained in Section C.4.2.1. The consequent reduction in $\mathcal{L}_v$ increases with T_s until around 310 to 320 K, depending on v, equivalent to a positive partial feedback. At higher T_s, the sign of the partial feedback switches from positive to negative as the $\mathcal{L}_v$ reduction starts to decrease with T_s (Figure C.5e).

Overall, the effect is in the same order of magnitude as for the single-constraint experiment, both giving effects of $\mathcal{O}(1\,\%)$ or less at 288 K and up to $\mathcal{O}(5\,\%)$ above 300 K. However, the two experiments disagree about both the sign of the effect and the exact T_s dependence.

C.4.2.4 *Implications for climate sensitivity*

The effect on $\mathcal{S}$ is again dominated by the effect on λ, while the effect on $\mathcal{F}$ is much weaker. At 288 K, $\mathcal{S}$ is increased by 0.02 K (1 %). The effect on $\mathcal{S}$ reaches a peak of around 0.05 K (2 %) at around 300 K. Following the T_s dependence of the effect on λ the sign of the effect on $\mathcal{S}$ switches at around 310 K, reaching a reduction of $\mathcal{S}$ of up to -0.15 K (6 %) at 330 K (Figure C.5f,i).

The two uncertainty experiments disagree on sign and T_s dependence of the effect of continuum uncertainty on $\mathcal{S}$. The difference is most pronounced at around 300 K, where both experiments predict a local maximum of the effect, but of opposite sign. However, they agree that the magnitude of the effect is of $\mathcal{O}(1\,\%)$ at 288 K and reaches $\mathcal{O}(5\,\%)$ above 300 K.

C.5 DISCUSSION

We have developed a careful mechanistic understanding of how uncertainty in the continuum at terrestrial wavenumbers affects CO_2 forcing $\mathcal{F}$, longwave feedback λ, and climate sensitivity $\mathcal{S}$; but how applicable is this to real world uncertainty? In the following, we address the assumptions underlying our idealized representations of atmosphere and spectroscopy and discuss their implications for the generalizability of our results.

c.5.1   *Atmospheric idealizations*

In our representation of the atmosphere, we make two major simplifications, both of which are widely used in idealized single-column studies of Earth's climate (e. g., Koll and Cronin, 2018; Jeevanjee et al., 2021b,a; Kluft et al., 2021; Seeley and Jeevanjee, 2021; Koll et al., 2023; Stevens and Kluft, 2023).

First, our single-column approach by design does not account for horizontal variations in temperature and humidity. The main effect of this approach is an underestimation of the effect of continuum uncertainty due to the non-linear dependence of the self continuum on q. To estimate the global mean effect, an average over all T_s weighted by their occurrence on Earth is better suited. The first-order effect of this can be estimated by simply averaging the simulated effects of continuum uncertainty over all T_s that are commonly observed on Earth (270 to 310 K). This gives an average effect of continuum uncertainty on climate sensitivity of around -0.07 K in the single-constraint experiment and $+0.03$ K in the general-constraint experiment. Those values are larger than the ± 0.02 K found for $T_s = 288$ K, but of similar magnitude, which suggests that this simplification does not qualitatively affect our results. Note that this estimate only captures variations in T_s, but not variations in relative humidity $\mathcal{R}$ at a given T_s which also occur in the real world. To properly account for this, one would need a realistic global climatology of T_s and $\mathcal{R}$, which is beyond the scope of our single-column approach.

Second, we assume a vertically uniform relative humidity profile $\mathcal{R} = 80\,\%$. This approach overestimates mid-tropospheric $\mathcal{R}$ compared to observational estimates, which generally lie between 40 % and 60 % (e. g., Sherwood et al., 2010; Wright et al., 2010). However, defining a non-uniform $\mathcal{R}$ profile for a wide range of T_s comes with its own challenges. Defining $\mathcal{R}$ as function of pressure does not capture the vertical expansion of the troposphere as T_s increases, hence it is best practice to define $\mathcal{R}$ as function of temperature instead (Romps, 2014). However, there are many degrees of freedom in choosing a function for $\mathcal{R}$, and the resulting feedback is often sensitive to details in the exact definition of this function (Bourdin et al., 2021). The main effect of assuming a vertically uniform $\mathcal{R}$ profile is an overestimation of the effect of continuum uncertainty due to an overestimation of mid-tropospheric $\mathcal{R}$. To estimate the effect of this assumption, we performed our analysis for an exemplary, and inherently somewhat arbitrary non-uniform $\mathcal{R}$ profile (Figure C.9), which is described in more detail in C.7. As expected the effect is somewhat reduced in magnitude, but apart from that the results look very similar (Figure C.10).

Therefore, rather than trying to capture both horizontal and vertical variations in $\mathcal{R}$ in a realistic way, the goal of this study is to develop a conceptual understanding of how continuum uncertainty propagates

to uncertainty in the radiative properties of the Earth. To this end, simplifying assumptions are generally much easier to interpret than results of more complex experiments, as they help to focus on the essential processes at play. Our conclusions regarding the different mechanisms by which self and foreign continuum affect forcing and feedback at different T_s, as well as the different effects of the two uncertainty experiments, do not seem to be affected by either of these simplifications.

c.5.2   *Spectroscopic idealizations*

Due to the lack of a comprehensive model for continuum uncertainty, we have to rely on idealized representations of this uncertainty. We perform two experiments based on different idealized representations of continuum uncertainty. Both of them are obviously not meant to be perfectly realistic; in fact, they can be considered rather extreme cases that isolate different aspects of continuum uncertainty.

In both approaches, we represent uncertainty by assuming a 10 % weaker self continuum compared with MT_CKD 4.0. This is arguably a conservative estimate, particularly in the 1000 cm^{-1} window, where a number of studies are consistent with a roughly 20 % weaker self continuum than in MT_CKD 4.0 (Burch and Alt, 1984; Cormier et al., 2005; Fournier et al., 2024, see also Figure C.2). Additional simulations we performed show that the effect of continuum uncertainty is to first order proportional to the assumed magnitude of uncertainty, so the effects of different magnitudes of continuum uncertainty can be estimated from the results presented here. This might also be useful to evaluate how future achievements in reducing continuum uncertainty affect uncertainty in climate sensitivity.

We further assume that continuum uncertainty is spectrally uniform. Given the fact that the continuum in different parts of the spectrum likely originates from different physical processes, this spectral uniformity is unlikely to properly represent actual continuum uncertainty. This caveat thus needs to be considered when interpreting the broadband quantities derived from this assumption.

Similarly, we discard the possibility that the self continuum might be stronger than current estimates because this would violate radiative closure in the windows. Although a stronger self continuum than in MT_CKD 4.0 is unlikely for the arguments outlined above, it cannot be entirely ruled out. However, unless the total continuum absorption in the windows is currently substantially underestimated, this increase in the self continuum would have to be much smaller than 10 % in the windows. In that case, the effect on S would presumably be qualitatively similar to the continuum uncertainty analyzed above, but with opposite sign and substantially reduced magnitude,

given that most of the effect of the continuum originates in the window.

Furthermore, we assume that total continuum absorption is perfectly known — under some reference conditions in the single-constraint experiment and even for all atmospheric profiles in the general-constraint experiment. In reality, instrumental errors limit the accuracy of continuum measurements and field studies of the continuum are additionally affected by aerosol effects (e.g., Shine et al., 2016). Both of these effects cause uncertainty in total continuum absorption and thus also in the magnitude of our foreign continuum adjustment. For a weaker adjustment than assumed above, the effect of continuum uncertainty can be estimated qualitatively from Figure C.5. The effect would roughly lie in between the case without foreign continuum adjustment (light blue) and either the single-constraint (purple) or general-constraint experiment (orange), respectively. This would imply a weaker effect on $\mathcal{S}$ at high surface temperatures and a still small effect for $T_s = 288\,\mathrm{K}$. For a stronger adjustment than assumed above, the effect of continuum uncertainty would be even stronger at high surface temperatures.

Moreover, we do not account for uncertainty in the temperature dependence of the self continuum. A recent comparison of different laboratory studies suggests that the negative temperature dependence might be overestimated in MT_CKD 4.0 (Fournier et al., 2024). This can be expected to induce additional uncertainty in $\mathcal{F}$, λ, and $\mathcal{S}$.

For the single-constraint experiment specifically, the choice of the reference values T_0, p_0, and q_0 themselves is to some extent arbitrary. The values we use are chosen to mimic conditions commonly present in both laboratory and field studies of the continuum. Different choices of these reference values, particularly of q_0, have a non-negligible quantitative impact on the effect of continuum uncertainty: For $q_0 = 0.01$, the foreign continuum adjustment is only half as strong compared to $q_0 = 0.02$, which reduces the effect on $\mathcal{S}$ by about one third at high T_s (Figure C.10). The biggest effect of q_0 is on the exact T_s at which the effects on $\mathcal{F}$ and λ change sign, while their magnitudes are in many cases quite similar. Regardless of the choice of q_0, the effect of continuum uncertainty on $\mathcal{S}$ is modest for $T_s = 288\,\mathrm{K}$ but substantial at high T_s.

For the general-constraint experiment, the combination of a perfectly constrained total continuum absorption for all T_s and a decrease in the self continuum, which strongly increases with T_s, is a rather extreme case. This is because this combination implies that the foreign continuum increases more strongly with T_s than is supported by our current understanding. This strong increase of the foreign continuum with T_s would either have to come from a stronger-than-linear dependence on q, which contradicts its definition, or from a strongly

positive dependence on T, which contradicts the current consensus that the foreign continuum is temperature independent.

Given the limited realism in our representations of continuum uncertainty therefore, the results presented in this study should not be viewed as conclusive quantitative statements on the exact effect of uncertainty in water vapor continuum absorption. However, they give a good picture of the magnitude and temperature dependence of the effect and illuminate the different processes at play.

C.6   SYNTHESIS

We have developed a conceptual understanding of how uncertainty in water vapor continuum absorption at terrestrial wavenumbers affects CO_2 forcing $\mathcal{F}$, longwave feedback λ, and climate sensitivity $\mathcal{S}$. This understanding is based on simulations that are idealized both in their treatment of the atmosphere and their representation of continuum uncertainty, which allows us to isolate different aspects of the effect of continuum uncertainty and analyze the underlying processes.

Our results highlight in particular the different effects of self and foreign continuum on λ, which arise from their different dependences on water vapor concentration q and temperature T. This has implications for both the dependence of the column-integrated continuum absorption on surface temperature T_s, and the vertical distribution of continuum absorption within the atmospheric column at a given T_s. This demonstrates the importance of a correct partitioning between self and foreign continuum absorption and its relevance for climate studies.

Overall, despite the substantial remaining uncertainty in water vapor continuum absorption at terrestrial wavenumbers, the impact of this uncertainty on $\mathcal{S}$ in our simulations is modest for $T_s = 288$ K. This is the case compared to both the overall uncertainty in $\mathcal{S}$ (Sherwood et al., 2020) and the much smaller uncertainty in the clear-sky longwave $\mathcal{S}$ studied here (Manabe and Wetherald, 1967; Kluft et al., 2019; Jeevanjee, 2023; Stevens and Kluft, 2023). However, continuum uncertainty has a substantial effect on $\mathcal{S}$ at T_s above 300 K. This causes a non-negligible effect in the global mean for present-day climate, but also directly affects the surface temperature dependence of $\mathcal{S}$.

Therefore, a better understanding of the processes that cause the water vapor continuum and better estimates of its magnitude would contribute to further constraining the temperature dependence of $\mathcal{S}$. This temperature dependence is for example relevant to understand past and possible future climates of Earth, but also those of Venus or Earth-like exoplanets, for example in the context of the runaway greenhouse effect (e. g., Goldblatt et al., 2013). It could also be useful to interpret estimates of $\mathcal{S}$ based on paleoclimate records from very warm climates such as the Paleocene-Eocene (e. g., Caballero and Hu-

ber, 2013). While continuum uncertainty only has a modest impact on $\mathcal{S}$ for $T_s = 288\,K$, it does affect estimates of $\mathcal{S}$ in very warm climates. Therefore, continuum uncertainty affects the relationship between $\mathcal{S}$ inferred from those paleoclimate records and $\mathcal{S}$ relevant for contemporary climate change.

For a more quantitative assessment, it would be important to develop a comprehensive model of continuum uncertainty which, to our knowledge, does not currently exist. Such a model would need to not only include the actual uncertainty in self and foreign continuum, but also account for the correlation between the two as a function of temperature and water vapor concentration, covering both terrestrial and solar wavenumbers. Once such a model exists, it will be possible to assess the exact effect of continuum uncertainty under different climate states and the implications for interpreting paleoclimate records. Furthermore, one could then quantify the effect under present-day climate for a realistic global climatology that accounts for horizontal and vertical variations in temperature and humidity, for example using a general circulation model.

C.7 APPENDIX: SENSITIVITY TO IDEALIZATIONS

To investigate the impact of the assumption of a vertically uniform relative humidity profile $\mathcal{R}$, we performed the same analysis as in Section C.4.2 for a non-uniform $\mathcal{R}$ profile. We chose a C-shaped $\mathcal{R}$ (Sherwood et al., 2010; Wright et al., 2010), defined as a function of atmospheric temperature T (Romps, 2014). The profile features vertically uniform $\mathcal{R} = 80\,\%$ from the surface to the top of the boundary layer ($T_s - 10\,K$). Above the boundary layer, $\mathcal{R}$ first linearly decreases to a minimum of $40\,\%$ in the mid-troposphere at $250\,K$, and then linearly increases again to $80\,\%$ at $175\,K$. The $\mathcal{R}$ for different T_s are shown as function of p (Figure C.9a) and T (Figure C.9b).

The effect of this profile on CO_2 forcing $\mathcal{F}$, longwave feedback λ, and climate sensitivity $\mathcal{S}$ is shown in Figure C.10. Due to the lower mid-tropospheric $\mathcal{R}$, λ is more negative (Figure C.10b), which results in a lower $\mathcal{S}$ (Figure C.10c). Regarding the effect of continuum uncertainty, the choice of $\mathcal{R}$ profile mainly affects the single-constraint experiment, where the relative effect on λ and $\mathcal{S}$ are reduced by about a third (Figure C.10h,i). For the general-constraint experiment, the effect of continuum uncertainty is only affected for $T_s > 300\,K$. Apart from that, the T_s dependence of all quantities is qualitatively very similar to the case of a vertically uniform $\mathcal{R}$ profile.

Finally, the effect of a different choice of $q_0 = 0.01$ for the single-constraint experiment is shown in Figure C.10. The effect on λ and $\mathcal{S}$ is increased at $T_s < 295\,K$ but decreased by up to a third at $T_s > 295\,K$ compared to the case of $q_0 = 0.02$ (Figure C.10h,i). Overall, the T_s dependence is again qualitatively similar.
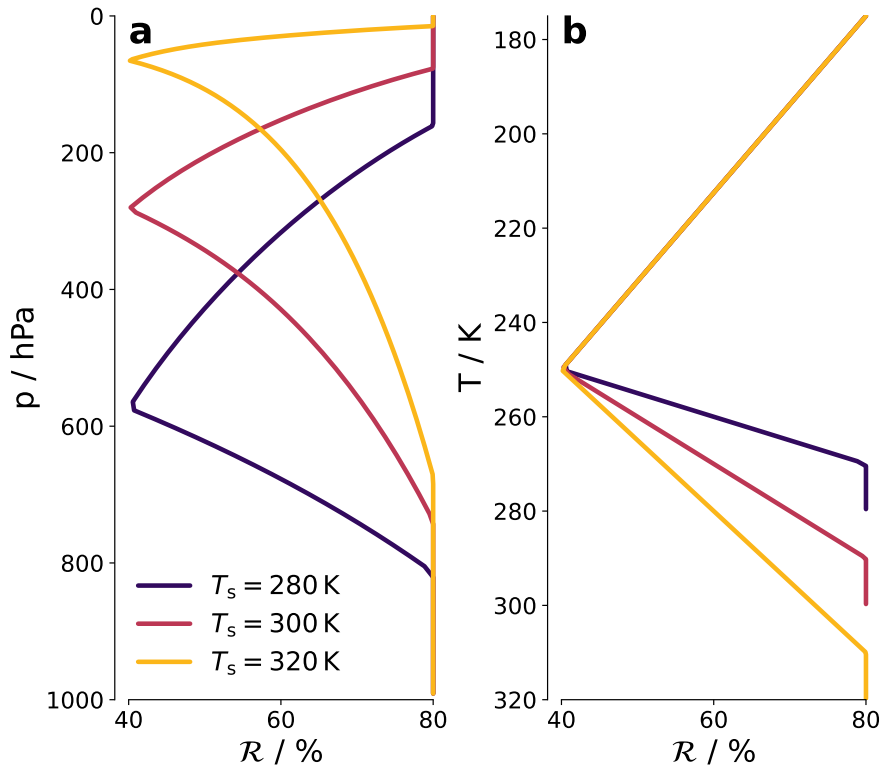
Figure C.9: Profiles of relative humidity $\mathcal{R}$ assuming vertically varying $\mathcal{R}$, plotted against pressure p (a) and temperature T (b).
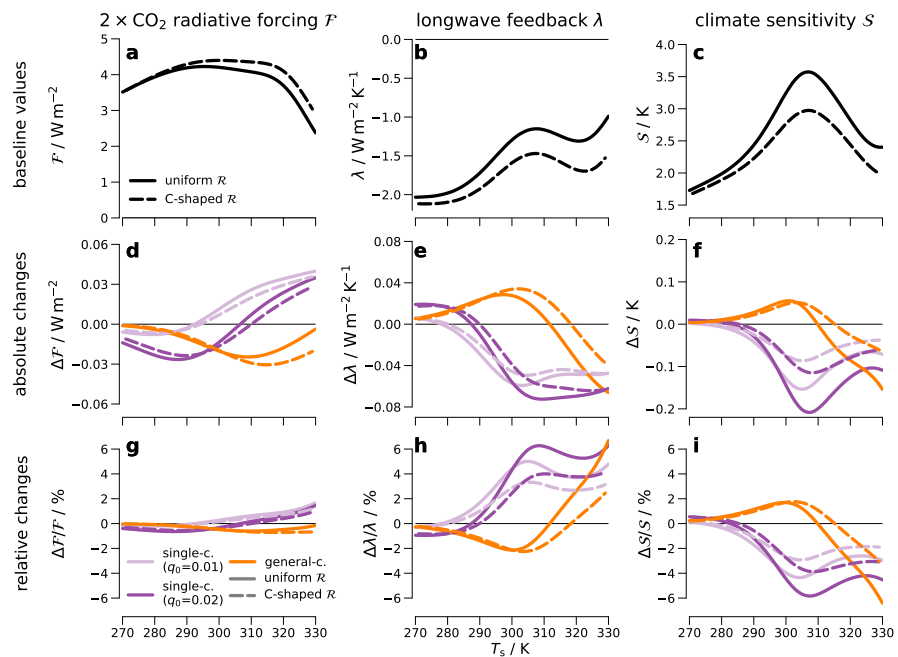
Figure C.10: Like Figure C.5 but now comparing the single-constraint (purple) and general-constraint (orange) for vertically uniform (solid) and C-shaped (dashed) $\mathcal{R}$ profiles. Additionally, the results of the single-constraint experiment are shown for the choice of $q_0 = 0.01$ (light purple).

DATA AVAILABILITY STATEMENT

Our analysis is based on the konrad model version 1.0.1 (available at 10.5281/zenodo.6046423 , Kluft et al., 2022), with some modifications to the model to support the scaling of absorption species (available at 10.5281/zenodo.10961148, Roemer et al., 2024b). For the radiative transfer simulations, we use the ARTS model version 2.6.2 (available at 10.5281/zenodo.10868342, Buehler et al., 2024). The model output produced in this study can be found at 10.5281/zenodo.10963797 (Roemer et al., 2024d), the code needed to run the models and produce the figures of this study can be found at 10.5281/zenodo.10963838 (Roemer et al., 2024c).

Andrews, T., J. M. Gregory, and M. J. Webb (2015). "The Dependence of Radiative Forcing and Feedback on Evolving Patterns of Surface Temperature Change in Climate Models." In: *Journal of Climate* 28.4. Publisher: American Meteorological Society Section: Journal of Climate, pp. 1630–1648. DOI: 10.1175/JCLI-D-14-00545.1.

Arrhenius, P. S. (1896). "XXXI. On the influence of carbonic acid in the air upon the temperature of the ground." In: *The London, Edinburgh, and Dublin Philosophical Magazine and Journal of Science*. Publisher: Taylor & Francis Group. DOI: 10.1080/14786449608620846.

August, T., D. Klaes, P. Schlüssel, T. Hultberg, M. Crapeau, A. Arriaga, A. O'Carroll, D. Coppens, R. Munro, and X. Calbet (2012). "IASI on Metop-A: Operational Level 2 retrievals after five years in orbit." In: *Journal of Quantitative Spectroscopy and Radiative Transfer*. Three Leaders in Spectroscopy 113.11, pp. 1340–1371. DOI: 10.1016/j.jqsrt.2012.02.028.

Aumann, H., M. Chahine, C. Gautier, M. Goldberg, E. Kalnay, L. McMillin, H. Revercomb, P. Rosenkranz, W. Smith Sr, D. Staelin, L. Strow, and J. Susskind (2003). "AIRS/AMSU/HSB on the Aqua mission: Design, science objective, data products, and processing systems." In: *Geoscience and Remote Sensing, IEEE Transactions on* 41, pp. 253–264. DOI: 10.1109/TGRS.2002.808356.

Baranov, Y. I. and W. J. Lafferty (2012). "The water vapour self- and water–nitrogen continuum absorption in the 1000 and 2500 cm-1 atmospheric windows." In: *Philosophical Transactions of the Royal Society A: Mathematical, Physical and Engineering Sciences* 370.1968. Publisher: Royal Society, pp. 2578–2589. DOI: 10.1098/rsta.2011.0234.

Baranov, Y. I., W. J. Lafferty, Q. Ma, and R. H. Tipping (2008). "Water-vapor continuum absorption in the 800–1250cm-1 spectral region at temperatures from 311 to 363K." In: *Journal of Quantitative Spectroscopy and Radiative Transfer* 109.12, pp. 2291–2302. DOI: 10.1016/j.jqsrt.2008.03.004.

Blumstein, D., G. Chalon, T. Carlier, C. Buil, P. Hebert, T. Maciaszek, G. Ponce, T. Phulpin, B. Tournier, D. Simeoni, P. Astruc, A. Clauss, G. Kayal, and R. Jegou (2004). "IASI instrument: technical overview and measured performances." In: *Infrared Spaceborne Remote Sensing XII*. Vol. 5543. SPIE, pp. 196–207. DOI: 10.1117/12.560907.

Boltzmann, L. (1884). "Ableitung des Stefan'schen Gesetzes, betreffend die Abhängigkeit der Wärmestrahlung von der Temperatur

aus der electromagnetischen Lichttheorie." In: *Annalen der Physik* 258.6, pp. 291–294. DOI: 10.1002/andp.18842580616.

Bony, S., R. Colman, V. M. Kattsov, R. P. Allan, C. S. Bretherton, J.-L. Dufresne, A. Hall, S. Hallegatte, M. M. Holland, W. Ingram, D. A. Randall, B. J. Soden, G. Tselioudis, and M. J. Webb (2006). "How Well Do We Understand and Evaluate Climate Change Feedback Processes?" In: *Journal of Climate* 19.15. Publisher: American Meteorological Society Section: Journal of Climate, pp. 3445–3482. DOI: 10.1175/JCLI3819.1.

Bony, S., B. Stevens, D. M. W. Frierson, C. Jakob, M. Kageyama, R. Pincus, T. G. Shepherd, S. C. Sherwood, A. P. Siebesma, A. H. Sobel, M. Watanabe, and M. J. Webb (2015). "Clouds, circulation and climate sensitivity." In: *Nature Geoscience* 8.4, pp. 261–268. DOI: 10.1038/ngeo2398.

Bouillon, M., S. Safieddine, J. Hadji-Lazaro, S. Whitburn, L. Clarisse, M. Doutriaux-Boucher, D. Coppens, T. August, E. Jacquette, and C. Clerbaux (2020). "Ten-Year Assessment of IASI Radiance and Temperature." In: *Remote Sensing* 12.15. Number: 15 Publisher: Multidisciplinary Digital Publishing Institute, p. 2393. DOI: 10.3390/rs12152393.

Bourdin, S., L. Kluft, and B. Stevens (2021). "Dependence of Climate Sensitivity on the Given Distribution of Relative Humidity." In: *Geophysical Research Letters* 48.8, e2021GL092462. DOI: 10.1029/2021GL092462.

Brindley, H. E. and R. J. Bantges (2016). "The Spectral Signature of Recent Climate Change." In: *Current Climate Change Reports* 2.3, pp. 112–126. DOI: 10.1007/s40641-016-0039-5.

Budyko, M. I. (1969). "The effect of solar radiation variations on the climate of the Earth." In: 21.5. Number: 5 Publisher: Stockholm University Press, p. 611. DOI: 10.3402/tellusa.v21i5.10109.

Buehler, S. A., P. Eriksson, O. Lemke, R. Larsson, S. Pfreundschuh, and M. Brath (2024). *ARTS - The Atmospheric Radiative Transfer Simulator*. DOI: 10.5281/zenodo.10868342.

Buehler, S. A., J. Mendrok, P. Eriksson, A. Perrin, R. Larsson, and O. Lemke (2018). "ARTS, the Atmospheric Radiative Transfer Simulator – version 2.2, the planetary toolbox edition." In: *Geoscientific Model Development* 11.4. Publisher: Copernicus GmbH, pp. 1537–1556. DOI: 10.5194/gmd-11-1537-2018.

Burch, D. E. and R. L. Alt (1984). *Continuum Absorption by H2O in the 700-1200 cm(-1) and 2400-2800 cm(-1) Windows,* tech. rep. Section: Technical Reports.

Byrne, M. P. and P. A. O'Gorman (2018). "Trends in continental temperature and humidity directly linked to ocean warming." In: *Proceedings of the National Academy of Sciences* 115.19. Publisher: Proceedings of the National Academy of Sciences, pp. 4863–4868. DOI: 10.1073/pnas.1722312115.

Caballero, R. and M. Huber (2013). "State-dependent climate sensitivity in past warm climates and its implications for future climate projections." In: *Proceedings of the National Academy of Sciences* 110.35. Publisher: Proceedings of the National Academy of Sciences, pp. 14162–14167. DOI: 10.1073/pnas.1303365110.

Carnot, S. (1824). *Réflexions sur la puissance motrice du feu et sur les machines propres à développer cette puissance*. Bachelier, Libraire, Paris.

Ceppi, P., F. Brient, M. D. Zelinka, and D. L. Hartmann (2017). "Cloud feedback mechanisms and their representation in global climate models." In: *WIREs Climate Change* 8.4, e465. DOI: 10.1002/wcc.465.

Charney, J. G., A. Arakawa, D. J. Baker, B. Bolin, R. E. Dickinson, R. M. Goody, C. E. Leith, H. M. Stommel, and C. I. Wunsch (1979). "Carbon dioxide and climate: a scientific assessment, National Research Council." In: *Washington, DC: The National Academies Press. doi* 10, p. 12181.

Chen, X. and X. Huang (2016). "Deriving clear-sky longwave spectral flux from spaceborne hyperspectral radiance measurements: a case study with AIRS observations." In: *Atmospheric Measurement Techniques* 9.12. Publisher: Copernicus GmbH, pp. 6013–6023. DOI: 10.5194/amt-9-6013-2016.

Chung, E.-S., D. Yeomans, and B. J. Soden (2010). "An assessment of climate feedback processes using satellite observations of clear-sky OLR." In: *Geophysical Research Letters* 37.2. DOI: 10.1029/2009GL041889.

Clapeyron, E. M. (1834). "Mémoire sur la puissance motrice de la chaleur la chaleur l'élasticité." In: *J. Éc. Roy. Polytech. Paris* 14, p. 23.

Clausius, R. (1850). "Ueber die bewegende Kraft der Wärme und die Gesetze, welche sich daraus für die Wärmelehre selbst ableiten lassen." In: *Annalen der Physik* 155.4, pp. 500–524. DOI: 10.1002/andp.18501550403.

Clough, S. A., F. X. Kneizys, and R. W. Davies (1989). "Line shape and the water vapor continuum." In: *Atmospheric Research* 23.3, pp. 229–241. DOI: 10.1016/0169-8095(89)90020-3.

Colman, R. and L. Hanson (2017). "On the relative strength of radiative feedbacks under climate variability and change." In: *Climate Dynamics* 49.5, pp. 2115–2129. DOI: 10.1007/s00382-016-3441-8.

Colman, R. and B. J. Soden (2021). "Water vapor and lapse rate feedbacks in the climate system." In: *Reviews of Modern Physics* 93.4. Publisher: American Physical Society, p. 045002. DOI: 10.1103/RevModPhys.93.045002.

Cormier, J. G., J. T. Hodges, and J. R. Drummond (2005). "Infrared water vapor continuum absorption at atmospheric temperatures." In: *The Journal of Chemical Physics* 122.11. Publisher: American Institute of Physics, p. 114309. DOI: 10.1063/1.1862623.

Dacie, S., L. Kluft, H. Schmidt, B. Stevens, S. A. Buehler, P. J. Nowack, S. Dietmüller, N. L. Abraham, and T. Birner (2019). "A 1D RCE Study of Factors Affecting the Tropical Tropopause Layer and Surface Climate." In: *Journal of Climate* 32.20. Publisher: American Meteorological Society Section: Journal of Climate, pp. 6769–6782. DOI: 10.1175/JCLI-D-18-0778.1.

Delamere, J. S., S. A. Clough, V. H. Payne, E. J. Mlawer, D. D. Turner, and R. R. Gamache (2010). "A far-infrared radiative closure study in the Arctic: Application to water vapor." In: *Journal of Geophysical Research: Atmospheres* 115.D17. DOI: 10.1029/2009JD012968.

Dessler, A. E. (2013). "Observations of Climate Feedbacks over 2000–10 and Comparisons to Climate Models." In: *Journal of Climate* 26.1. Publisher: American Meteorological Society Section: Journal of Climate, pp. 333–342. DOI: 10.1175/JCLI-D-11-00640.1.

Dessler, A. E. and P. M. Forster (2018). "An Estimate of Equilibrium Climate Sensitivity From Interannual Variability." In: *Journal of Geophysical Research: Atmospheres* 123.16, pp. 8634–8645. DOI: 10.1029/2018JD028481.

Dessler, A. E. (2020). "Potential Problems Measuring Climate Sensitivity from the Historical Record." In: *Journal of Climate* 33.6. Publisher: American Meteorological Society Section: Journal of Climate, pp. 2237–2248. DOI: 10.1175/JCLI-D-19-0476.1.

Dong, Y., K. C. Armour, M. D. Zelinka, C. Proistosescu, D. S. Battisti, C. Zhou, and T. Andrews (2020). "Intermodel Spread in the Pattern Effect and Its Contribution to Climate Sensitivity in CMIP5 and CMIP6 Models." In: *Journal of Climate* 33.18. Publisher: American Meteorological Society Section: Journal of Climate, pp. 7755–7775. DOI: 10.1175/JCLI-D-19-1011.1.

Dong, Y., C. Proistosescu, K. C. Armour, and D. S. Battisti (2019). "Attributing Historical and Future Evolution of Radiative Feedbacks to Regional Warming Patterns using a Green's Function Approach: The Preeminence of the Western Pacific." In: *Journal of Climate* 32.17. Publisher: American Meteorological Society Section: Journal of Climate, pp. 5471–5491. DOI: 10.1175/JCLI-D-18-0843.1.

Donohoe, A., K. C. Armour, A. G. Pendergrass, and D. S. Battisti (2014). "Shortwave and longwave radiative contributions to global warming under increasing CO2." In: *Proceedings of the National Academy of Sciences* 111.47. Publisher: Proceedings of the National Academy of Sciences, pp. 16700–16705. DOI: 10.1073/pnas.1412190111.

Eriksson, P., S. A. Buehler, C. P. Davis, C. Emde, and O. Lemke (2011). "ARTS, the atmospheric radiative transfer simulator, version 2." In: *Journal of Quantitative Spectroscopy and Radiative Transfer* 112.10, pp. 1551–1558. DOI: 10.1016/j.jqsrt.2011.03.001.

EUMETSAT (2018). *IASxxx1C0100IASI Level 1C Climate Data Record Release 1 - Metop-A*. DOI: `10.15770/EUM_SEC_CLM_0014`.

Eyring, V., S. Bony, G. A. Meehl, C. A. Senior, B. Stevens, R. J. Stouffer, and K. E. Taylor (2016). "Overview of the Coupled Model Intercomparison Project Phase 6 (CMIP6) experimental design and organization." In: *Geoscientific Model Development* 9.5. Publisher: Copernicus GmbH, pp. 1937–1958. DOI: `10.5194/gmd-9-1937-2016`.

Feldl, N. and T. Merlis (2023). "A Semi-Analytical Model for Water Vapor, Temperature, and Surface-Albedo Feedbacks in Comprehensive Climate Models." In: *Geophysical Research Letters* 50. DOI: `10.1029/2023GL105796`.

Feng, J., D. Paynter, and R. Menzel (2023a). "How a Stable Greenhouse Effect on Earth Is Maintained Under Global Warming." In: *Journal of Geophysical Research: Atmospheres* 128.9, e2022JD038124. DOI: `10.1029/2022JD038124`.

Feng, J., D. Paynter, C. Wang, and R. Menzel (2023b). "How atmospheric humidity drives the outgoing longwave radiation–surface temperature relationship and inter-model spread." In: *Environmental Research Letters* 18.10. Publisher: IOP Publishing, p. 104033. DOI: `10.1088/1748-9326/acfb98`.

Foote, E. (1856). "ART. XXXI.–Circumstances affecting the Heat of the Sun's Rays;: (Read before the American Association, August 23d, 1856.)" In: *American Journal of Science and Arts (1820-1879)* 22.66. Num Pages: 2 Place: New Haven, United States Publisher: American Periodicals Series II, p. 382.

Forster, P. M. F. and J. M. Gregory (2006). "The Climate Sensitivity and Its Components Diagnosed from Earth Radiation Budget Data." In: *Journal of Climate* 19.1. Publisher: American Meteorological Society Section: Journal of Climate, pp. 39–52. DOI: `10.1175/JCLI3611.1`.

Fournier, Q., S. Kassi, D. Mondelain, H. Fleurbaey, R. Georges, and A. Campargue (2024). "The water vapor self-continuum absorption at 8.45 µm by optical feedback cavity ring down spectroscopy." In: *Journal of Quantitative Spectroscopy and Radiative Transfer* 315, p. 108875. DOI: `10.1016/j.jqsrt.2023.108875`.

Goldblatt, C., T. D. Robinson, K. J. Zahnle, and D. Crisp (2013). "Low simulated radiation limit for runaway greenhouse climates." In: *Nature Geoscience* 6.8. Number: 8 Publisher: Nature Publishing Group, pp. 661–667. DOI: `10.1038/ngeo1892`.

Gordon, I. E., L. S. Rothman, R. J. Hargreaves, R. Hashemi, E. V. Karlovets, F. M. Skinner, E. K. Conway, C. Hill, R. V. Kochanov, Y. Tan, P. Wcisło, A. A. Finenko, K. Nelson, P. F. Bernath, M. Birk, V. Boudon, A. Campargue, K. V. Chance, A. Coustenis, B. J. Drouin, J.-M. Flaud, R. R. Gamache, J. T. Hodges, D. Jacquemart, E. J. Mlawer, A. V. Nikitin, V. I. Perevalov, M. Rotger, J. Tennyson,

G. C. Toon, H. Tran, V. G. Tyuterev, E. M. Adkins, A. Baker, A. Barbe, E. Canè, A. G. Császár, A. Dudaryonok, O. Egorov, A. J. Fleisher, H. Fleurbaey, A. Foltynowicz, T. Furtenbacher, J. J. Harrison, J.-M. Hartmann, V.-M. Horneman, X. Huang, T. Karman, J. Karns, S. Kassi, I. Kleiner, V. Kofman, F. Kwabia-Tchana, N. N. Lavrentieva, T. J. Lee, D. A. Long, A. A. Lukashevskaya, O. M. Lyulin, V. Y. Makhnev, W. Matt, S. T. Massie, M. Melosso, S. N. Mikhailenko, D. Mondelain, H. S. P. Müller, O. V. Naumenko, A. Perrin, O. L. Polyansky, E. Raddaoui, P. L. Raston, Z. D. Reed, M. Rey, C. Richard, R. Tóbiás, I. Sadiek, D. W. Schwenke, E. Starikova, K. Sung, F. Tamassia, S. A. Tashkun, J. Vander Auwera, I. A. Vasilenko, A. A. Vigasin, G. L. Villanueva, B. Vispoel, G. Wagner, A. Yachmenev, and S. N. Yurchenko (2022). "The HITRAN2020 molecular spectroscopic database." In: *Journal of Quantitative Spectroscopy and Radiative Transfer* 277, p. 107949. DOI: `10.1016/j.jqsrt.2021.107949`.

Gregory, J. M., W. J. Ingram, M. A. Palmer, G. S. Jones, P. A. Stott, R. B. Thorpe, J. A. Lowe, T. C. Johns, and K. D. Williams (2004). "A new method for diagnosing radiative forcing and climate sensitivity." In: *Geophysical Research Letters* 31.3. DOI: `10.1029/2003GL018747`.

Hansen, J., A. Lacis, D. Rind, G. Russell, P. Stone, I. Fung, R. Ruedy, and J. Lerner (1984). "Climate Sensitivity: Analysis of Feedback Mechanisms." In: *Climate Processes and Climate Sensitivity*. American Geophysical Union (AGU), pp. 130–163.

Hartmann, D. L. and K. Larson (2002). "An important constraint on tropical cloud - climate feedback." In: *Geophysical Research Letters* 29.20, pp. 12–1–12–4. DOI: `10.1029/2002GL015835`.

Held, I. M. and K. M. Shell (2012). "Using Relative Humidity as a State Variable in Climate Feedback Analysis." In: *Journal of Climate* 25.8. Publisher: American Meteorological Society Section: Journal of Climate, pp. 2578–2582. DOI: `10.1175/JCLI-D-11-00721.1`.

Held, I. M. and B. J. Soden (2000). "Water Vapor Feedback and Global Warming." In: *Annual Review of Energy and the Environment* 25.1, pp. 441–475. DOI: `10.1146/annurev.energy.25.1.441`.

Hersbach, H., B. Bell, P. Berrisford, S. Hirahara, A. Horányi, J. Muñoz-Sabater, J. Nicolas, C. Peubey, R. Radu, D. Schepers, A. Simmons, C. Soci, S. Abdalla, X. Abellan, G. Balsamo, P. Bechtold, G. Biavati, J. Bidlot, M. Bonavita, G. De Chiara, P. Dahlgren, D. Dee, M. Diamantakis, R. Dragani, J. Flemming, R. Forbes, M. Fuentes, A. Geer, L. Haimberger, S. Healy, R. J. Hogan, E. Hólm, M. Janisková, S. Keeley, P. Laloyaux, P. Lopez, C. Lupu, G. Radnoti, P. de Rosnay, I. Rozum, F. Vamborg, S. Villaume, and J.-N. Thépaut (2019a). *ERA5 monthly averaged data on single levels from 1979 to present*. Copernicus Climate Change Service (C3S) Climate Data Store (CDS). DOI: `10.24381/cds.f17050d7`.

— (2019b). *ERA5 monthly averaged data on pressure levels from 1979 to present*. Copernicus Climate Change Service (C3S) Climate Data Store (CDS). DOI: 10.24381/cds.6860a573.

— (2020). "The ERA5 global reanalysis." In: *Quarterly Journal of the Royal Meteorological Society* 146.730, pp. 1999–2049. DOI: 10.1002/qj.3803.

Hocking, J., P. Rayer, D. Rundle, R. Saunders, M. Matricardi, A. Geer, P. Brunel, and J. Vidot (2019). *RTTOV v12 Users Guide*.

Huang, X. (2020). *Aqua AIRS Level 3 Spectral Outgoing Longwave Radiation (OLR) Monthly*. DOI: DOI:10.5067/5P7KQ31XI7XJ.

Huang, X., X. Chen, B. J. Soden, and X. Liu (2014). "The spectral dimension of longwave feedback in the CMIP3 and CMIP5 experiments." In: *Geophysical Research Letters* 41.22, pp. 7830–7837. DOI: 10.1002/2014GL061938.

Huang, X., X. Chen, and Q. Yue (2019). "Band-by-Band Contributions to the Longwave Cloud Radiative Feedbacks." In: *Geophysical Research Letters* 46.12, pp. 6998–7006. DOI: 10.1029/2019GL083466.

Huang, X., W. Yang, N. G. Loeb, and V. Ramaswamy (2008). "Spectrally resolved fluxes derived from collocated AIRS and CERES measurements and their application in model evaluation: Clear sky over the tropical oceans." In: *Journal of Geophysical Research: Atmospheres* 113.D9. DOI: 10.1029/2007JD009219.

Huang, Y., S. Leroy, P. J. Gero, J. Dykema, and J. Anderson (2010). "Separation of longwave climate feedbacks from spectral observations." In: *Journal of Geophysical Research: Atmospheres* 115.D7. DOI: 10.1029/2009JD012766.

Huang, Y. and V. Ramaswamy (2008). "Observed and simulated seasonal co-variations of outgoing longwave radiation spectrum and surface temperature." In: *Geophysical Research Letters* 35.17. DOI: 10.1029/2008GL034859.

Ingersoll, A. P. (1969). "The runaway greenhouse: A history of water on Venus." In: *Journal of Atmospheric Sciences* 26.6, pp. 1191–1198.

Ingram, W. (2010). "A very simple model for the water vapour feedback on climate change." In: *Quarterly Journal of the Royal Meteorological Society* 136.646, pp. 30–40. DOI: 10.1002/qj.546.

— (2012). "Water vapor feedback in a small ensemble of GCMs: Two approaches." In: *Journal of Geophysical Research: Atmospheres* 117.D12. DOI: 10.1029/2011JD017221.

— (2013). "A new way of quantifying GCM water vapour feedback." In: *Climate Dynamics* 40.3, pp. 913–924. DOI: 10.1007/s00382-012-1294-3.

Jeevanjee, N. (2018). *The physics of climate change: simple models in climate science*. arXiv:1802.02695 [physics]. DOI: 10.48550/arXiv.1802.02695.

Jeevanjee, N. (2023). "Climate sensitivity from radiative-convective equilibrium: A chalkboard approach." In: *American Journal of Physics* 91.9, pp. 731–745. DOI: 10.1119/5.0135727.

Jeevanjee, N. and S. Fueglistaler (2020). "On the Cooling-to-Space Approximation." In: *Journal of the Atmospheric Sciences* 77.2. Publisher: American Meteorological Society Section: Journal of the Atmospheric Sciences, pp. 465–478. DOI: 10.1175/JAS-D-18-0352.1.

Jeevanjee, N., I. Held, and V. Ramaswamy (2022). "Manabe's Radiative–Convective Equilibrium." In: *Bulletin of the American Meteorological Society* 103.11. Publisher: American Meteorological Society Section: Bulletin of the American Meteorological Society, E2559–E2569. DOI: 10.1175/BAMS-D-21-0351.1.

Jeevanjee, N., D. D. B. Koll, and N. Lutsko (2021a). ""Simpson's Law" and the Spectral Cancellation of Climate Feedbacks." In: *Geophysical Research Letters* 48.14, e2021GL093699. DOI: 10.1029/2021GL093699.

Jeevanjee, N., J. T. Seeley, D. Paynter, and S. Fueglistaler (2021b). "An Analytical Model for Spatially Varying Clear-Sky CO_2 Forcing." In: *Journal of Climate* 34.23. Publisher: American Meteorological Society Section: Journal of Climate, pp. 9463–9480. DOI: 10.1175/JCLI-D-19-0756.1.

John, V. O. and B. J. Soden (2007). "Temperature and humidity biases in global climate models and their impact on climate feedbacks." In: *Geophysical Research Letters* 34.18. DOI: 10.1029/2007GL030429.

Jungclaus, J., M. Bittner, K.-H. Wieners, F. Wachsmann, M. Schupfner, S. Legutke, M. Giorgetta, C. Reick, V. Gayler, H. Haak, P. de Vrese, T. Raddatz, M. Esch, T. Mauritsen, J.-S. von Storch, J. Behrens, V. Brovkin, M. Claussen, T. Crueger, I. Fast, S. Fiedler, S. Hagemann, C. Hohenegger, T. Jahns, S. Kloster, S. Kinne, G. Lasslop, L. Kornblueh, J. Marotzke, D. Matei, K. Meraner, U. Mikolajewicz, K. Modali, W. Müller, J. Nabel, D. Notz, K. Peters-von Gehlen, R. Pincus, H. Pohlmann, J. Pongratz, S. Rast, H. Schmidt, R. Schnur, U. Schulzweida, K. Six, B. Stevens, A. Voigt, and E. Roeckner (2019). *MPI-M MPI-ESM1.2-HR model output prepared for CMIP6 CMIP historical*. DOI: 10.22033/ESGF/CMIP6.6594.

Keil, P., H. Schmidt, B. Stevens, and J. Bao (2021). "Variations of Tropical Lapse Rates in Climate Models and Their Implications for Upper-Tropospheric Warming." In: *Journal of Climate* 34.24. Publisher: American Meteorological Society Section: Journal of Climate, pp. 9747–9761. DOI: 10.1175/JCLI-D-21-0196.1.

Kiehl, J. T. and V. Ramanathan (1982). "Radiative Heating Due to Increased CO_2: The Role of H_2O Continuum Absorption in the 12–18 μm Region." In: *Journal of the Atmospheric Sciences* 39.12. Publisher: American Meteorological Society Section: Journal of

the Atmospheric Sciences, pp. 2923–2926. DOI: 10.1175/1520-04 69(1982)039<2923:RHDTIC>2.0.CO;2.

Kirchhoff, G. (1860). "Ueber das Verhältniss zwischen dem Emissionsvermögen und dem Absorptionsvermögen der Körper für Wärme und Licht." In: *Annalen der Physik* 185.2, pp. 275–301. DOI: 10.1002/andp.18601850205.

Kluft, L., S. Dacie, and S. Bourdin (2022). *atmtools/konrad: Fix ARTS and cloud interfaces.* DOI: 10.5281/zenodo.6046423.

Kluft, L., S. Dacie, M. Brath, S. A. Buehler, and B. Stevens (2021). "Temperature-Dependence of the Clear-Sky Feedback in Radiative-Convective Equilibrium." In: *Geophysical Research Letters* 48.22, e2021–GL094649. DOI: 10.1029/2021GL094649.

Kluft, L., S. Dacie, S. A. Buehler, H. Schmidt, and B. Stevens (2019). "Re-Examining the First Climate Models: Climate Sensitivity of a Modern Radiative–Convective Equilibrium Model." In: *Journal of Climate* 32.23. Publisher: American Meteorological Society Section: Journal of Climate, pp. 8111–8125. DOI: 10.1175/JCLI-D-18-0774.1.

Koll, D. D. B. and T. W. Cronin (2018). "Earth's outgoing longwave radiation linear due to H2O greenhouse effect." In: *Proceedings of the National Academy of Sciences* 115.41. Publisher: Proceedings of the National Academy of Sciences, pp. 10293–10298. DOI: 10.1073/pnas.1809868115.

Koll, D. D. B., N. Jeevanjee, and N. J. Lutsko (2023). "An Analytic Model for the Clear-Sky Longwave Feedback." In: *Journal of the Atmospheric Sciences* -1.aop. Publisher: American Meteorological Society Section: Journal of the Atmospheric Sciences. DOI: 10.1175/JAS-D-22-0178.1.

Komabayasi, M. (1967). "Discrete equilibrium temperatures of a hypothetical planet with the atmosphere and the hydrosphere of one component-two phase system under constant solar radiation." In: *Journal of the Meteorological Society of Japan. Ser. II* 45.1. Publisher: Meteorological Society of Japan, pp. 137–139.

Kythe, P. and P. Puri (2011). *Computational methods for linear integral equations.* Springer Science & Business Media.

Lang, T., A. K. Naumann, B. Stevens, and S. A. Buehler (2021). "Tropical Free-Tropospheric Humidity Differences and Their Effect on the Clear-Sky Radiation Budget in Global Storm-Resolving Models." In: *Journal of Advances in Modeling Earth Systems* 13.11, e2021–MS002514. DOI: 10.1029/2021MS002514.

Lee, H., K. Calvin, D. Dasgupta, G. Krinner, A. Mukherji, P. W. Thorne, C. Trisos, P. Aldunce, K. Barrett, G. Blanco, W. W. Cheung, S. Connors, F. Denton, A. Diongue-Niang, D. Dodman, M. Garschagen, O. Geden, B. Hayward, C. Jones, F. Jotzo, T. Krug, R. Lasco, Y.-Y. Lee, V. Masson-Delmotte, M. Meinshausen, K. Mintenbeck, A. Mokssit, F. E. Otto, M. Pathak, A. Pirani, E. Poloczanska, H.-O.

Pörtner, A. Revi, D. C. Roberts, J. Roy, A. C. Ruane, J. Skea, P. R. Shukla, R. Slade, A. Slangen, Y. Sokona, A. A. Sörensson, M. Tignor, D. Van Vuuren, Y.-M. Wei, H. Winkler, P. Zhai, and Z. Zommers (2023). *IPCC, 2023: Climate Change 2023: Synthesis Report. Contribution of Working Groups I, II and III to the Sixth Assessment Report of the Intergovernmental Panel on Climate Change [Core Writing Team, H. Lee and J. Romero (eds.)]. IPCC, Geneva, Switzerland.* Tech. rep. Edition: First. Intergovernmental Panel on Climate Change (IPCC). DOI: 10.59327/IPCC/AR6-9789291691647.

Leroy, S., J. Anderson, J. Dykema, and R. Goody (2008). "Testing Climate Models Using Thermal Infrared Spectra." In: *Journal of Climate* 21.9. Publisher: American Meteorological Society Section: Journal of Climate, pp. 1863–1875. DOI: 10.1175/2007JCLI2061.1.

Liou, K.-N. (2002). *An introduction to atmospheric radiation*. Vol. 84. Elsevier.

Liuzzi, G., G. Masiello, C. Serio, L. Palchetti, and G. Bianchini (2014). "Validation of H_2O continuum absorption models in the wave number range 180–600 cm^{-1} with atmospheric emitted spectral radiance measured at the Antarctica Dome-C site." In: *Optics Express* 22.14. Publisher: Optica Publishing Group, pp. 16784–16801. DOI: 10.1364/OE.22.016784.

Loeb, N. G., D. R. Doelling, H. Wang, W. Su, C. Nguyen, J. G. Corbett, L. Liang, C. Mitrescu, F. G. Rose, and S. Kato (2018). "Clouds and the Earth's Radiant Energy System (CERES) Energy Balanced and Filled (EBAF) Top-of-Atmosphere (TOA) Edition-4.0 Data Product." In: *Journal of Climate* 31.2. Publisher: American Meteorological Society Section: Journal of Climate, pp. 895–918. DOI: 10.1175/JCLI-D-17-0208.1.

Ma, Q. and R. H. Tipping (1991). "A far wing line shape theory and its application to the water continuum absorption in the infrared region. I." In: *The Journal of Chemical Physics* 95.9, pp. 6290–6301. DOI: 10.1063/1.461549.

Madden, R. A. and V. Ramanathan (1980). "Detecting Climate Change due to Increasing Carbon Dioxide." In: *Science* 209.4458. Publisher: American Association for the Advancement of Science, pp. 763–768. DOI: 10.1126/science.209.4458.763.

Manabe, S. and R. T. Wetherald (1967). "Thermal Equilibrium of the Atmosphere with a Given Distribution of Relative Humidity." In: *Journal of the Atmospheric Sciences* 24.3, pp. 241–259. DOI: 10.1175/1520-0469(1967)024<0241:TEOTAW>2.0.CO;2.

Mauritsen, T., R. Redler, M. Esch, B. Stevens, C. Hohenegger, D. Klocke, R. Brokopf, H. Haak, L. Linardakis, N. Röber, and R. Schnur (2022). "Early Development and Tuning of a Global Coupled Cloud Resolving Model, and its Fast Response to Increasing CO2." In: *Tellus A: Dynamic Meteorology and Oceanography* 74.2022, pp. 346–363. DOI: 10.16993/tellusa.54.

McKim, B. A., N. Jeevanjee, and G. K. Vallis (2021). "Joint Dependence of Longwave Feedback on Surface Temperature and Relative Humidity." In: *Geophysical Research Letters* 48.18. DOI: 10.1029/2021 GL094074.

Meraner, K., T. Mauritsen, and A. Voigt (2013). "Robust increase in equilibrium climate sensitivity under global warming." In: *Geophysical Research Letters* 40.22, pp. 5944–5948. DOI: 10.1002/2013 GL058118.

Merlis, T. M., K.-Y. Cheng, I. Guendelman, L. Harris, C. S. Bretherton, M. Bolot, L. Zhou, A. Kaltenbaugh, S. K. Clark, G. A. Vecchi, and S. Fueglistaler (2024). "Climate sensitivity and relative humidity changes in global storm-resolving model simulations of climate change." In: *Science Advances* 10.26. Publisher: American Association for the Advancement of Science, eadn5217. DOI: 10.1126/sc iadv.adn5217.

Mlawer, E. J., K. E. Cady-Pereira, J. Mascio, and I. E. Gordon (2023). "The inclusion of the MT_CKD water vapor continuum model in the HITRAN molecular spectroscopic database." In: *Journal of Quantitative Spectroscopy and Radiative Transfer* 306, p. 108645. DOI: 10.1016/j.jqsrt.2023.108645.

Mlawer, E. J. and D. D. Turner (2016). "Spectral Radiation Measurements and Analysis in the ARM Program." In: *Meteorological Monographs* 57.1. Publisher: American Meteorological Society Section: Meteorological Monographs, pp. 14.1–14.17. DOI: 10.1175/AMSMO NOGRAPHS-D-15-0027.1.

Mlawer, E. J., D. D. Turner, S. N. Paine, L. Palchetti, G. Bianchini, V. H. Payne, K. E. Cady-Pereira, R. L. Pernak, M. J. Alvarado, D. Gombos, J. S. Delamere, M. G. Mlynczak, and J. C. Mast (2019). "Analysis of Water Vapor Absorption in the Far-Infrared and Submillimeter Regions Using Surface Radiometric Measurements From Extremely Dry Locations." In: *Journal of Geophysical Research: Atmospheres* 124.14, pp. 8134–8160. DOI: 10.1029/2018JD029508.

Mlawer, E. J., J. Mascio, D. D. Turner, V. H. Payne, C. Flynn, and R. Pincus (2024). *A More Transparent Infrared Window*. DOI: 10.22541 /essoar.171328603.35133326/v1.

Mosso, A., T. Hocking, and T. Mauritsen (2024). "The presence of clouds lowers climate sensitivity in the MPI-ESM1.2 climate model." In: *EGUsphere*. Publisher: Copernicus GmbH, pp. 1–17. DOI: 10.5 194/egusphere-2024-618.

Mukhopadhyay, A., W. T. S. Cole, and R. J. Saykally (2015). "The water dimer I: Experimental characterization." In: *Chemical Physics Letters* 633, pp. 13–26. DOI: 10.1016/j.cplett.2015.04.016.

Murphy, D. M., S. Solomon, R. W. Portmann, K. H. Rosenlof, P. M. Forster, and T. Wong (2009). "An observationally based energy balance for the Earth since 1950." In: *Journal of Geophysical Research: Atmospheres* 114.D17. DOI: 10.1029/2009JD012105.

Muñoz-Sabater, J. (2019). *ERA5-Land monthly averaged data from 1950 to present.* Copernicus Climate Change Service (C3S) Climate Data Store (CDS). DOI: `10.24381/cds.68d2bb30`.

Muñoz-Sabater, J., E. Dutra, A. Agustí-Panareda, C. Albergel, G. Arduini, G. Balsamo, S. Boussetta, M. Choulga, S. Harrigan, H. Hersbach, B. Martens, D. G. Miralles, M. Piles, N. J. Rodríguez-Fernández, E. Zsoter, C. Buontempo, and J.-N. Thépaut (2021). "ERA5-Land: a state-of-the-art global reanalysis dataset for land applications." In: *Earth System Science Data* 13.9. Publisher: Copernicus GmbH, pp. 4349–4383. DOI: `10.5194/essd-13-4349-2021`.

Müller, W. A., J. H. Jungclaus, T. Mauritsen, J. Baehr, M. Bittner, R. Budich, F. Bunzel, M. Esch, R. Ghosh, H. Haak, T. Ilyina, T. Kleine, L. Kornblueh, H. Li, K. Modali, D. Notz, H. Pohlmann, E. Roeckner, I. Stemmler, F. Tian, and J. Marotzke (2018). "A Higher-resolution Version of the Max Planck Institute Earth System Model (MPI-ESM1.2-HR)." In: *Journal of Advances in Modeling Earth Systems* 10.7, pp. 1383–1413. DOI: `10.1029/2017MS001217`.

Nakajima, S., Y.-Y. Hayashi, and Y. Abe (1992). "A Study on the "Runaway Greenhouse Effect" with a One-Dimensional Radiative-Convective Equilibrium Model." In: *Journal of the Atmospheric Sciences* 49.23. Publisher: American Meteorological Society Section: Journal of the Atmospheric Sciences, pp. 2256–2266. DOI: `10.1175/15 20-0469(1992)049<2256:ASOTGE>2.0.CO;2`.

Newman, S. M., P. D. Green, I. V. Ptashnik, T. D. Gardiner, M. D. Coleman, R. A. McPheat, and K. M. Smith (2012). "Airborne and satellite remote sensing of the mid-infrared water vapour continuum." In: *Philosophical Transactions of the Royal Society A: Mathematical, Physical and Engineering Sciences* 370.1968. Publisher: Royal Society, pp. 2611–2636. DOI: `10.1098/rsta.2011.0223`.

Odintsova, T. A., A. O. Koroleva, A. A. Simonova, A. Campargue, and M. Y. Tretyakov (2022). "The atmospheric continuum in the "terahertz gap" region (15–700 cm−1): Review of experiments at SOLEIL synchrotron and modeling." In: *Journal of Molecular Spectroscopy* 386, p. 111603. DOI: `10.1016/j.jms.2022.111603`.

Palchetti, L., H. Brindley, R. Bantges, S. A. Buehler, C. Camy-Peyret, B. Carli, U. Cortesi, S. D. Bianco, G. D. Natale, B. M. Dinelli, D. Feldman, X. L. Huang, L. C.-Labonnote, Q. Libois, T. Maestri, M. G. Mlynczak, J. E. Murray, H. Oetjen, M. Ridolfi, M. Riese, J. Russell, R. Saunders, and C. Serio (2020). "FORUM: Unique Far-Infrared Satellite Observations to Better Understand How Earth Radiates Energy to Space." In: *Bulletin of the American Meteorological Society* 101.12. Publisher: American Meteorological Society Section: Bulletin of the American Meteorological Society, E2030–E2046. DOI: `10.1175/BAMS-D-19-0322.1`.

Pan, F. and X. Huang (2018). "The Spectral Dimension of Modeled Relative Humidity Feedbacks in the CMIP5 Experiments." In:

Journal of Climate 31.24. Publisher: American Meteorological Society Section: Journal of Climate, pp. 10021–10038. DOI: 10.1175 /JCLI-D-17-0491.1.

Paynter, D. J., I. V. Ptashnik, K. P. Shine, K. M. Smith, R. McPheat, and R. G. Williams (2009). "Laboratory measurements of the water vapor continuum in the 1200–8000 cm−1 region between 293 K and 351 K." In: *Journal of Geophysical Research: Atmospheres* 114.D21. DOI: 10.1029/2008JD011355.

Paynter, D. J. and V. Ramaswamy (2011). "An assessment of recent water vapor continuum measurements upon longwave and shortwave radiative transfer." In: *Journal of Geophysical Research: Atmospheres* 116.D20. DOI: 10.1029/2010JD015505.

— (2012). "Variations in water vapor continuum radiative transfer with atmospheric conditions." In: *Journal of Geophysical Research: Atmospheres* 117.D16, n/a–n/a. DOI: 10.1029/2012JD017504.

Pierrehumbert, R. T. (1995). "Thermostats, Radiator Fins, and the Local Runaway Greenhouse." In: *Journal of the Atmospheric Sciences* 52.10. Publisher: American Meteorological Society Section: Journal of the Atmospheric Sciences, pp. 1784–1806. DOI: 10.1175/15 20-0469(1995)052<1784:TRFATL>2.0.CO;2.

Pierrehumbert, R. T. (2010). *Principles of Planetary Climate*. Cambridge University Press.

Pierrehumbert, R. T., H. Brogniez, and R. Roca (2008). "Chapter 6 On the Relative Humidity of the Atmosphere." In: *The Global Circulation of the Atmosphere*. Ed. by T. Schneider and A. H. Sobel. Princeton University Press, pp. 143–185. DOI: 10.1515/978069123 6919-008.

Planck, M. (1901). "Ueber das gesetz der energieverteilung im normalspectrum. vol. 309, issue 3." In: *Ann. Phys*, pp. 353–363.

Previdi, M., K. L. Smith, and L. M. Polvani (2021). "Arctic amplification of climate change: a review of underlying mechanisms." In: *Environmental Research Letters* 16.9. Publisher: IOP Publishing, p. 093003. DOI: 10.1088/1748-9326/ac1c29.

Ptashnik, I. V., R. A. McPheat, K. P. Shine, K. M. Smith, and R. G. Williams (2011). "Water vapor self-continuum absorption in near-infrared windows derived from laboratory measurements." In: *Journal of Geophysical Research: Atmospheres* 116.D16. DOI: 10.1029 /2011JD015603.

Raghuraman, S. P., D. Paynter, V. Ramaswamy, R. Menzel, and X. Huang (2023). "Greenhouse Gas Forcing and Climate Feedback Signatures Identified in Hyperspectral Infrared Satellite Observations." In: *Geophysical Research Letters* 50.24, e2023GL103947. DOI: 10.1029/2023GL103947.

Roemer, F. E. and S. A. Buehler (2024a). "Observations of the Clear-Sky Spectral Longwave Feedback at Surface Temperatures Be-

tween 210 K and 310 K." In: *ESS Open Archive*. DOI: `10.22541/ess oar.171804490.08945991/v2`.

Roemer, F. E. and S. A. Buehler (2024b). *Supplementary data for "Observations of the Clear-Sky Spectral Longwave Feedback at Surface Temperatures Between 210K and 310K" [Dataset]*. DOI: `10.5281/zenodo .11394082`.

Roemer, F. E., S. A. Buehler, M. Brath, L. Kluft, and V. O. John (2023a). "Direct observation of Earth's spectral long-wave feedback parameter." In: *Nature Geoscience* 16.5, pp. 416–421. DOI: `10.1038/s4156 1-023-01175-6`.

— (2023b). *Spectrally resolved fluxes and feedbacks from observations and simulations (Version 2)*. DOI: `10.26050/WDCC/FluxFeedb_ObsSim_v 2`.

Roemer, F. E., S. A. Buehler, L. Kluft, and R. Pincus (2024a). "Effect of Uncertainty in Water Vapor Continuum Absorption on CO_2 Forcing, Longwave Feedback, and Climate Sensitivity." In: *Journal of Advances in Modeling Earth Systems* 16.7, e2023MS004157. DOI: `10 .1029/2023MS004157`.

— (2024b). *Git Patches to modify konrad to support scaling of absorption species in line-by-line calculations (Version 3) [Software]*. DOI: `10.528 1/zenodo.10961148`.

— (2024c). *Supplementary code for "Effect of Uncertainty in Water Vapor Continuum Absorption on CO2 Forcing, Longwave Feedback, and Climate Sensitivity" (Version 3) [Software]*. DOI: `10.5281/zenodo.1096 3838`.

— (2024d). *Supplementary data for "Effect of Uncertainty in Water Vapor Continuum Absorption on CO2 Forcing, Longwave Feedback, and Climate Sensitivity" (Version 3) [Dataset]*. DOI: `10.5281/zenodo.10 963797`.

Romps, D. M. (2014). "An Analytical Model for Tropical Relative Humidity." In: *Journal of Climate* 27.19. Publisher: American Meteorological Society Section: Journal of Climate, pp. 7432–7449. DOI: `10.1175/JCLI-D-14-00255.1`.

— (2020). "Climate Sensitivity and the Direct Effect of Carbon Dioxide in a Limited-Area Cloud-Resolving Model." In: *Journal of Climate* 33.9. Publisher: American Meteorological Society Section: Journal of Climate, pp. 3413–3429. DOI: `10.1175/JCLI-D-19-0 682.1`.

Saunders, R., J. Hocking, E. Turner, P. Rayer, D. Rundle, P. Brunel, J. Vidot, P. Roquet, M. Matricardi, A. Geer, N. Bormann, and C. Lupu (2018). "An update on the RTTOV fast radiative transfer model (currently at version 12)." In: *Geoscientific Model Development* 11.7. Publisher: Copernicus GmbH, pp. 2717–2737. DOI: `10 .5194/gmd-11-2717-2018`.

Schwarzschild, K. (1914). "Diffusion and absorption in the sun's atmosphere." In: *Sitzungsberichte der Königlich Preussischen Akademie der Wissenschaften Berlin*, pp. 1183–1200.

Seeley, J. T. and N. Jeevanjee (2021). "H2O Windows and CO2 Radiator Fins: A Clear-Sky Explanation for the Peak in Equilibrium Climate Sensitivity." In: *Geophysical Research Letters* 48.4, e2020–GL089609. DOI: 10.1029/2020GL089609.

Serio, C., G. Masiello, F. Esposito, P. D. Girolamo, T. D. Iorio, L. Palchetti, G. Bianchini, G. Muscari, G. Pavese, R. Rizzi, B. Carli, and V. Cuomo (2008). "Retrieval of foreign-broadened water vapor continuum coefficients from emitted spectral radiance in the H_2O rotational band from 240 to 590 cm^{-1}." In: *Optics Express* 16.20. Publisher: Optica Publishing Group, pp. 15816–15833. DOI: 10.1364/OE.16.015816.

Shepherd, T. G. (2014). "Atmospheric circulation as a source of uncertainty in climate change projections." In: *Nature Geoscience* 7.10. Publisher: Nature Publishing Group, pp. 703–708. DOI: 10.1038/ngeo2253.

Sherwood, S. C., M. J. Webb, J. D. Annan, K. C. Armour, P. M. Forster, J. C. Hargreaves, G. Hegerl, S. A. Klein, K. D. Marvel, E. J. Rohling, M. Watanabe, T. Andrews, P. Braconnot, C. S. Bretherton, G. L. Foster, Z. Hausfather, A. S. von der Heydt, R. Knutti, T. Mauritsen, J. R. Norris, C. Proistosescu, M. Rugenstein, G. A. Schmidt, K. B. Tokarska, and M. D. Zelinka (2020). "An Assessment of Earth's Climate Sensitivity Using Multiple Lines of Evidence." In: *Reviews of Geophysics* 58.4, e2019RG000678. DOI: 10.1029/2019RG000678.

Sherwood, S. C. (1996). "Maintenance of the Free-Tropospheric Tropical Water Vapor Distribution. Part II: Simulation by Large-Scale Advection." In: *Journal of Climate* 9.11. Publisher: American Meteorological Society Section: Journal of Climate, pp. 2919–2934. DOI: 10.1175/1520-0442(1996)009<2919:MOTFTT>2.0.CO;2.

Sherwood, S. C., W. Ingram, Y. Tsushima, M. Satoh, M. Roberts, P. L. Vidale, and P. A. O'Gorman (2010). "Relative humidity changes in a warmer climate." In: *Journal of Geophysical Research: Atmospheres* 115.D9. DOI: 10.1029/2009JD012585.

Shine, K. P., A. Campargue, D. Mondelain, R. A. McPheat, I. V. Ptashnik, and D. Weidmann (2016). "The water vapour continuum in near-infrared windows – Current understanding and prospects for its inclusion in spectroscopic databases." In: *Journal of Molecular Spectroscopy*. New Visions of Spectroscopic Databases, Volume II 327, pp. 193–208. DOI: 10.1016/j.jms.2016.04.011.

Shine, K. P., I. V. Ptashnik, and G. Rädel (2012). "The Water Vapour Continuum: Brief History and Recent Developments." In: *Surveys in Geophysics* 33.3, pp. 535–555. DOI: 10.1007/s10712-011-9170-y.

Siebesma, A. P., S. Bony, C. Jakob, and B. Stevens, eds. (2020). *Clouds and Climate: Climate Science's Greatest Challenge*. Cambridge: Cambridge University Press. DOI: 10.1017/9781107447738.

Simpson, G. (1928a). "Some studies in terrestrial radiation." In: *Mem. R. Meteorol. Soc* 2, pp. 69–95.

— (1928b). "Further studies in terrestrial radiation." In: *Mem. R. Meteorol. Soc* 3, pp. 1–26.

Sledd, A. and T. L'Ecuyer (2019). "How Much Do Clouds Mask the Impacts of Arctic Sea Ice and Snow Cover Variations? Different Perspectives from Observations and Reanalyses." In: *Atmosphere* 10.1. Number: 1 Publisher: Multidisciplinary Digital Publishing Institute, p. 12. DOI: 10.3390/atmos10010012.

Slingo, A. and M. J. Webb (1997). "The spectral signature of global warming." In: *Quarterly Journal of the Royal Meteorological Society* 123.538, pp. 293–307. DOI: 10.1002/qj.49712353803.

Soden, B. J., I. M. Held, R. Colman, K. M. Shell, J. T. Kiehl, and C. A. Shields (2008). "Quantifying Climate Feedbacks Using Radiative Kernels." In: *Journal of Climate* 21.14. Publisher: American Meteorological Society Section: Journal of Climate, pp. 3504–3520. DOI: 10.1175/2007JCLI2110.1.

Stefan, J. (1879). *Über die Beziehung zwischen der Wärmestrahlung und der Temperatur*. Kaiserlich-Königliche Hof und Staatsdruckerie.

Stevens, B. and L. Kluft (2023). "A Colorful look at Climate Sensitivity." In: *EGUsphere*. Publisher: Copernicus GmbH, pp. 1–24. DOI: 10.5194/egusphere-2022-1460.

Thomas, G. E. and K. Stamnes (2002). *Radiative transfer in the atmosphere and ocean*. Cambridge University Press.

Tipping, R. H. and Q. Ma (1995). "Theory of the water vapor continuum and validations." In: *Atmospheric Research* 36.1, pp. 69–94. DOI: 10.1016/0169-8095(94)00028-C.

Trenberth, K. E., Y. Zhang, J. T. Fasullo, and S. Taguchi (2015). "Climate variability and relationships between top-of-atmosphere radiation and temperatures on Earth." In: *Journal of Geophysical Research: Atmospheres* 120.9, pp. 3642–3659. DOI: 10.1002/2014JD022887.

Trigo, I. F., S. Boussetta, P. Viterbo, G. Balsamo, A. Beljaars, and I. Sandu (2015). "Comparison of model land skin temperature with remotely sensed estimates and assessment of surface-atmosphere coupling." In: *Journal of Geophysical Research: Atmospheres* 120.23, pp. 12,096–12,111. DOI: 10.1002/2015JD023812.

Tsushima, Y., A. Abe-Ouchi, and S. Manabe (2005). "Radiative damping of annual variation in global mean surface temperature: comparison between observed and simulated feedback." In: *Climate Dynamics* 24.6, pp. 591–597. DOI: 10.1007/s00382-005-0002-y.

Tsushima, Y. and S. Manabe (2013). "Assessment of radiative feedback in climate models using satellite observations of annual

flux variation." In: *Proceedings of the National Academy of Sciences* 110.19. Publisher: Proceedings of the National Academy of Sciences, pp. 7568–7573. DOI: 10.1073/pnas.1216174110.

Turner, D. D., D. C. Tobin, S. A. Clough, P. D. Brown, R. G. Ellingson, E. J. Mlawer, R. O. Knuteson, H. E. Revercomb, T. R. Shippert, W. L. Smith, and M. W. Shephard (2004). "The QME AERI LBLRTM: A Closure Experiment for Downwelling High Spectral Resolution Infrared Radiance." In: *Journal of the Atmospheric Sciences* 61.22. Publisher: American Meteorological Society Section: Journal of the Atmospheric Sciences, pp. 2657–2675. DOI: 10.1175/JAS3300.1.

Turner, E. C., H.-T. Lee, and S. F. B. Tett (2015). "Using IASI to simulate the total spectrum of outgoing long-wave radiances." In: *Atmospheric Chemistry and Physics* 15.12. Publisher: Copernicus GmbH, pp. 6561–6575. DOI: 10.5194/acp-15-6561-2015.

Tyndall, J. (1861a). "XXIII. *On the absorption and radiation of heat by gases and vapours, and on the physical connexion of radiation, absorption, and conduction.—The bakerian lecture.*" In: *The London, Edinburgh, and Dublin Philosophical Magazine and Journal of Science* 22.146, pp. 169–194. DOI: 10.1080/14786446108643138.

— (1861b). "XXXVI. *On the absorption and radiation of heat by gases and vapours, and on the physical connexion of radiation, absorption, and conduction.—The bakerian lecture.*" In: *The London, Edinburgh, and Dublin Philosophical Magazine and Journal of Science* 22.147, pp. 273–285. DOI: 10.1080/14786446108643154.

Vigasin, A. A. (2000). "Water vapor continuous absorption in various mixtures: possible role of weakly bound complexes." In: *Journal of Quantitative Spectroscopy and Radiative Transfer* 64.1, pp. 25–40. DOI: 10.1016/S0022-4073(98)00142-3.

Wing, A. A., K. A. Reed, M. Satoh, B. Stevens, S. Bony, and T. Ohno (2018). "Radiative–convective equilibrium model intercomparison project." In: *Geoscientific Model Development* 11.2. Publisher: Copernicus GmbH, pp. 793–813. DOI: 10.5194/gmd-11-793-2018.

Wright, J. S., A. Sobel, and J. Galewsky (2010). "Diagnosis of Zonal Mean Relative Humidity Changes in a Warmer Climate." In: *Journal of Climate* 23.17. Publisher: American Meteorological Society Section: Journal of Climate, pp. 4556–4569. DOI: 10.1175/2010JCLI3488.1.

Wu, W., X. Liu, Q. Yang, D. K. Zhou, and A. M. Larar (2020). "Radiometrically Consistent Climate Fingerprinting Using CrIS and AIRS Hyperspectral Observations." In: *Remote Sensing* 12.8. Number: 8 Publisher: Multidisciplinary Digital Publishing Institute, p. 1291. DOI: 10.3390/rs12081291.

Yoshimori, M., F. H. Lambert, M. J. Webb, and T. Andrews (2020). "Fixed Anvil Temperature Feedback: Positive, Zero, or Negative?" In: *Journal of Climate* 33.7. Publisher: American Meteorological So-

ciety Section: Journal of Climate, pp. 2719–2739. DOI: 10.1175/JCLI-D-19-0108.1.

Yue, Q., B. H. Kahn, E. J. Fetzer, M. Schreier, S. Wong, X. Chen, and X. Huang (2016). "Observation-Based Longwave Cloud Radiative Kernels Derived from the A-Train." In: *Journal of Climate* 29.6. Publisher: American Meteorological Society Section: Journal of Climate, pp. 2023–2040. DOI: 10.1175/JCLI-D-15-0257.1.

Zelinka, M. D., T. A. Myers, D. T. McCoy, S. Po-Chedley, P. M. Caldwell, P. Ceppi, S. A. Klein, and K. E. Taylor (2020). "Causes of Higher Climate Sensitivity in CMIP6 Models." In: *Geophysical Research Letters* 47.1. DOI: 10.1029/2019GL085782.

Zhang, M. H., J. J. Hack, J. T. Kiehl, and R. D. Cess (1994). "Diagnostic study of climate feedback processes in atmospheric general circulation models." In: *Journal of Geophysical Research: Atmospheres* 99.D3, pp. 5525–5537. DOI: 10.1029/93JD03523.

Zhou, C., M. D. Zelinka, A. E. Dessler, and S. A. Klein (2015). "The relationship between interannual and long-term cloud feedbacks." In: *Geophysical Research Letters* 42.23, pp. 10,463–10,469. DOI: 10.1002/2015GL066698.

Zhou, C., M. D. Zelinka, and S. A. Klein (2016). "Impact of decadal cloud variations on the Earth's energy budget." In: *Nature Geoscience* 9.12. Number: 12 Publisher: Nature Publishing Group, pp. 871–874. DOI: 10.1038/ngeo2828.

EIDESSTATTLICHE VERSICHERUNG
DECLARATION ON OATH

Hiermit erkläre ich an Eides statt, dass ich die vorliegende Dissertationsschrift selbst verfasst und keine anderen als die angegebenen Quellen und Hilfsmittel benutzt habe.

I hereby declare upon oath that I have written the present dissertation independently and have not used further resources and aids than those stated.

Hamburg, den 12. August 2024
Hamburg, 12 August 2024

Florian Elias Römer

Hinweis / Reference

Die gesamten Veröffentlichungen in der Publikationsreihe des MPI-M
„Berichte zur Erdsystemforschung / Reports on Earth System Science",
ISSN 1614-1199

sind über die Internetseiten des Max-Planck-Instituts für Meteorologie erhältlich:
https://mpimet.mpg.de/forschung/publikationen

All the publications in the series of the MPI -M
„Berichte zur Erdsystemforschung / Reports on Earth System Science",
ISSN 1614-1199

are available on the website of the Max Planck Institute for Meteorology:
https://mpimet.mpg.de/en/research/publications